MICRODOSIMETRY OF PHOTONEUTRONS AROUND MEDICAL LINEAR ACCELERATORS.

John S. P. Crossman

A Thesis Submitted for the Degree of PhD
at the
University of St Andrews

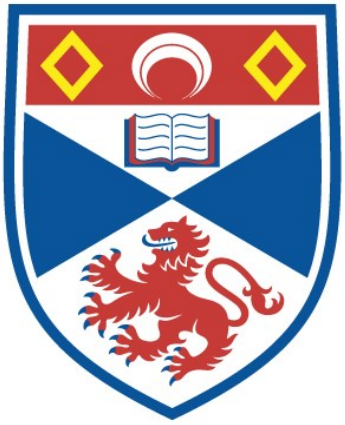

1997

MICRODOSIMETRY OF PHOTONEUTRONS AROUND MEDICAL LINEAR ACCELERATORS

by

John S.P. Crossman

(B.Sc. (Hons), P.G.C.E., M.Sc.)

A Thesis Submitted for the Degree of Doctor of Philosophy

at the University of St. Andrews

May 1996

ProQuest LLC.
789 East Eisenhower Parkway
P.O. Box 1346
Ann Arbor, MI 48106 – 1346

CONTENT OF THE THESIS

DECLARATIONS

I, J.S.P Crossman, hereby certify that this thesis, which is approximately 50,000 words in length, has been written by me, that is the record of the work carried out by me and that it has not been submitted in a previous application for a higher degree.

Date 22.7.96 Signed

J.Crossman

I was admitted as a research student in November 1991 and as a candidate for the degree of Ph.D. in November 1992; the higher study for which this is a record was carried out in the University of St.Andrews between 1991 and 1996.

Date 22.7.96 Signed

J.Crossman

CERTIFICATION

I hereby certify that the candidate has fulfilled the conditions of the Resolution and Regulations appropriate for the degree of Ph.D in the University of St. Andrews and that the candidate is qualified to submit this thesis in application for that degree.

Date Signed (supervisor)

Dr. D.E.Watt

LIST OF PUBLICATIONS

Al-Janabi, M., Crossman, J.S.P., Foster, C.J, Robertson, M. and Watt, D.E. *Yields and quality of photoneutron fields in the vicinity of high energy therapy machines.* Radiat. Prot. Dosim. **52** (1-4) 119-122 (1994).

Crossman, J.S.P. and Watt, D.E. *Inherent calibration of microdosimeters for dose distributions in lineal energy.* Radiat. Prot. Dosim. **55** (4) 295-298 (1994).

Crossman, J.S.P., Foster, C.J. and Watt, D.E. *Endo-microdosimeters for the control of radiation effectiveness in therapy application.* Radiat. Prot. Dosim. **61** (1-3) 25-28 (1995).

Crossman, J.S.P. and Watt, D.E. *Photoneutrons: An underestimated risk in radiotherapy?* Submitted for publication in Radiat. Prot. Dosim. (1995).

CONFERENCES ATTENDED

Eleventh Symposium on Microdosimetry, Gatlinburg, Tennessee, U.S.A. (September 1992).

Workshop on Advances in Radiation Measurement, Chalk River, Ontario, Canada (October 1994).

Eighth Symposium on Neutron Dosimetry, Paris, France. (November 1995).

ACKNOWLEDGEMENTS

I am very grateful to my supervisor Dr. D.E.Watt for his expert guidance and supervision. I am particularly thankful to him for his scientific advice, and general encouragement and enthusiasm.

Thanks are also due to the following: Cliff Foster and John Parry at the Department of Radiotherapy, Ninewells Hospital, Dundee for their scientific and technical advice, and considerable patience; Jim Clark and the others in the university's mechanical workshop; Les Kirk for both technical and general advice; the university's computing technical staff for their advice and swift repairs; and my colleagues in the Radiation Biophysics Group.

I gratefully acknowledge the financial support of the C.E.C. for awards as a Young Scientist to the conferences. I am also very thankful for the financial support from the Scottish Home and Health Department (SHHD) and the Association for International Cancer Research (AICR).

DEDICATION

To my wife, Elisabeth, who encouraged me constantly.

ABSTRACT

Photoneutrons produced in the vicinity of medical linear accelerators for therapy, constitute a hazard which is difficult to assess and monitor. The aims of the project were to develop new techniques, using microdosimetry, which would be suitable for the improved quality control of pulsed photon beams and for the assessment of the associated photoneutron hazard in typical treatment facilities from the perspective of the patients and staff.

The measurements of photoneutron yields and equivalent doses were obtained using activation analysis detectors around a 10 MV LINAC. To obtain adequate statistical precision, an optimum thickness of 2.5 cm of polyethylene was used that doubled the detector's sensitivity. This enabled the yields and spatial distribution of the low intensity field to be recorded. Photoneutron equivalent dose-rates of up to 0.104 $Sv.h^{-1}$, or 0.1% of the useful photon dose-rates, were measured. In the literature, however, it was found that equivalent dose-rates could reach as high as 1% of the useful photon treatment dose-rate for machines operating at X ray energies of ≥18 MV. Thus it is recommended that to uphold the principle of ALARA, such high energies (≥18 MV) should only be used when no lower energy machine is available.

Microdosimetry with a tissue equivalent proportional counter (TEPC) microdosimeter, enabled the photoneutron contribution to the quality spectrum to be identified in the maze to the treatment room of the 10 MV LINAC, and the photoneutrons there were assigned a radiation weighting factor of 20. The known problems concerning the rf interference and very high pulsed dose-rates inside the treatment room proved too severe to obtain meaningful results with the TEPC. The microdosimeter did however provide useful diagnostic information. Furthermore, a novel calibration technique for TEPC's was developed and an established one, the proton-edge method, was improved.

A new approach was adopted to conduct microdosimetry in the vicinity of medical accelerators. This involved the design of a condensed phase microdosimeter comprising, a miniature CsI(T1) scintillator coupled to an optical fibre 20 m long, for conducting in-beam, on-line measurements of quality spectra. However, Cerenkov light and scintillation light produced in the optical fibre by the radiation fields was the cause of strong interference that has yet to be overcome.

The application of the microdosimeter, which is still under development, to brachytherapy is proposed for *in-vivo* measurements.

TABLE OF CONTENTS

LIST OF TABLES

FIGURE CAPTIONS

CHAPTER 1

INTRODUCTION

1.0 General

The Ionising Radiation Regulations (Protection of persons undergoing medical treatment) 1988 require, in effect, that all exposure to ionising radiation be kept as low as possible in the examination and treatment of patients[1]. Moreover, dosimetric limits for the controlled usage of therapy machines are becoming increasingly highly specified with regard to the primary beam and to unwanted leakage and scattered radiations. Proposals have been made that the dose equivalent within the treatment room for radiotherapy be less than 0.1% of the treatment dose in the plane of the patient; and less than 0.1% for X rays and 0.5% for photoneutrons leaking through the tube housing [2].

For optimisation of treatment in radiotherapy the dosimetry must be accurate to better than 5%, some say 3.5%, and complex procedures are recommended to achieve this [3,4]. Furthermore, it is essential that the beam quality is reproducible to within the same tolerance if the correct RBE's (see section 1.2.3) are to be assumed. Therefore, the development of microdosimetric instrumentation for the improved measurement of the physical quality of therapy beams has been undertaken in the present project.

The dominant type of external beam radiotherapy machine is the high energy electron accelerator, of which the the linear accelerator (LINAC) is the most common. High energy electrons of energy E can be used directly, or they can be fired on a high-Z target to produce a continuous bremsstrahlung spectrum of X rays with a maximum energy E (in this thesis, X rays produced by electrons of energy E MeV will be denoted as E MV X rays for convenience). Radiotherapy is becoming increasingly based on machines operating above 6 MV, which is near the

photoneutron production threshold in some materials such as lead, and some machines even operate up as high as 50 MV which easily exceeds the photoneutron production threshold in all materials. Consequently, unwanted photoneutrons can be produced in the components of the machine and in the patient [5]. The neutron component of the dose has been shown to be under 1% of the primary photon beam, but it makes an important contribution to the general dose-levels within the treatment room. Thus, photoneutrons present a hazard within the treatment room without benefiting the patient as they do not significantly contribute to the treatment. Indeed, it has been calculated that 500 new fatal malignancies per year may result from photoneutron exposure during treatment in the USA alone[6].

The photoneutron dose is due to direct exposure and to exposure from radiations emitted by neutron activated materials. Personnel operating the accelerators are also at risk from the aforementioned radiations, but with a carefully designed maze, and by taking the precaution of waiting several hours before carrying out maintenance work on the treatment head where most of the activation products are formed, the hazard can be effectively minimised to below the maximum permissible levels.

The sources of stray radiation inside the treatment room that affect the patient include: the accelerator head which produces leakage photons and photoneutrons; scatter of the primary photon beam by the patient and the treatment room walls; and activation radiation and nuclear reactions within the patient and other materials in the beam path. These need to be monitored and assessed, and reduced wherever possible.

1.1.0 The physics of photoneutron production

For a comprehensive account of the physics of photoneutron production around medical accelerators the reader is referred to NCRP Report 79[7]. A brief résumé, however, is included here to explain the origins and yields of photoneutrons, as well as their spectral characteristics.

1.1.1 Photo- and electro- neutron cross-sections.

The cross-sections, or the probabilities, that neutrons are produced in the interactions with photons of 50 MeV and less, depend on the properties of the giant resonance of the photonuclear interaction. The giant resonance is principally caused by electric dipole absorption and can be considered to be a vibration of the groups of neutrons confined in a nucleus with a rigid surface. The plot of the nuclear photon absorption cross-section as a function of photon energy, E, yields a large peak which is at around 22 MeV for light nuclei and which decreases to about 13 MeV for heavy nuclei. The area under this peak, referred to as the strength of the giant resonance, can be calculated approximately using the electronic dipole sum-rule :

$$\int_0^\infty \sigma(E)dE = \frac{[2\pi^2 e^2\hbar]}{Mc^2}\ \frac{NZ}{A} = 0.06\frac{NZ}{A} \qquad \text{(MeV.barns)} \qquad (1.1)$$

where: e = 1.6 x 10^{-16} c; $\hbar = h/2\pi$ (Planck's constant/ 2π) in MeV-s; Mc^2 is the mean rest mass energy of a nucleon (Mc^2=938.926 MeV); N is the neutron number, Z is the proton number, and A = N + Z. Thus the strength of the giant resonance tends to increase with mass number, A, but it is relatively small having a maximum value of only a few millibarns per nucleon. Metals such as lead, uranium and tungsten, which are commonly found around medical accelerators, however, yield relatively

large numbers of photoneutrons due to their high masses. The width of the peak of the giant resonance varies from 4 MeV to 8 MeV (full width at half maximum).[8]

The emission of a single neutron by a photon denoted by (γ,n) is the most probable reaction to occur. However, other processes that occur include: (γ,2n), (γ,3n), (γ,pn), (γ,α), and (γ,f). The cross-sections for the preceding interactions with quasi - monoenergetic photons measured for a wide range of nuclides is given in graphical form in reference (9) and is also available in a digital format. A more comprehensive atlas of photoneutron cross-sections that includes bremsstrahlung interactions is available elsewhere[10], and for an at-a-glance table of the bremstrahlung weighted photoneutron yields for several of the more common nuclei found around medical accelerators measured by various authors see NCRP 79.

Electrons are also capable of interacting with nuclei to produce photoneutrons, but by electro disintegration in the reaction denoted by (e,e'n). The order of magnitude of the eletroneutron cross-section is of the order of the fine constant (approximately 1/137) times the corresponding bremsstrahlung weighted cross-section. Since the fluence of electrons is of the same order of magnitude as the fluence of photons, electroneutrons only make up a small portion of the total neutron fluence.

By knowing the photoneutron cross-sections, yields of photoneutrons can be calculated, for example, for the purpose of selecting a material with a low yield to use for the target such as copper[11,12].

1.1.2 Photoneutron spectrum in the treatment room

The fission source from ^{252}Cf is often used as a general good approximation of the photoneutron spectrum from typical target materials[7] (the average energy neutron energy for a variety of targets and sources is given in Table 1.1). However,

after surrounding the target with massive metal shielding, as is necessary in a high energy medical LINAC to provide photon shielding and a collimated beam of X rays, considerable distortion of the spectrum occurs. Due to the major difficulties of measuring photoneutrons in the vicinity of medical accelerators (see Chapter 4) spectral measurements are rare, although some using Bonner sphere spectroscopy away from the isocentre, that yielded low resolution results that were in poor agreement with calculated spectra do exist[13].

A theoretical approach to calculate the spectrum is adopted[14]. The production and transport of the photoneutrons can be studied using Monte Carlo calculations in various codes such as MORSE or MCNP. Several of the major assumptions are discussed here.

It is assumed that the photoneutron spectrum consists of a lower energy evaporation component and a higher energy, but smaller direct component that makes up about 12% of the total fluence[7]. The evaporation component can be described by a Maxwellian distribution given by:

$$\frac{dN}{dE_n} = \frac{E_T}{T^2} \exp\left(\frac{-E_n}{T}\right) \qquad (1.2)$$

where T is the nuclear temperature in MeV.

The photoneutron production is approximately isotropic (although there is probably some anisotropy with the direct component) and the neutrons undergo multiple collisions within the treatment head. The treatment head shielding usually made of lead, tungsten or a combination of the two is about 10-15 cm thick. It attenuates the fluence by only 15%-25% (the non-elastic scattering cross-section is small for neutrons of a few MeV and less)[7], but reduces the mean energy from 1-2 MeV by as much as a factor of 2. This spectrum emerging from the treatment head

will be referred to here on, as the direct component (in keeping with other works) and it has a mean energy $\overline{E}_{dir}$. The fluence of this direct spectrum is generally assumed to vary with the inverse square of the distance from the target.

Further distortion of the photoneutron spectrum arises because of the scattering of the photoneutrons off the walls of the treatment room. The hydrogen in the concrete walls can thermalize the neutrons rapidly and this eventually results in capture. Alternatively, the photoneutrons can scatter back out of the walls to traverse the room, and this can occur several times before capture takes place. Thus, a low-energy scattered component of the photoneutron spectrum is present throughout the room that is assumed to be constant throughout the treatment room. This scattered component of the spectrum has a mean energy denoted by $\overline{E}_{sc}$.

As Monte Carlo codes are not generally available, McCall has developed a "cookbook" method to estimate the mean energy of the total photoneutron spectrum anywhere within the room[7]. It was found that for a room with concrete walls that $\overline{E}_{sc} = 0.24\ \overline{E}_{dir}$. Then the average energy $\overline{E}$ of the total fast neutron spectrum (the thermal component must be treated separately) is given by:

$$\overline{E} = \frac{\overline{E}_{dir}\Phi_{dir} + \overline{E}_{sc}\Phi_{sc}}{\Phi_{dir} + \Phi_{sc}} = \overline{E}_{dir}\left(1 - \frac{4.1 \times 4\pi R^2}{S + 5.4 \times 4\pi R^2}\right) \qquad (1.2)$$

where Φ is the fluence, R is the distance from the target in cm, and S is the inside surface area of the room in cm^2. $\overline{E}_{dir}$ is given by $\overline{E}_t^{(HEL/x)}$ where $\overline{E}_t$ is the average energy of the spectrum from the target (given in Table 1.1), HEL is the half-energy layer of the shielding material (analogous to the half-value layer), and x is thickness of the shielding. For a typical treatment room and medical LINAC the following parameters are used to determine the average energy of the spectrum, $\overline{E}$, at 1 m from the isocentre for different bremsstrahlung in Table 1.1: S is 1.6 x 10^6 cm^2 , $R^2 = 100^2 + 100^2$ cm^2 , a tungsten shield of HEL = 7.5 cm and x = 10 cm.

Bremsstrahlung energy /source (MV)	Target material	$\overline{E}_t$ (MeV)	$\overline{E}$ (MeV)
10	W	0.65	0.37
15	W	1.8	1.43
25	W	2.2	1.86
25	Pb	2.3	1.98
Cf -252	-	-	2.15

Table 1.1

1.2.0 Radiation quality

The phenomenon that the same doses of different radiation (different types and even the same types with different energies) give rise to different degrees of biological effect is a key area of biophysics research. The aim of this research is to identify the relevant biological targets and to identify the mechanisms by which the radiation causes the effects. The cell nucleus and its strands of DNA are considered most important by far, with the key biological damage being identified as single strand and double strand breaks. However, there is still no fully satisfactory explanation of the mechanisms. The approach, so far, is to find a physical parameter, the 'radiation quality', that will closely match the biological effectiveness (currently RBE - see section 1.2.3). Some of the earlier physical parameters that have been used to describe quality as a physical parameter are summarised in Table 1.2 (the earlier parameters are merely physical descriptors that broadly differentiate between different radiation types) together with some significant developments in its evolution.

1.2.1 Linear energy transfer

The concept of linear energy transfer (LET), denoted by L_∞, the energy per unit length transferred to the medium locally by the charged particle through all the possible processes (such as ionisation, excitation, and charge exchange) has been adopted. It is exactly the same as the linear collision stopping power, S_{coll}, with the radiative energy transfers to bremsstrahlung being excluded [15].

It was found experimentally that there is always a range of LET values in cellular, or sub-cellular regions. This brought about another big advance in the specification of quality: the use of an LET distribution and its mean value. The dose average LET , L_D, for a distribution of LET events was the first and it is given by:

$$\overline{L}_D = \int_0^\infty d(L).L.dL \qquad (1.3)$$

where d(L) is the fraction of dose deposited in the LET interval L to L+dL. The dose distribution in LET is used in radiobiological experiments. Other distributions have also arisen for specific situations such as for track-segment experiments (i.e where thin biological targets that are penetrated by mono-energetic charged particles and that involve a narrow LET distribution) when the track distribution in LET is appropriate. The restricted energy versions of the dose and track distributions are also used.

However, LET and its distributions only approximately specify quality and there are many limitations to their use which include the following:

(1) It is assumed that charged particles expend their energy continuously and uniformly along tracks of negligible diameter and curvature. This assumption is consistent with the continual slowing down approximation (CSDA), but this

situation is not very realistic. The curvature of tracks for high-LET radiations is usually small, but in the case of low-LET radiations the tracks of the secondary electrons can be markedly curved. This occurs at the end of their range when the curvature is so pronounced that the radius of curvature becomes similar to the interaction mean free path.

(2) They do not take into account the fluctuations of range straggling and energy straggling that occur within sensitive biological sites with dimensions in the order of microns, or less (some say 2 nm). Fluctuations in the number of particles that penetrate a sensitive structure that is irradiated to a given dose is also unaccounted for.

(3) The type of energy transfer process may be of importance to quality, but this is not emphasised in the LET concept. Nuclear elastic collisions may have a differing damaging effectiveness compared with purely ionising collisions, for example.

Moreover, measuring LET and its distributions has proven very difficult so far. They can, however, be calculated or derived from other types of measurements.

Restricted LET is an improvement to the concept of LET by allowing for the spatial distribution of δ-rays surrounding the primary charged particle track The main drawback to the restricted LET is that the value of the energy cut-off is subjective and there is no general consensus as to what it should be. This cut-off energy is usually chosen so that the excluded δ-rays have a range greater than the sensitive structures, but the nature and dimensions of these structures is still subject to much research and controversy, however typical values used for the cut-off energy are 100-500 eV. Restricted LET with the energy cut-off has the advantage that it simplifies calculation, but a distance cut-off would be just as useful especially as it would make measurements easier.

Clearly there are many limitations associated with LET and this has meant that other parameters are being evolved with the aim of eventually finding an absolute quality parameter. Quality parameters derived from microdosimetry (see Chapter 3) are the most promising that have come into acceptance, but again there are limitations with their use. The major limitation is that the simulated site size can not be reduced below about 0.3 μm for the acquisition of single-event spectra (multi-event spectra can be obtained down to about 10 nm, but the information that they yield is much more limited).

The mean free path between ionisations is a possible parameter for defining absolute biological effectiveness. From extensive studies of biological data mainly taken from the literature, it was found that maximum biological effectiveness by direct action occurs for a mean free path (λ) of 2 nm which is the separating distance between two strands of double-stranded DNA. Also proposed are empirical damage models based on λ, and an entirely new system for radiation protection that compares different types of radiation through their ABE (Absolute Biological Effectiveness). However such a novel approach, which controversially departs from the use of energy based parameters, has yet to be widely accepted, mainly because of the considerable technical difficulties of measuring radiation interactions over the order of 10 nm.

The requirement for a practical system still must be met for the fields of radiation protection and for radiobiology.

1.2.2 Quality in radiation protection

A modifying factor, the quality factor, Q, was introduced that allows for the inter comparison of the same low doses of different radiations for radiation protection purposes. Although the values of the quality factor are based on

appropriate biological data they are also based on the judgement of the ICRP (International Commission on Radiation Protection) and are chosen to err on the side of safety. The subjective nature of Q is stressed.

Previous to 1991 the quality factor was used to give the dose equivalent, H, as follows [16]:

$$H = Q \times D \quad \text{in units of Sv (sievert)} \tag{1.4}$$

where D is the absorbed dose (Gy), Q is the quality factor (dimensionless).

Q is given as a function of LET. The current relationship between quality and LET (L_∞) given by ICRP 60 [17] in the Table 1.3 below:

L_∞ (keV.μm^{-1})	Q
< 10	1
10 -100	0.32L - 2.2
> 100	300 / (L)$^{0.5}$

Since any irradiation entails a distribution of LET values, even in the case of exposure to a monoenergetic source, the effective quality factor, $\overline{Q}$, is used. It is given by:

$$\overline{Q} = \frac{1}{D}\int D(L)Q(L)dL \tag{1.5}$$

Previously quality was given as a linear function of unrestricted LET of charged particles in water. The ICRP have suggested that the use of this function may have implied a degree of precision that was not justified because of uncertainties in the radiological data. Thus for the sake of clarity and for simplification of the protection units the ICRP have introduced the equivalent dose, H. The equivalent dose $H_{T,R}$ (in units of Sv) in tissue, T, due to radiation, R, is given by:

$$H_{TR} = w_{TR} D_{TR} \qquad (1.6)$$

where D_{TR} is the average absorbed dose. As with the quality factor, the choice of the radiation weighting factor is partially based on the judgement of a committee. Values of w_{TR} for different radiations are given in ICRP 60[17] and are summarised in the Table 1.4 below:

Radiation type	w_R
Photons all energies	1
Electrons and muons, all energies	1
Neutrons, energy < 10 keV	5
10 keV to 100 keV	10
> 100 keV to 2 MeV	20
> 2 MeV to 20 MeV	10
> 20 MeV	5
Protons	5
α-particles, fission fragments, heavy nuclei	20

If the radiation type and energy are not found in the table, then it is recommended that $\overline{Q}$ given by equation (1.5) for a 10 mm depth in the ICRU sphere[18] should be used. It is also acceptable to determine $\overline{Q}$ in terms of lineal energy [19]. This is also more convenient, as lineal energy is simpler to measure than LET.

1.2.3 Quality used in radiobiology and radiotherapy

Relative biological effectiveness, RBE, is the quality parameter for use in radiobiology and in radiotherapy. It is defined by the following equation:

$$RBE = \frac{D_B}{D_A} \qquad (1.7)$$

where D_B is the absorbed dose from radiation B and D_A is the absorbed dose from the reference radiation A. Thus RBE is the ratio of the absorbed doses of two different types of radiation that produce the same specified biological end-point. Typical end-points are death, enzyme inactivation, chromosome breakages, and mutation. The most common experiments that utilise RBE involve the irradiation of cultured cell colonies, but sometimes even live animals are used. The dose is usually set at D_0 which is the dose for 37% survival (which is equivalent to a survival fraction of 1/e) and radiation 'B' is usually the reference radiation which is typically 250 kV X rays, or ^{60}Co γ-rays, with have an RBE of unity.

In radiotherapy using X rays and electrons, high doses are used, and the variation in RBE is no more than about 20%[20] whereas the RBE' s of high LET beams can reach as high as 5. These are much lower values of quality than in radiation protection which is only applicable to low doses.

1.3 Aims of the present work

The major aims at the outset of this project were to:

(1) Develop new techniques, utilising microdosimetry, which would be suitable for the improved quality control of pulsed photon beams for the assessment of the photon and photoneutron hazards in typical treatment facilities from the perspective of both staff and patients (the technique should preferably be on-line and performed under clinical conditions).

(2) Assess the sources, yields, energy spectra and equivalent doses of photoneutrons generated within and around high energy accelerators used in radiotherapy with the objective of minimising their biological hazard.

1.4 Scope of the thesis

The regulatory background for the control of leakage, or stray, radiation around medial linear accelerators; the concept of radiation quality; and the present dosimetric system for radiation protection have been briefly examined in the introduction.

A literature review, with critical appraisal, of the dosimetric measurements, methods, and techniques for the assessment of photoneutrons is presented in Chapter 2. The problems associated with the ultra-high dose rates and electromagnetic interference from strong radio-frequency field in the vicinity of medical LINACs are highlighted. Also, equivalent doses of patient-produced photoneutrons and other photonuclear products, are collated and inter-compared.

Microdosimetry is introduced in Chapter 3. The emphasis is on the experimental techniques, with the design and commissioning of a tissue equivalent proportional counter (TEPC) achieved. Calibration techniques for TEPCs are critically reviewed and a completely new technique, the inherent electron calibration technique, which has been developed in the present work is described in depth. This has led to improvements to a conceptually similar method, the proton-edge calibration technique, for a wide range of simulated diameters being recommended.

The experimental photoneutron dosimetry and microdosimetry is the subject of Chapter 4. To obtain adequate statistical precision, a novel design of neutron activation monitor was designed, based on experimental work to determine the optimum moderator thickness. The monitor was used to determine the spatial yields of photoneutron fluences from which equivalent doses were calculated. Microdosimetry was a limited success, with spectra being obtained in the maze to the treatment room only. The results of others, however, have been collated and the

techniques used have been critically assessed. As none of the aforementioned techniques is entirely adequate to achieve the aims outlined, the decision to embark on a totally novel approach to microdosimetry was made.

Thus, a condensed phase microdosimeter is currently under development. The preliminary stages of this development and the conceptual basis are reported in Chapter 5. Included are considerations in selecting the materials; calculations of the dimensions of the detector; and estimates of the signal losses and minimum threshold of detection. Severe problems that have delayed the development of the microdosimeter, however, are identified. Future work that may overcome these problems is suggested.

Finally, in the conclusions, the risk from photoneutrons is critically reassessed. The possibility of applying the condensed phase microdosimeter to the field of brachytherapy is discussed. To argue the feasibility of microdosimetry using such a dense detector as CsI(Tl) a calculated microdose spectrum for a sphere of 1 μm in the photon field of ^{241}Am is presented.

CHAPTER 2

CONVENTIONAL DOSIMETRIC MONITORING AND ASSESSMENT OF PHOTONEUTRONS

2.0 Introduction

The main detectors, or techniques that have been used to monitor the fluence, or absorbed dose, of photoneutrons in the vicinity of LINACs used for photon therapy will be reviewed in this section. The detectors used include various activation detectors with and without moderators, thermoluminescent detectors (TLDs), etched track detectors, diodes, and more recently bubble chambers. Also included is the ^{235}U fission counter that has been used rarely, but which could be an answer to achieving reliable on-line results. Most of the detection techniques that have been used around accelerators are described in depth in NCRP 79[7] and those of a more practical nature and which are more suitable for general clinical use are described in the AAPM Report 19[21]. The main tasks involved in monitoring photoneutrons are[7] as follows: measuring the fluence and the equivalent dose, determining the neutron spectrum as a function of energy, and assessing the response of the detector to other radiation types in the mixed fields.

From an extensive literature review measurements of photoneutron fluence rates, dose rates, and equivalent dose rates have been collected and analysed.

2.1 General considerations

Typically LINACs produce pulses of radiation that last between 1-10 μs at repetition rates of between 100-400 pulses per second. Within each pulse the photons are bunched together in groups separated by about 3 ns (depending on the period of the magnetron, or klystron). Naturally the photon fluence is ultra-high in the treatment beam where it is about 1000 times greater than the neutron fluence, but outside the beam the photon to neutron ratio is reduced to between

10-100. The instantaneous photon fluence rate during each radiation pulse is enormous due to the short pulse lengths and the intense beam current (in the order of hundreds of milli-amps). It is the major problem which prevents the use of electronic active detectors (the ^{235}U fission counter is a notable exception). Examples of these are detectors include: BF_3 proportional counters, ^{3}He proportional counters, and TEPC microdosimeters. They rely on individual pulse counting and they cannot be used normally, because multiple events occur within their resolving time (typically of the order of microseconds) with the effect that serious pile-up occurs i.e. the super-position of signal pulses within the resolving time. Electromagnetic interference due to the intense radio frequency fields produced by the magnetron or klystron in the treatment room, also affects these electronically active detectors. However, with r.f. shielding using Faraday cages and triaxial cables, for example, this serious problem can be minimised.

2.2 Detectors and measuring techniques

2.2.1.0 Activation detectors

These work on the principle that certain elements when placed in a neutron field are induced with radioactivity. The $\beta-$ or γ –rays due to the induced radioactivity can then be counted if the activated material is taken to a suitable detector (for example a Geiger counter for β–rays and a NaI(Tl) spectrometer for γ–ray) and if the mass of the activation material, the irradiation time, the decay time, the half-life, and the activation cross-section are known, the neutron fluence can be calculated. Since the physics of the technique is well understood, as are the many errors and corrections associated with its use[22,23], accurate absolute fluence measurements can be performed. The experimental details of the use of activation detectors are well explained in AAPM Report 19[21]. Activation analysis was used in the present project for measurements around a LINAC at Ninewells Hospital and more details of the method adopted and calculations performed are given in section 4.1.

Activation detectors have been the most commonly used detector for photoneutron measurement around LINACs because of their following advantageous attributes: they are inexpensive (provided that the relatively sophisticated counting equipment is available) and re-usable (after the radioactivity has decayed); they can be relatively small to provide good spatial resolution; they are passive integrating devices that overcome the problem of the intense pulsed field; they are immune to any electromagnetic interference; and they can be used in harsh environments. However, the labour intense nature of the technique, particularly when several detectors are being used simultaneously, can be inconvenient and the source of error.

There are many materials that are useful as activation detectors and they are normally used in the form of a thin foil, or less frequently as a wire, or powder. Some have a high thermal neutron capture cross-section while others, known as the threshold activation detectors, are insensitive to thermal neutrons and require interactions with higher energy neutrons before they become activated. In selecting the material for the activation detector several properties require consideration. The induced activity of the detector should be maximised in order to achieve good counting statistics. Therefore the element chosen should have both a high microscopic activation cross-section and relative isotopic abundance. The half-life should be neither too long nor too short. Ideally it should be short enough that saturation (the maximum activity achievable which occurs when the rate of production equals the rate of decay) is achieved, or nearly achieved (after an irradiation time of five half-lives, for example the activity is within 5% of saturation) and it should be long enough that significant decay does not occur from the time after irradiation until the time of detection. In practice the detectors used for photoneutron detection around LINACs have half-lives of the order of minutes to several days (the longer lived products are particularly useful if the detector has to be sent to another laboratory for analysis). Also consideration is required for the nature of the emissions of

the activated product; for instance γ-rays are less affected by absorption than soft X rays or β–rays, and it is easier to perform spectroscopy with γ-rays whereby the spectra from any impurities and background can be discriminated against.

For accurate absolute flux measurements, correction factors should be applied that take into account the flux perturbation. This affect is due to the self-shielding and flux depression of the detector itself upon the neutron field. Self-shielding is an affect that causes the neutron flux at the centre of the detector to be reduced in comparison with that at the surface, while flux depression arises from the removal of neutrons in the ambient field in the vicinity of the detector. By making the detector thin (< 1mm) these corrections can be minimised. In IAEA 107[23] these corrections are considered along with other factors. These are: (1) flux depression due to cadmium shielding when used; (2) activation produced by resonance, or fast neutrons; (3) self-absorption of the β-rays (when these are the radiation being counted); (4) unwanted activities may be produced due to impurities or meta-stable states; (5) thick detectors are not isotropic.

2.2.1.1 Thermal activation detectors

Elements that are suitable for neutron activation analysis are shown in Table 2.1. Indium and gold have proven to be the most commonly used thermal neutron activation detectors for photoneutron measurements because they are readily available, their half-lives are convenient, and their cross-sections are high.

The activity for all the materials listed, is induced by the (n, γ) reaction. This has a thermal neutron cross-section that varies with 1/ v, approximately, where v is the neutron velocity. Many of the materials demonstrate significant resonances between the energy of 1 eV to 1 MeV, and the effect of the resonance neutrons on the detector's induced activity must be accounted for if the thermal neutron component of the neutron field is to be measured. This can be achieved

Element	Isotope	Relative abundance %	Thermal activation microscopic cross-section σ_c (x $10^{-24}cm^2$)	Induced activity	Half-Life	Main γ–ray energy (keV)
Vanadium	^{51}Vd	99.76	4.88 ± 5	^{52}Vd	3.76 min	1434
Manganese	^{55}Mn	100	13.3 ± 2	^{56}Mn	2.58 h	847
Cobalt	^{59}Co	100	18 ± 2	^{60m}Co	10.5 min	59
			37 ± 2	^{60}Co	5.26 y	1173
Copper	^{63}Cu	69.1	4.42 ± 0.2	^{64}Cu	12.87 h	511
	^{65}Cu	30.9	2.17 ± 0.03	^{66}Cu	5.14 min	1039
Rhodium	^{103}Rh	100	11 ± 1	^{104m}Rh	4.41 min	51
			134 ± 4	$^{104}Rh^*$	43s	556
Silver	^{107}Ag	51.35	37 ± 4	^{108}Ag	2.42 min	633
	^{109}Ag	46.85	4 ± 1	^{110m}Ag	253 d	658
Indium	^{115}In	95.71	161 ± 8	^{116m}In	54 min	417
			41 ± 5	^{116}In	14 s	434
Dysprosium	^{164}Dy	28.18	2100 ± 400	^{165m}Dy	1.25 min	198
			900 ± 300	^{165}Dy	139 min	95
Gold	^{197}Au	100	98.8 ± 0.3	^{198}Au	2.7 d	412

* Direct formation

Table 2.1

by the cadmium ratio technique through the use of two activation detectors; one bare detector and one covered by cadmium sheet of the order of 0.5 mm thick.

The cadmium acts as a low energy neutron filter because of its high capture cross-section (c. 8000 b) for neutrons with energies below about 0.4 eV, which it removes, and its low cross-section for neutrons of higher energy which it transmits. By subtracting the fluence measured by the bare detector by that measured with the cadmium covered detector, the thermal neutron fluence can be determined.

For the measurement of the fluence from the fast neutron component the activation detector is surrounded by the appropriate thickness and type of moderator (see section 4.2.1). The slow neutron component is first removed using cadmium sheeting and the fast neutron component is slowed and thermalised in the moderator.

2.2.1.2 Threshold activation detectors

Fast neutron threshold activation detector materials are listed in ICRU 26 [24]. Although the list is long, there are very few suitable materials for measurements around LINACs. The problem is that the effective threshold energy of many of these materials is higher than the mean energy of the photoneutrons, which is between about 0.3 - 2 MeV. According to Tochlin and La Riviere[25] it is unsatisfactory to use threshold detectors with a threshold above about 2 MeV. The reason is that they are sensitive to only a small portion of the photoneutron spectrum. McCall[14] has calculated the integral spectrum for various LINACs to show the moderating effect of the heavy lead shielding. For a 25 MV LINAC with 15 cm of lead shielding only about 20 % of the neutron spectrum lies above 2 MeV.

A recommended[21] material to use is phosphorous in the form of P_2O_5 as developed by Price *et al.* [26]. The $^{31}P(n,p)^{31}Si$ reaction for fast neutrons and the $^{31}P(n,\gamma)^{32}P$ reaction for thermal neutrons allow the respective components to be

measured simultaneously. An advantage of using phosphorous is that there is very little photon interference because the undesired activation products are very short-lived, or are stable. This results in a mere 4% photon response in the detector when irradiated at the isocentre of a 25 MV LINAC photon beam; moreover, there are no photoneutron reactions that yield the products viz. ^{31}Si and ^{32}P. In NCRP 79 the phosphorous activation method is reviewed and it was concluded that the method yielded accurate results. Indeed a comparison of the results of Price *et al.* of the photoneutron yields with those of others (see Table 2.4) shows good agreement. However this agreement is probably fortuitous, and it is argued in the present work that due to the insensitivity of P_2O_5 to photoneutrons, P_2O_5 is not a very suitable threshold activation material for accurate photoneutron detection.

There is a significant discrepancy in the type and magnitude of the threshold activation energy of ^{31}P used by Price *et al.* and that recommended in ICRU 29. The former authors use a threshold energy of 0.7 MeV whereas in ICRU 29 the 'effective' threshold of 2.4 MeV is quoted. The (n,p) cross-sections given in JEFPC (1994)[27] , shown in Figure 2.1, indicate that indeed 0.7 MeV is the true threshold, however the magnitude of the cross-section is approximately 7 orders of magnitude smaller than that at 2.4 MeV where the cross-section has started to flatten out. A more practical definition of the threshold neutron activation energy is obtained by weighting the cross-section by the approximate neutron fluence, if known. Since Price *et al.* only correct for the insensitivity of the detector to photoneutrons with energy below 0.7 MeV it is surprising that they achieve results which are consistent with other measurements.

In NCRP 79 the significance of the dependence of the response of the ^{31}P detector on the photoneutron spectrum is acknowledged and it is implied that although this detector would be inaccurate for measurements outside the treatment beam where the photoneutron spectrum is considerably degraded,

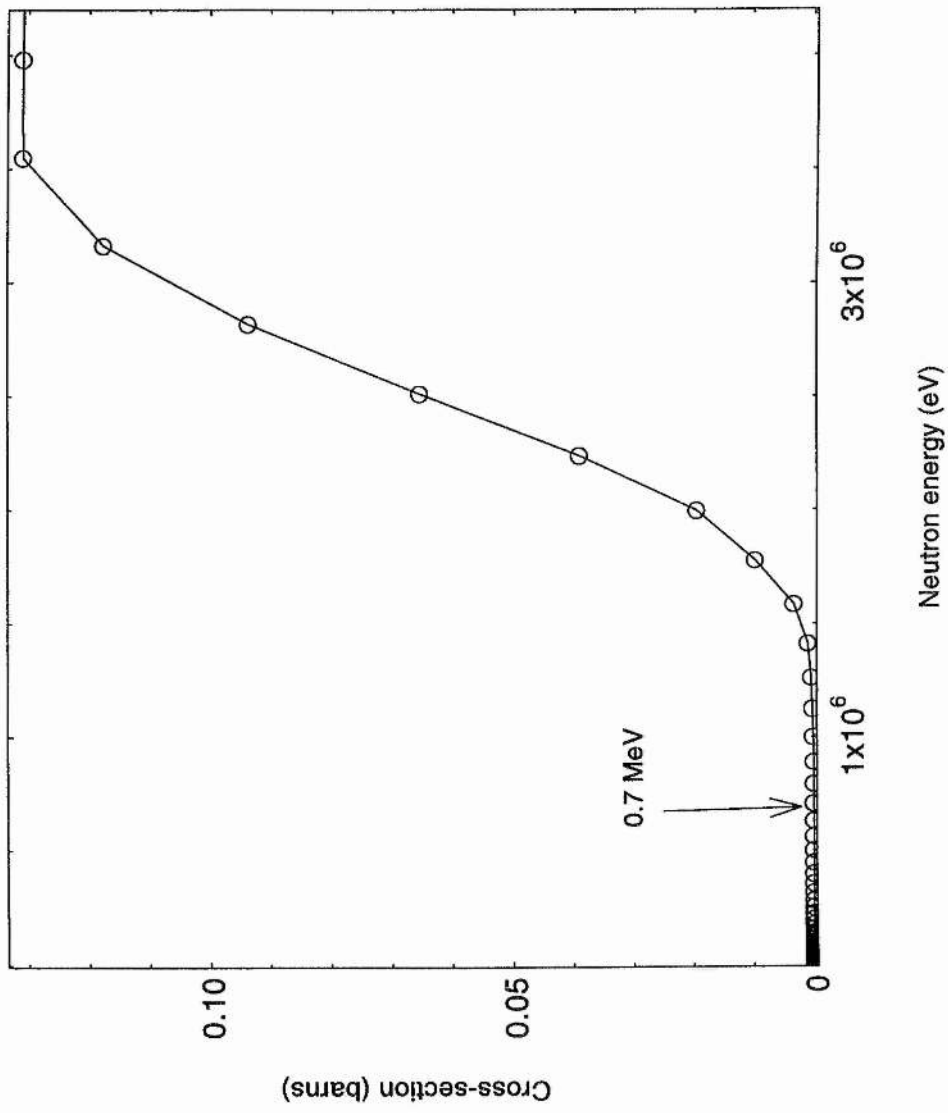

Figure 2.1. Neutron activation cross-section of ^{31}P

within the treatment beam of a high energy machine (25 MeV) the mean energy of the photoneutrons would be sufficiently high for the accurate use of the detector. This implication is examined here.

The photoneutron spectrum emerging from a thick lead target irradiated by 32 MeV electrons was measured at 90^0 to the beam using a Bonner sphere spectrometer by Holeman et al [28] . This is an unmoderated spectrum which is a good representation of the type of photoneutron spectrum considered in the NCRP report. The relative number of photoneutrons per MeV (e.g. circles) is shown in Figure 2.2 together with the relative response of a ^{31}P threshold detector (e.g. squares). The response of the detector was determined by weighting the photoneutron spectrum by the cross-section. The relative response curve shows the following: there is no response below 1.1 MeV; from 1.1 to 2.4 MeV there is a considerable under-response which would need correction; and above about 2.4 MeV (only about 45% of the spectrum lies above here) the response starts to match the spectrum well. Thus, the method even in the treatment beam would be inaccurate and would rely on corrections that in turn rely on accurate spectral information. However, this spectral information is scarce and probably inaccurate itself.

Despite this heavy reliance on spectral information, threshold detectors could be used and materials with a lower effective threshold would make more accurate detectors. However they have yet to be used for measurements of photoneutron yields around accelerators for radiotherapy. All the elements given in Table 2.2 have effective thresholds well below 2 MeV. They have been taken from ICRU 26.

2.2.2 Thermoluminescent dosimeters

Thermoluminescent dosimeters, or TLDs, work in the following manner. Incident radiation causes the formation of electron-hole pairs in the TLD material. The material used is chosen because it exhibits a high concentration of

Reaction	Half-life	Effective threshold (MeV)
$^{103}Rh(n,n')^{103m}Rh$	56.1 min	0.7
$^{115}In(n,n')^{115m}In$	12.8 d	1.4
$^{232}Th(n,f)$fission products	-	1.4
$^{237}Np(n,f)$fission products	-	0.7
$^{238}U(n,f)$fission products	-	1.4

Table 2.2. Fast neutron threshold detectors

Figure 2.2 The relative response of a phosphorus activation detector to a photoneutron spectrum

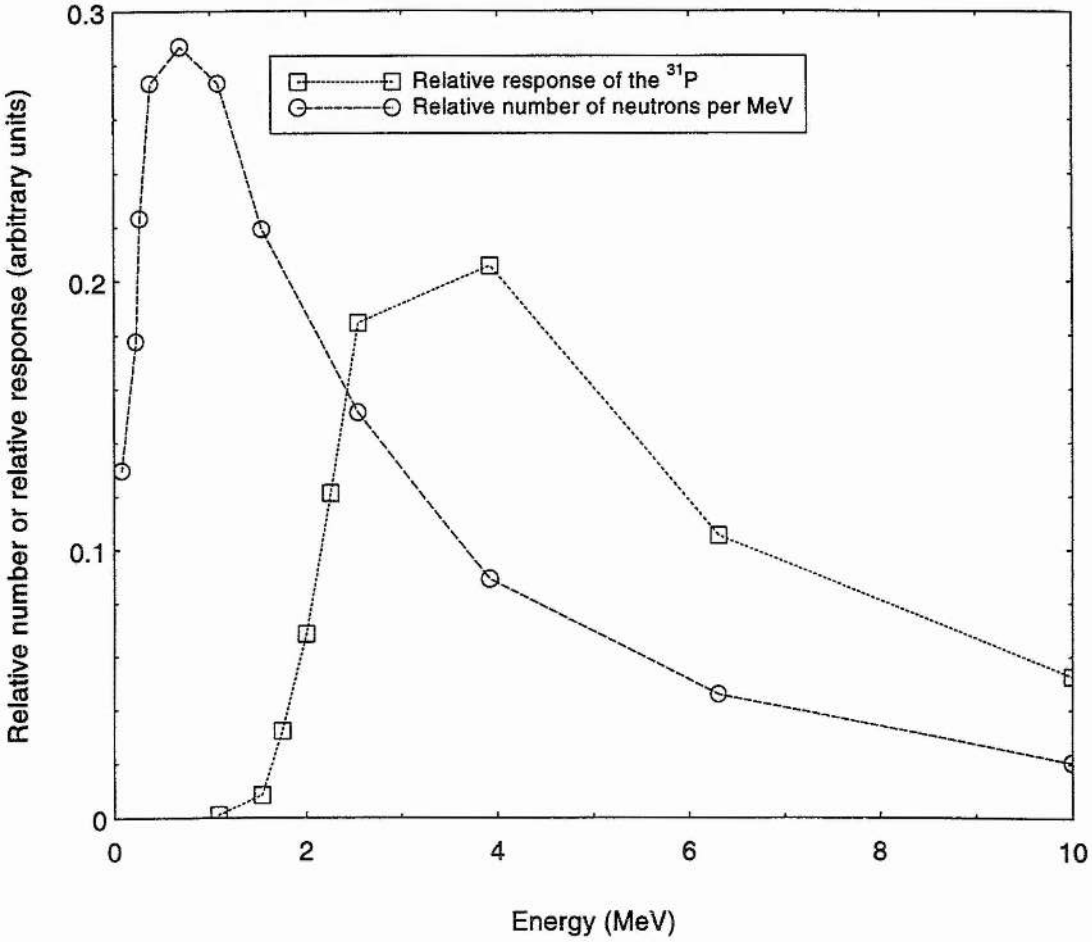

trapping centres (e.g. the site of a missing negative ion in the lattice structure will trap an electron) within the bandgap and these entrap the electron-hole pairs. The release of these trapped electrons and holes is only likely after deliberate heating of the sample. On recombination the transitions result in the emission of thermoluminescence photons which are detected using a photomultiplier tube. The light yield is recorded as a function of the sample temperature to give a "glow curve" and the area under this curve can easily be related to the absorbed dose due to the radiation field. If the TLD is surrounded by the appropriate moderator a response that is directly related to equivalent dose can be achieved.

If the sample is heated to a high enough temperature all of the trapped charges will be released, effectively erasing the radiation exposure record, and the TLD can then be re-used. Apart from being recyclable, TLDs can be read immediately by the user, they are relatively inexpensive and they are small and portable. They are also suitable for measurements in mixed neutron-gamma fields[25].

The lithium fluoride (LiF) TLD has been used for photoneutron measurements[29,30]. It contains a chip of ^{6}LiF and a chip of ^{7}LiF. ^{7}LiF which is widely used as a gamma dosimeter, is sensitive to γ-rays, but insensitive to thermal neutrons, whereas ^{6}LiF has a high thermal neutron capture cross-section (945 barns) and is therefore sensitive to thermal neutrons with which it undergoes $^{6}Li(n,\alpha)^{3}H$ reactions. Thus the difference in the readings from the two chips of LiF gives a measure of the neutron field.

A moderator is needed to thermalise fast neutrons if they are to be detected with sufficient efficiency. Thermalisation can be achieved, for example, with the use of a sphere of polyethylene surrounding the TLD (Anderson and Hwang[30] used a 25 cm thick sphere to obtain a response directly related to dose equivalent). Alternatively the thermalisation that occurs within the human body can utilised. When neutrons enter the body, some are scattered (some to the extent of being reflected) and moderated by multiple elastic

collisions with atomic nuclei. The outward flux of these low energy and thermal neutrons, i.e. albedo neutrons, can be measured by an albedo dosimeter worn close to the body in the form of a badge. To ensure that it is mainly the neutrons from the body that are being measured, cadmium (a good thermal neutron absorber) is placed on the front of the dosimeter.

A major disadvantage with the use of the albedo TLD is that the albedo neutron flux is dependent on the incident neutron energy[31]. This means that a neutron spectrum has to be assumed (if the neutron source is unknown) and calibration against an appropriate source must be made. If ^{252}Cf is chosen as the calibration source, which is often the case, then for measurements of photoneutrons there will be an overestimation of the equivalent dose by as much as several fold because photoneutron spectra are considerably degraded in comparison.

2.2.3 Track-etch detectors

Track-etch detectors take advantage of the trail of damaged molecules that are formed when densely ionising (high-LET) charged particles pass through a dielectric material. This radiation damage is in the form of microscopic tracks. Upon chemical etching, or electrochemical etching, the damaged tracks are etched away more rapidly than the surrounding material, revealing pits that can be seen under a microscope.

Before etchable damage occurs the minimum threshold for the specific energy loss (-dE/dx, or L_∞) must be exceeded by the incident radiation. This is an advantage that gives track-etch detectors excellent discrimination. against γ–rays and fast electrons.

In general the materials used are all electrical insulators, but there are also some semiconductors with wide bandgaps that can record tracks. There are two main groups of track-etch materials: organic solids (e.g. polymers) and inorganic solids (e.g. crystals and glasses). The organic solids are of interest here as they

have been used for photoneutron measurements. The most commonly used materials for fast neutron detection are: polycarbonate (Lexan^{TM} and Makrofol^{TM}), cellulose nitrate (LR -115), and CR-39 (Columbia resin 39).

The least ionising ion that can be recorded using polycarbonate foils is a 0.3 MeV α-particle [32] which means that only elastic recoils of carbon or oxygen are registered. Cellulose nitrate has a lower specific energy threshold than the polycarbonates, but this threshold LET in tissue is about L_{∞}= 100 keV.μm^{-1} which is considerably higher than the maximum L_{∞} of protons. Despite their insensitivity to protons polycarbonate and cellulose nitrate can be used together with radiators as fission-fragment track-etch dosimeters for measurements around medical accelerators. Polycarbonate plastic foils sandwiched between depleted uranium foils were used.[7]

CR-39 is a plastic polymer with a much lower specific energy threshold than cellulose nitrate and it can detect hydrogen recoils (protons) from neutrons of energy about 0.1 MeV. This is a very important attribute, especially for measurements of photoneutrons which can have a mean energy of less than 0.5 MeV around LINACs operating below 10 MV. Moreover, the equivalent dose for fast neutrons is predominantly due to protons because the energy transfer to proton recoils is greatest and the elastic (n,p) scattering cross-section is large. Therefore, the partial KERMA factor is large.

Sherwin *et al* [33] used CR-39 for measurements around LINACs. They chose to ignore the proton sensitivity of the detector. Instead they used radiator pellets of lithium borate which has a very high thermal neutron (n,α) capture cross-section and glued these to the detecting plastic. Thermalisation of fast neutrons was via the polythene moderator of an Anderson-Braun remmeter, at the centre of which the track-etch detector was placed. They compared the results with those from moderated gold activation foils and found good agreement. The mean difference between the two sets of measurements was 14% which was also the overall standard error of the track-etch measurements.

Apart from being more economical they found that the advantages of the etch-track detector over activation foils were as follows: they were easier to use; they demonstrated greater sensitivity (with a potential enhancement in sensitivity of up to ten fold); and the plastic remained as a permanent physical record of the measurement.

The main disadvantages of using CR-39 and etched-track detectors in general arise because they have a strong directional dependence due to their planar shape; the etching process takes a long time (over six hours for CR-39); and there are inconsistencies in manufacture that cause variations between different batches in sensitivity and background.

2.2.4 Superheated drop detectors and bubble detectors

D.A. Glaser (1953) invented the bubble chamber to overcome the disadvantages of the Wilson cloud chamber, the particle detector of the day. In 1965 the largest bubble detector was the 80-in chamber at Brookhaven National Laboratory which weighed in at over 450 tons (including the accompanying magnets). In contrast, with a typical weight of 10 g, the superheated drop detector (SDD) developed by Apfel [34] and the bubble detector (BD) developed by Ing *et al.* at Chalk River [35], are the bubble chamber's modern-day descendants . The principle of operation of the latter detectors does however bear similarities with that of the original.

Drops of liquid are incorporated in a fluid gel in the case of the SDD, or a firm polymer in the case of the BD. The drops of liquid are analogous to the original bubble chamber, each behaving as individual bubble chambers. The liquid is chosen so that its boiling point is below the operating temperature of the rest of the detector and thus the liquid becomes superheated. These drops are held in a semi-unstable state within the gel and can remain in this superheated state for long periods because the gel is isothermal. The passage of a charged

particle in a drop forces it to boil suddenly, expanding to form a gas bubble with a large volume increase.

In SDDs the volume of gas produced serves as an indication of the neutron dose, and this can be measured using a graduated pipette for example. Alternatively the acoustic output, or the 'pop' produced by each bubble as it is formed, can be counted using a piezoelectric transducer and counting electronics.

The use of the bubble detector can be even simpler. The bubbles formed by vaporisation of the liquid drops by the neutron induced events are small, but visible and they are fixed within the firm gel. The neutron dose is simply related to the number of bubbles seen. As with the SDDs, there is the possibility of measuring the volume of gas produced using graduated pipettes. The big advantage of the bubble detector is its re-usability. By re-pressurisation the bubbles re-condense and the detector can be used again.

Nath *et al.*[36] used SDDs (Neutrometer-HD, Apfel Enterprises) around a 25 MV LINAC. They noted that although the drop material was Freon-12 (CCL_2F_2) it is held in a gel with a similar elemental composition to tissue equivalent liquid. This is advantageous for dosimetry. The Neutrometer-HD consists of a 4 cm^2 glass vial filled with gel into which approximately $2x10^4$ liquid drops of about 65 μm in diameter (expanding to 500 μm upon vaporisation) were mixed. The volume of gel displaced due to the photoneutron field was read using a graduated pipette attached to the cap of the vial. Their results of neutron dose equivalent are generally consistent with those of others (see Table 2.3), however their results from measurements within the treatment field where the photon to neutron dose ratio is about 1000 to 1, are higher than those of others[26]. Presuming that manufacturers are correct that there are no pile-up effects in the main beam, it is argued here, that the results of Nath *et al.* demonstrate that there is a significant response to photo- and electro- nuclear reactions within the detector itself. Furthermore, contrary to the advice of the manufacturers, it is recommended that the use of SDDs, like the majority of

detectors, should be limited to measurements outside the treatment field when the accelerator is operating at and above about 18 MV. Both Figure 2.3 and Figure 2.4 provide compelling evidence of the strong influence of the photonuclear reactions within the SSD when operating within the treatment field at these higher energies.

Figure 2.3 shows the neutron dose equivalent as measured by the SSDs from electron beams with energies ranging from 7-25 MeV for a 20x20 cm^2 field size. The photoneutron yield is proportional to the (e, e'n) cross-sections which are not well known, but are expected to be 1/137 times smaller than the corresponding bremsstrahlung-weighted cross-sections[7]. For oxygen and carbon, the main constituents of the SSDs the giant resonance occurs approximately between 20-30 MeV for monoenergetic photons. Assuming this is the giant resonance region for electro-nuclear reactions, then it is hardly surprising that within the beams (up to 10 cm from the beam axis in Figure 2.3) there is a significant, but undesired, enhancement of the detector's response due to those electro-nuclear reactions. Outside the treatment field, the electron dose drops off rapidly and the electro-nuclear response which dominates the detectors response falls with a similar sharp drop-off. The strong electro-nuclear response of the detector within the treatment field explains two apparent anomalies seen in the results shown in Figure 2.3. One of these anomalies which Nath *et al.* noted is the magnitude of the neutron dose equivalent from the electron beams compared with that from the X ray beam at 25 MV. The electron beam produces a 1/5 of the photoneutron dose equivalent determined in the X ray beam. This ratio is probably a factor of at least 20 too large (deduced by extrapolation of the neutron dose equivalent measurements observed outside the treatment field). There are two reasons why it should be much smaller: the electro-neutron cross-section is small; and the electron beam is only about one milliamp when operating in electron beam mode compared with several hundred milliamps in X ray mode. The small, almost insignificant neutron dose equivalent observed

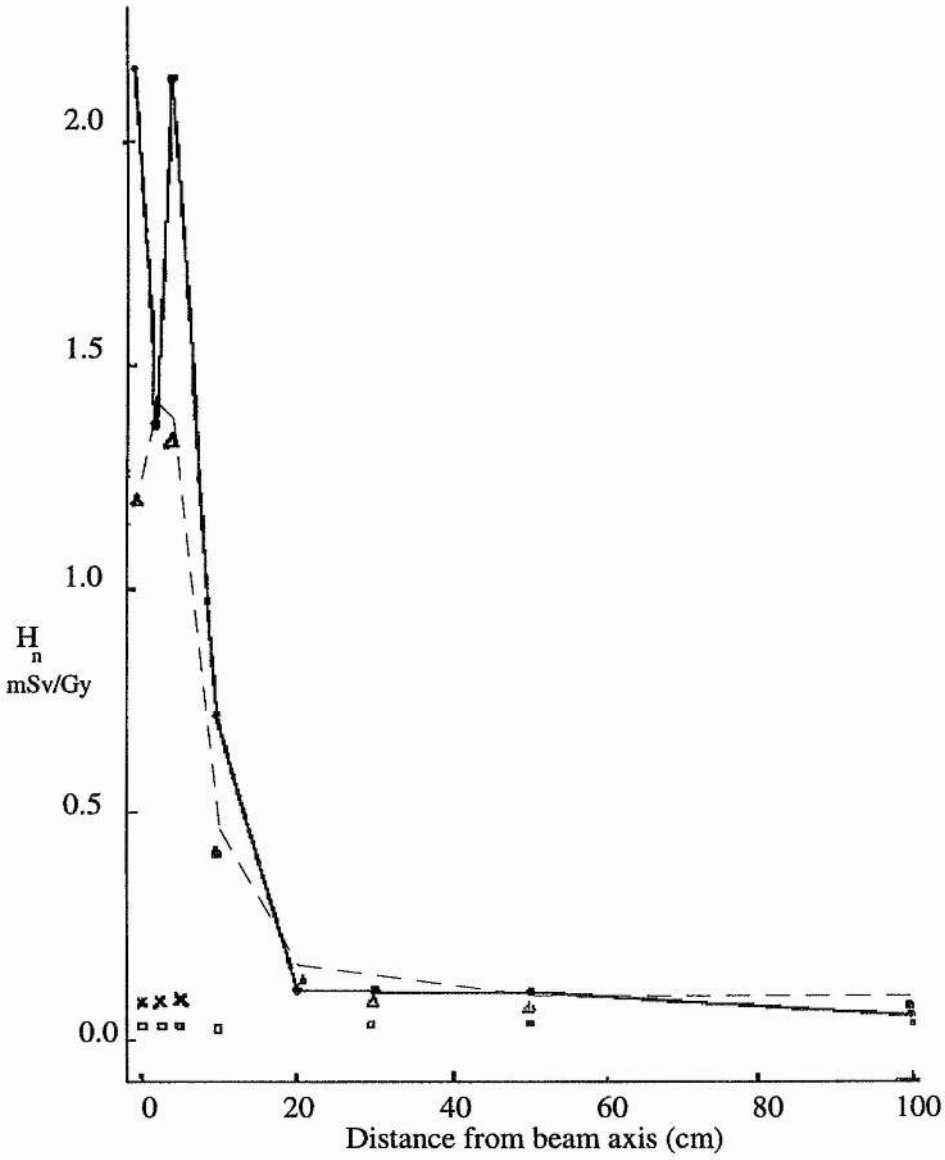

Figure 2.3 Spatial dependence of neutron equivalent dose per cGy from electron irradiation by a Sagittaire accelerator at energies of 25 MV (solid circles), 22 MV (triangles), 16 MV (crosses), and 7 MV (squares). Results for energies 10 MV, 13 MV, and 19 MV (not shown) closely followed those at 7 MV, and although they were slightly higher, they never exceeded 0.1 mSv/Gy.

at an electron beam energy of 16 MeV compared with the higher energy electron beams is also surprising. Examination of the excitation functions shows that electro-neutron production is mainly due to the interception of the electron beam by the tungsten collimators. The giant resonance for tungsten peaks for bremsstrahlung at 15 MeV and drops to approximately half of the maximum cross-section at 22 MeV. Again assuming the electro-neutron cross-sections follow the photoneutron cross-sections, then the photoneutron output from the 15 MeV beam should at least match that of the beams of higher energies. However, the response of the SDD when electro-neutron production in the collimators should be at, or close to its maximum possible level, is actually negligible.

In Figure 2.4 Nath *et al* compare their measurements in a 25 MV photon field made using the SDDs with those from Price *et al*[26](an earlier work of which Nath was a co-author). The latter group used P_2O_5 powder for activation analysis and they measured the photon response to be between 2-4%, only, of the total response of the detector. The results outside the treatment field (distances > 15 cm from the beam axis) are in good agreement with the SDD measurements and are less than or equal to those from the P_2O_5 powder and this is again due to the strong photonuclear response of the detector. The photonuclear reactions within the SDD material are mainly (γ,n), (γ,p), and (γ,α) reactions. With a large portion of the photon spectrum of the 25 MV bremsstrahlung overlapping the giant resonance region (lying between 20-30 MeV) there is significant photonuclear production in the major elemental constituents of the SDD i.e. C, O, N, F, and Cl. Within the treatment field the response of the SDD in terms of neutron dose equivalent is between 25-59% greater than that of the activation powder. The errors associated with the use of the SDD have been examined by Nath *et al.*, but the role of the photonuclear response of the detector when in the treatment beam has not been stressed. They estimate the accuracy in their measurements to be ±20%.

Figure 2.4. Photoneutron dose equivalent for two different detectors

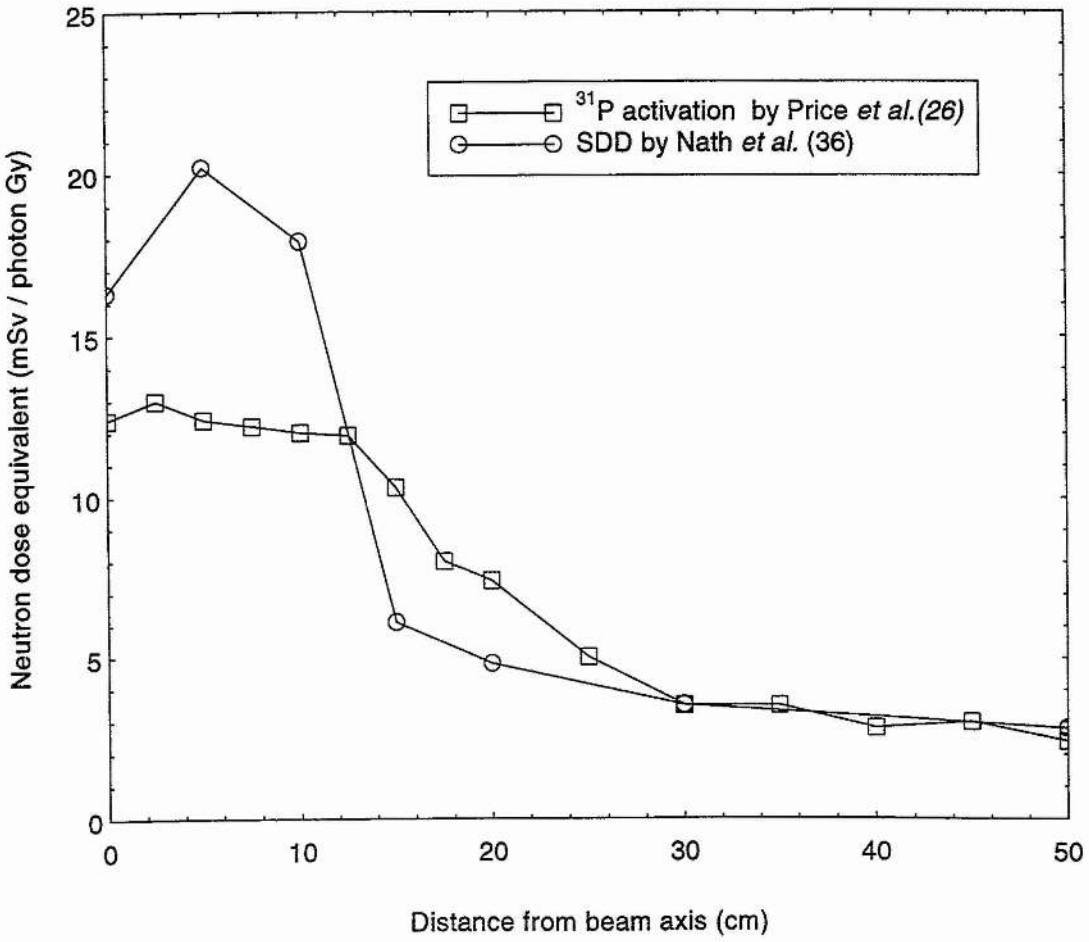

Ipe (1988) *et al.*[37] have performed an in-depth examination of the bubble detector. Irradiating the BD-100 (Chalk River Laboratories, Canada) with 6 MV bremsstrahlung from a Clinac 1800 medical accelerator they found that bubbles were produced even though there was no bubble production on irradiation with a higher dose of ^{60}Co γ-rays. They concluded that these bubbles were produced by the photodisintegration of deuterium (natural hydrogen is a constituent of the polymer), a reaction which has a threshold energy of 2.22 MeV (see Figure 2.5).

Thus both the SDD and the BD respond to high energy bremsstrahlung by way of the photonuclear reactions in the detectors themselves. This means that their use within the treatment field will result in an overestimation of the neutron dose equivalent. However, if the detectors were made to be tissue equivalent and they were placed within phantoms, they could be used to give, simultaneously, a measure of the dose due to externally produced neutrons and the dose due to photonuclear reactions within the patient.

2.2.5 The ^{235}U fission chamber

Gudowska (1988)[38] was the first to demonstrate that photoneutron yields can be obtained 'on-line' and in a LINAC treatment beam by using an electronically 'active' detector, the ^{235}U fission chamber. The key to this success rests with the excellent discrimination properties of the fission counter to unwanted radiation.

Essentially the counter is an ionisation chamber with its inner surfaces covered with 100 μg of fissile ^{235}U which has a high thermal neutron cross-section of 583 b. The energy released on the fission of ^{235}U is about 180 MeV, of which approximately 160 MeV is transferred to the kinetic energy of the fission fragments which travel in opposite directions with an energy of between 70-100 MeV each. The ionisation chamber is used in pulse counting mode and on an amplitude basis alone, it is a simple matter to discriminate the high energy fragments from the background of α–particles and fast electrons (produced by

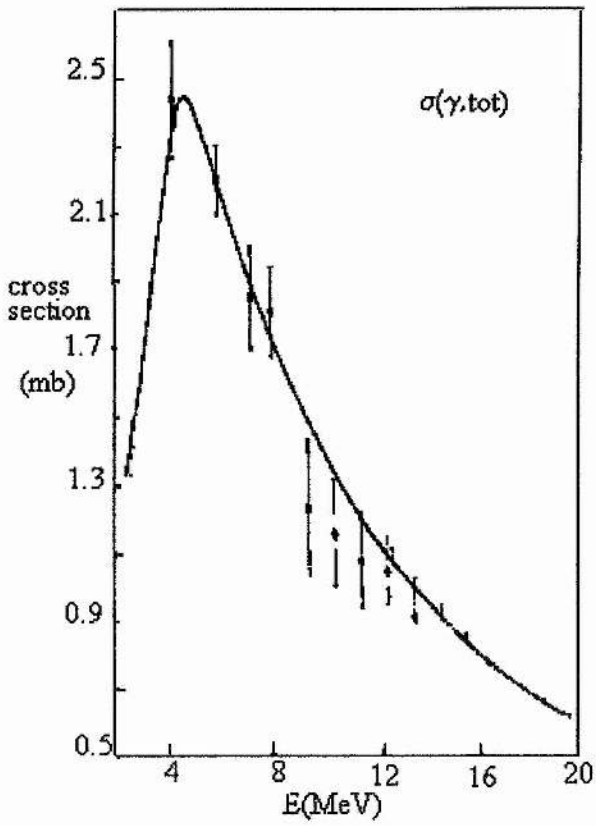

Figure 2.5. The photoneutron cross-section of deuterium

the interactions of the photon beam) that will deposit a maximum energy per event of about 5 MeV and several keV respectively. Additionally, by optimising the dimensions of the counter the fission-fragment signal to the α–particle signal ratio can be increased because of the following: the fission-fragment track is approximately half the length of an α–particle track; and the energy deposition over a fission-fragment track is greatest at the start whereas the alpha-particle deposits most of its energy at the end of its track.

Moderation of the fast neutron fluence was through the use of a polyethylene cylinder of the Anderson-Braun type of 7.5 cm wall thickness. Furthermore for measurements within the treatment beam itself a lead filter measuring 3 x 3 x12 cm^2 was mounted on the cylinder to screen the counter. The filter was required for measurements within the treatment beam because the pulsed photon beams from high energy medical accelerators are so intense that the signal pulses that they produce in the detector are greater than the signal pulses from fission fragments due to the photoneutrons. Even with the filter in place the signal due to the photon beam was a factor of 10 greater than the neutron induced signal. The detector was used without the lead filter outside the beam because the photon dose rate falls off sharply there, and the ratio of the photon signal to the neutron signal was about 50 to 1. It was estimated that whenever the photon signal was greater than the neutron signal, a 10% correction on the total number of fission counts was needed to account for missing fission counts that were lost electronically. The thermal neutron fluence was determined by measurements using the fission counter without the moderator.

Gudowska does not clearly explain how the fast neutron component was separated from the thermal component and how the fast neutron cross-section, which is not insignificant in comparison with the thermal neutron cross-section[27], was taken into account. Therefore, it is recommended that the cadmium ratio method be used if the accurate determination of the thermal and fast neutron components is required. This would, however, have the slight

disadvantage of expense, as a substantial amount of cadmium sheeting would be required.

Fast neutron calibration was achieved using a known ^{252}Cf source and separate thermal neutron calibration was taken via measurements from a reactor pile.

Gudowska performed extensive measurements using the fission counter around six different high energy therapy accelerators including LINACs, betatrons, and microtrons. These measurements are in good agreement with those found in the literature shown in Table 2.3 and NCRP 79.

Verification of the accuracy of the fission counter for photoneutron measurements was achieved through a comparison with measurements using indium activation foil. The agreement between the two methods for the many measurements was within 15%. The total error associated with the measurements using the fission counter was 20%[38], with the principle source of error being the inaccuracy of the fluence-to-dose conversion factors. This is due to a lack of similarity between the spectrum of ^{252}Cf and the various photoneutron spectra. Other sources of error associated with the fission counter measurements that were corrected for were estimated to be as follows[38]: photoneutron production in the polythene moderator up to 20 MV was negligible, for 21 MV it was 3%, and for 42-50 MV it was 35%; photoneutron production in the lead filter was 4%; and the thermal neutron diffusion in the moderator was 6%.

The major advantage with this detector is the possibility of using it on-line while the accelerator is in clinical use. Also it is portable and can easily be transferred for measurements around other accelerators.

2.2.6 Diodes

These semi-conductor devices can be used passively for photoneutron measurements. Damage, which is greatest for high-LET radiation, occurs as

charged particles pass through the diode and cause a change in the electrical characteristics. This damage is usually caused by the displacement of lattice atoms which in turn upsets the equilibrium of excess charge carriers in the junction. This causes a change in the forward voltage of the diode when a small current is passed through the device. The change in voltage before and after irradiation can serve as a measure of the neutron fluence, for example, if calibrated against a suitable source.

The main disadvantage of using diodes is that they have a high sensitivity to high photon fluxes and this prohibits their use in-beam. Also because of fading effects, it is recommended that measurement of the forward voltage should be delayed after irradiation by 48 hours. However, silicon diodes are re-usable. By annealing at 300°C for 2 minutes about 80% of the damage will be removed[39].

2.3.0 Photoneutron Measurements

Experimentally measured yields of photoneutrons using the instruments and techniques described previously are given in this section together with some calculated yields. The measurements are of the following: the fast neutron and thermal photoneutrons produced within the accelerator itself; the patient-produced photoneutrons; and additionally, the photonuclear charged particles produced in the patient.

2.3.1.0 Photoneutrons produced in the accelerator

Photoneutrons are produced mainly in the high-Z materials in the accelerator's treatment head when operating above about 6 MV.

2.3.1.1 Fast neutron measurements

Despite the difficulties of measuring photoneutron fields, a considerable amount of experimental data exists and many of the results published prior to 1984 are tabulated in NCRP 79[7]. Much of this data has been combined with more recent results that also utilise a wide variety of dosimetric techniques These have been collected and compiled and are shown in Table 2.3 where the total neutron equivalent dose for each measurement for a typical course of treatment of 40 Gy of X rays (e.g. 20 fractions of 2 Gy) has been calculated and is shown in column 7. Although there is a scarcity of measurements of the photoneutron spectrum, it is known that the mean neutron energy lies between 0.1 MeV to 2 MeV (see section 1.1.2) where the weighting factor of $w_R = 20$ [17] is used for calculating the equivalent dose. For measurements where the absorbed dose was given, multiplication by 20 was performed to give equivalent dose. For the measurements where dose equivalent was given, these values were simply doubled to give equivalent dose, assuming a quality factor of Q =10 had been used originally. For values of dose equivalent where a quality factor was stated in the original paper (in three cases a factor of about 7 had been used) a multiplication factor equal to the ratio of 20/Q was used to transform to the equivalent dose. All of the measurements were taken with the LINACs operating under normal treatment conditions with a source-to-skin distance of 1 m. The measurements taken from NCRP 79 (i.e. pre-1984) are for different sized treatment fields, and the more recent values have been restricted to values for 10x10 cm^2 fields (in an attempt to bring more consistency). Additionally all of the measurements were performed outside the treatment field to avoid any significant effects due to photonuclear reactions within the detectors themselves.

The total neutron equivalent dose for a typical course of treatment against the nominal photon energy (e.g. 25 MV is the bremsstrahlung of 25 MeV electrons impinging on a target with a maximum photon energy of 25 MeV, but a mean energy closer to 12 MeV) is shown as a histogram in Figure 2.6.

Table 2.3. Photoneutron production around LINACs

		Neutron leakage per photon treatment Gy at the isocentre						
Photon Energy MV	Distance from isocentre cm	Dose equivalent Sv	Absorbed dose Gy	Fluence cm^{-2}	Equival-ent dose Sv	Total H for a 40 Gy treatment mSv	Method	Reference
8	60	3.8e-5	-	-	-	3	-	46
10	10	-	6.0e-5	1.5e6	-	48	A	47
10	100	1.0e-4	1.0e-5	3.2e5	-	8	D	48
10	30	-	-	3.8e5	7.8e-3	10	A	49
10	100	4.0e-5	-	-	-	3	B	50
10	100	-	-	1.6e6	5.8e-4	24	A	51
15	50	2.5e-4	-	1.9e6	5.7e-4	23	A	52
15	100	4.0e-4	-	-	8.0e-4	32	A	53
16	20	2.5e-4	-	-	-	20	-	54
18	100	8.7e-4	-	-	-	70	A	55
18	10	-	1.4e-4	4.1e6	2.8e-3	112	D	56
18	100	-	1.5e-4	-	3.0e-3	120	C	57
18	100	2.1e-3	-	-	-	168	B	50
18	100	1.3e-3	-	2.0e-7	-	104	A	40
18	50	3.7e-3	-	1.7e-7	7.4e-3	296	H	Gudowska 1988
18	50	2.5e-3	-	1.4e7	5.3e-3	212	A	McCall 1982
18	50	2.0e-3	-	1.2e7	4.3e-3	172	A	McCall 1982
18	50	8.0e-4	-	-	-	64	D	Bading 1982
20	100	1.7e-3	-	-	-	136	F	Anderson 1980
20.4	50	2.6e-3	-	-	-	208	B	Rogers 1980
21	100	1.7e-3	-	-	-	136	A	53
21	100	1.2e-3	-	-	-	96	A	53
24	50	9.9e-4	-	-	-	88	A	McCall 1982

Table 2.3 (contd.) Photoneutron production around LINACs

		Neutron leakage per photon treatment Gy at the isocentre						
Photon Energy MV	Distance from isocentre cm	Dose equivalent Sv	Absorbed dose Gy	Fluence cm^{-2}	Equival-ent dose Sv	Total H for a 40 Gy treatment mSv	Method	Reference
25	30	3.5e-3	-	1.9e7	-	400	C	Wilenzick 1979 from Nath 1979
25	100	3.3e-3	3.3e-3	-	1.2e-3	264	C	Marbach 1975
25	50	2.1e-3	2.5e-4	-	2.0e-4	200	E	Holeman 1977
24	50	6.3e-4	-	5.0e6	1.5e-3	60	A	LaRiviere 1982
25	50	3.8e-3	-	-	-	304	-	Nath 1979
25	100	2.0e-3	-	-	-	160	F	Anderson 1983
25	100	4.1e-3	-	-	-	328	B	Rogers 1981
25	100	3.1e-3	-	-	-	248	B	Rogers 1981
20-25	50	-	-	-	5.4e-3	216	G	Sherwin 1988
20-25	50	-	-	-	4.8e-3	192	I	Sherwin 1988
20-25	50	-	-	-	2.0e-3	80	I	Sherwin 1988
20-25	100	-	-	-	3.6e-3	144	I	Sherwin 1988
20-25	100	-	-	-	4.0e-3	160	I	Sherwin 1988
20-25	100	-	-	-	1.6e-3	64	I	Sherwin 1988
25	15	-	-	-	5.9e-3	237	G	Nath 1993
25	15	-	-	-	1.0e-2	400	A	Price 1978
25	100	1.3e-3	-	-	-	104	A	Tosi 1990
30	100	2.3e-3	-	-	-	184	F	Anderson 1983
35	100	2.4e-3	-	-	-	192	F	Anderson 1983

Key: A - moderated activation foils; B - activation foils in remmeter moderator; C - silicon diodes; D - bare activation foils; E - Bonner spectrometer; F - moderated TLDs; G - super heated drop detectors.; H - fission fragment ionsation chamber; I - moderated etch-track detectors.

Figure 2.6. A comparison of the total equivalent dose from LINACs operating at different energies

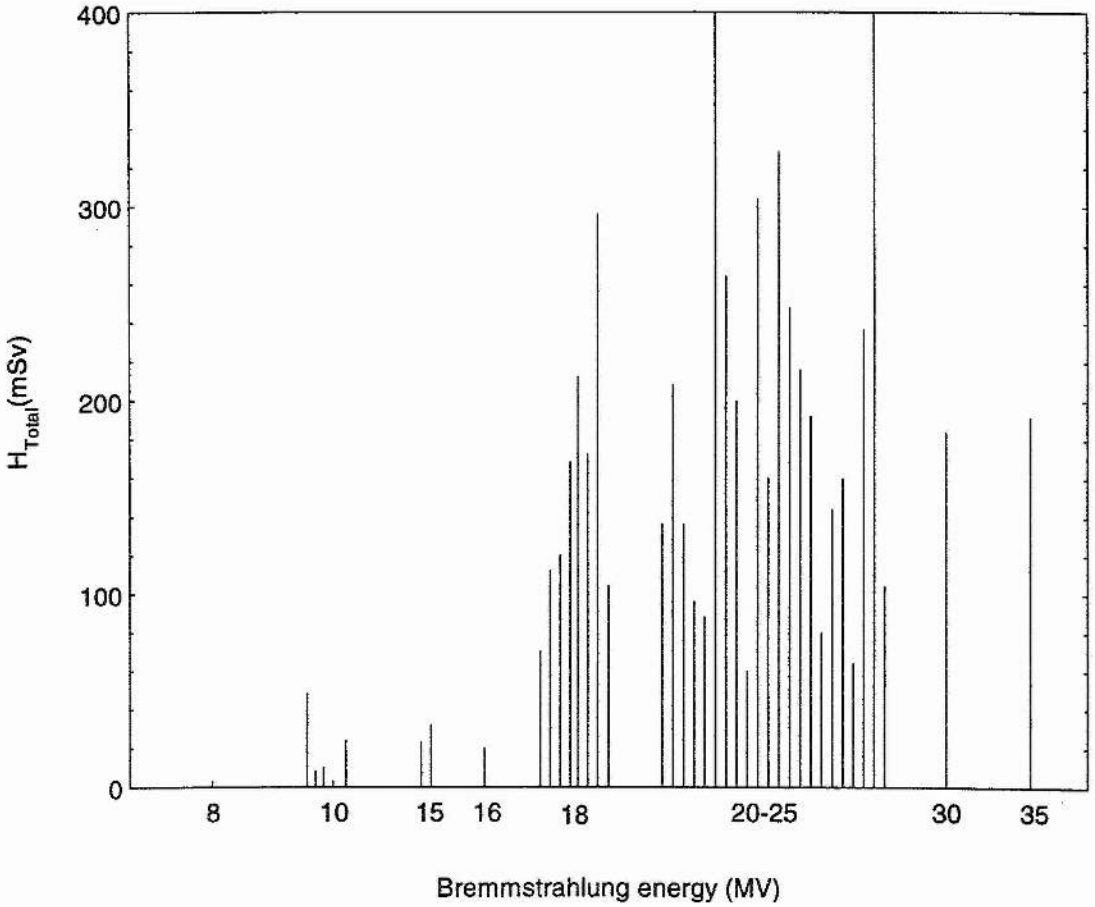

2.3.1.2 Thermal neutrons

There are very few measurements of thermal photoneutrons. Holeman *et al.* [28] used a Bonner spectrometer in the vicinity of a 25 MV Sagitaire LINAC and measured a slow component (< 0.1 keV) outside the treatment beam of 2.1×10^{-5} Gy/ treatment Gy. This was about an order of magnitude smaller than the fast neutron component. The slow neutron component was fairly constant at to up to 2 m from the target, but it fell by 80% at the inside of the treatment room door.

Using the above result and applying a radiation weighting factor of 5, the equivalent dose to the patient for a 40 Gy X ray treatment would be 4 mSv. The fast neutron equivalent dose for the same treatment would be 160 mSv. It is interesting, that despite its small contribution to the equivalent dose, the fluence of slow neutrons is approximately the same order of magnitude as the fast neutron component.

Sanchez *et al.*[40] measured the thermal neutron component around an 18 MV LINAC. This component was roughly homogeneous throughout the treatment room with the fluence rates only varying from 8.4×10^5 to 1.0×10^6 cm^{-2} / treatment Gy. Converting to dose equivalent, this thermal neutron component was two orders of magnitude smaller than the epithermal component.

A similar result, that the thermal neutron dose equivalent was 2% of the fast neutron dose equivalent was found by Anderson and Hwang[30] using moderated TLDs. They found the thermal neutron distribution to be isotropic.

Gudowska[38] also found that for six different electron accelerators the distribution of thermal neutrons was fairly homogeneous, but these measurements performed with a fission counter were for distances up to a maximum of 1 m only from the isocentre. For one accelerator operating at 18 MV the fluence varied between 2.1×10^6 to $2.9 \times 10^6 cm^{-2}$/ treatment Gy.

2.3.2.1 Photoneutrons produced in the patient

When energies above about 15 MV are used, significant photoneutron production starts to occur in the common low-Z materials (C, N, and O) within the patient's body. There are no known direct measurements of photoneutrons produced within the patient in clinical conditions (e.g. measurements using phantoms), but there are rough calculations and Monte Carlo calculations[5,41,42,44]. These are shown in Figure 2.7 against the bremsstrahlung energy.

Allen and Chaudhri[5] have made the most thorough and recent investigations of photoneutron production in tissue. They measured the photoneutron yields from a tissue-equivalent liquid from high energy bremsstrahlung (6 to 30 MeV) using a 4π Halpern-type neutron detection system that consisted of 16 BF_3 proportional counters embedded in a polythene block. The photon beam came from a microtron with a very small neutron component which was accounted for. It was shown that even at 6 MV there is some photoneutron production, but the yield is approximately three orders of magnitude lower than at 28 MV. At 16 MV the photoneutron yield is two orders of magnitude less than at 25 MV. Allen and Chaudhri compared measured yields with calculated yields and found that the photoneutron cross-sections for the rarer isotopes in tissue (^2H, ^{13}C, ^{15}N, ^{17}O, ^{18}O) needed to be considered to obtain good agreement.

Ing *et al.*[41] and Laughlin *et al.*[42] have ignored these rare constituents of tissue in their calculations and their results, although consistent with each other and in fair agreement with the activation measurements of Fox and M^{c}Allister[43] are lower than Allen and Chaudhri. The latter authors explained that their results are higher because of the use of different bremsstrahlung spectra, and to a lesser extent the use of different excited states of the residual nuclei were assumed. The results of a rough calculations by Horsley *et al.*[44] are in good agreement with the results of Allen and Chaudhri. The latter authors estimated

Figure 2.7 Patient produced photoneutron doses at different bremsstrahlung energies

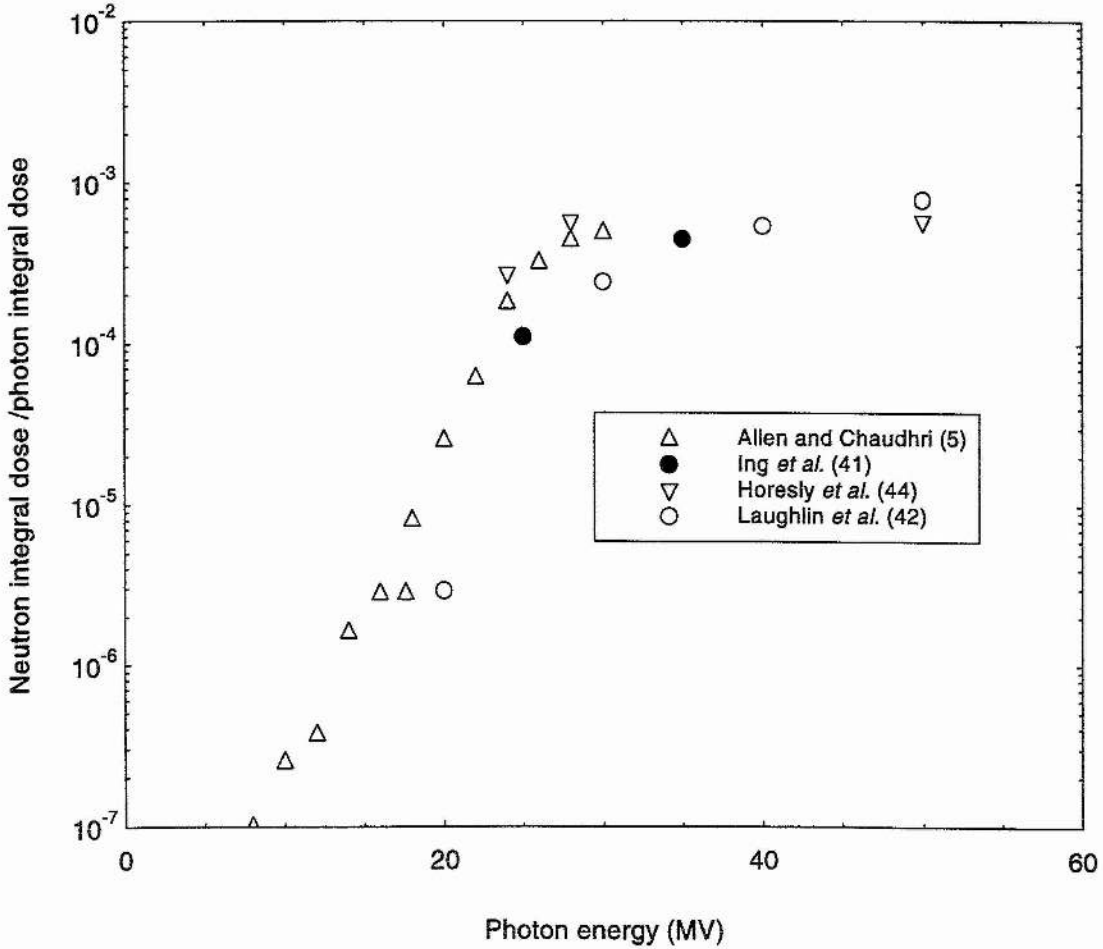

that an integral equivalent dose of 0.3% and 1.0% of the integral equivalent dose for 24 MV and 30 MV bremsstrahlung respectively. Ing *et al.*[41] estimated that the tissue produced photoneutron integral absorbed dose is 0.012% and 0.043% of the integral dose of 25 MV X rays and 35 MV X rays respectively. These doses correspond to equivalent doses of 0.24% and 0.86% of the photon treatment dose.

2.3.2.2 Photonuclear reactions in the patient

Allen and Chaudhri[45] have estimated that for 24 MV bremsstrahlung, 24% of the integral absorbed dose is due to neutrons, while 69% is due to protons, and 7% is due to α-particles. This is an equivalent dose that is 1.1% of the photon dose. Their estimate for a 30 MV bremsstrahlung beam is an equivalent dose of 2.9% of the photon dose.

2.4 Conclusions

All of the methods described in this chapter can provide dosimetric measurements that quantify the photoneutron fields that are reasonably accurate for the purpose of radiation protection to the patient. It is very difficult to decide, from comparing results in the literature, which method is the most accurate, mainly due to a lack of measurements under the same conditions. There are many variables which include: model of LINAC because of the effects of using different targets, beam flatteners, beam-bending systems and collimators; age and condition of LINAC; beam size; beam energy; size of room; and source-to-skin distance. The importance of performing local measurements around individual LINACs rather than relying on the results of others is stressed because there are so many variables. Sherwin *et al.*[33] found that even between two LINACs of the same model, but at different stages in their lives (i.e. one was being commissioned at the factory while the other was in use at a hospital) the photoneutron yields differed. The most important factors that

cause the differences in photoneutron production between different models are the composition and thickness of the target (typically Au, Pl, or W) and the collimators (typically Pb or W). The size of the treatment field will also effect the photoneutron output. The major factors that effect the measurements themselves include the following: the plane of measurement, the distance from the isocentre, and the size and the shape of the room, which will affect the photoneutron spectral distribution.

Some of the variables have been kept constant and a comparison of the results from different measurement methods for a 25 MV X ray beam from a variety of models of LINAC for a 10 x 10 cm field at a source-to-skin distance (ssd) of approximately 1 m is shown in Table 2.4.

Table 2.4:

	Neutron equivalent dose (mSv/ treatment Gy)			Reference
Method	Isocentre	0.5 m to the side	1 m to the side	
P_2O_5	15.2	7.8	4.0	Price. (26)
Multisphere	-	5.2	4.2	Nath (13)
Moderator-Au foil and Monte Carlo	11.3	4.8	-	M^{c}Call (61)
Track-etch	-	7.0	-	Wilenzick (1979) in (13)
Silicon diode	-	-	6.6	Marbach (59)
Moderator -TLDs	-	-	4.1	Anderson (30)
Moderator - Au foil	-	5.2	2.6	Tosi (53)
Bubble detector	14.0	2.8	3.6	Nath (36)

Clear evidence can be obtained from Figure 2.4 that the photoneutron production from high-Z materials in LINACs operating in X ray mode at about 18 MV and above, greatly exceeds that of the LINACs operating at lower energy (8-16 MV). This result is hardly surprising because at the higher energies mentioned, there is a considerable number of photons with energies at the peak of the giant resonance, whereas at the lower energies the majority of photons in the bremsstrahlung spectra have comparatively tiny photoneutron cross-sections[8]. To reduce the photoneutron hazard significantly and to follow the principle of A.L.A.R.A (as low as reasonably achievable), the use of high energy photons

(≥18 MV) should be avoided whenever treatments permit. Choosing the lower energies would also reduce photoneutron production in the patient by a similar amount.

The use of a phantom for *in-vivo* style measurements is recommended because the patient-produced photoneutrons can be measured at the same time as the accelerator-produced photoneutrons. In general there are a lack of photoneutron measurements, particularly so at the lower X ray energies (6-10 MV nominal photon energy). More measurements are therefore needed to establish photoneutron yields at these lower energies near the photoneutron production threshold.

The major limitation with most of the techniques reviewed here, is that the spectral information required is scarce, and this means errors can occur when selecting the fluence-to-dose conversion, where applicable, and the calibration sources. This is not the case in microdosimetry where the quality of the photoneutron field can be measured simultaneously with the absorbed dose.

CHAPTER 3

MICRODOSIMETRY

3.0 General

As a science, microdosimetry, deals with the spatial and temporal energy deposition distributions by ionising radiations in cellular and sub-cellular structures, and their relationship to biological effects. The overall objective is to closely link the physical processes of radiation interactions in human cells to the biological effects. In a single measurement, both the absorbed dose (the quantity of radiation) and the microdosimetric quality of the radiation can be obtained, thus making microdosimetry a very useful tool particularly in radiobiological research, radiation protection and radiotherapy.

Microdosimetry is concerned with the stochastic nature of ionising radiation as manifest by the random microscopic fluctuations of the energy deposition in cellular biological targets. In conventional dosimetry, quantities such as dose and LET (linear energy transfer) are used; these are mean values associated with the energy deposition. For small volumes, highly LET radiation, and small doses, significant departure from these mean values occur, with the fluctuations ranging in magnitude between zero and many times the mean value. It is for these measurements that microdosimetry is the technique of choice.

In 1955, Rossi[64,65] the principal founder of microdosimetry developed a counter for the measurement of the LET of heavy ions. Instead it was the ionisation produced in the gas by charged particles that was measured. From this measurement and by knowing the mean energy required to produce an ion pair, the energy imparted was determined (that is after calibration - see section 3.6). From this work the spherical tissue equivalent proportional counter (TEPC), or Rossi counter emerged. Rossi and co-workers then went on to develop the conceptual framework

and instrumentation that has established lineal energy, as a stochastic alternative to LET.

The design and construction of microdosimeters is well established, but there are still difficulties in their accurate calibration. In the following chapter, a résumé is given of the principles of microdosimetry; the design and commissioning of a cylindrical microdosimeter for applications in (γ,n) mixed fields is described; and a critical study of the methods of calibration that includes the development of a new calibration method is reported.

3.1 Microdosimetric quantities and their distributions

The microdosimetric quantities and distributions that are used in this thesis together with some of the other microdosimetric quantities in common usage are defined here. These are taken from ICRU 36 [66]. For a more concise list of the quantities and for a useful summary of their applications see Blanc and Terrisol [67].

These are all stochastic quantities unless otherwise stated.

Energy deposit

The energy deposit, ε_i , in a single interaction is:

$$\varepsilon_i = T_{in} - T_{out} + Q_{\Delta m} \qquad (3.1)$$

where: T_{in} = energy of the incident ionising particle (exclusive of rest mass)

T_{out} = the sum of the energies of all ionising particles leaving the interaction

$Q_{\Delta m}$= the changes of the rest mass energy of the atom and all the particles involved.

The unit of ε_i is the joule (J), but it is usually expressed in electron-volt (eV).

Energy imparted

The energy imparted, ε , to the matter in a volume is:

$$\varepsilon = \sum_i \varepsilon_i \qquad (3.2)$$

where the summation is performed over all energy deposits, ε_i , in that volume.

Lineal energy

The lineal energy, y, is the quotient of ε by $\bar{l}$ where ε is the energy imparted to the matter in the volume by a single event deposition. It is analogous to the non-stochastic quantity LET, and is given by:

$$y = \frac{\varepsilon}{\bar{l}} \qquad (3.3)$$

The unit is $J.m^{-1}$, but $keV.\mu m^{-1}$ is more convenient in practice.

The mean chord length in a volume is the mean length of randomly oriented chords in that volume. For a convex body , $\bar{l} = 4V/A$ where V is the volume of the body and A is the surface area.

It should be noted that in the special case of a sphere or a circular cylinder (one with its length equal to its height) the mean chord length is given by: $\bar{l} = \frac{2}{3}d$, where d is the diameter of the sphere. In the case of a cylinder the mean chord length is given by: $\bar{l} = \frac{2rh}{r+h}$, where r is the radius and h is the height.

Specific energy

The specific energy (imparted), z, is the quotient of ε by m, where energy ε is imparted to mass, m. It is analogous to the non-stochastic quantity, dose. The specific energy is given by:

$$z = \frac{\varepsilon}{m} \qquad (3.4)$$

The unit is $J.kg^{-1}$,but the special unit, the gray (Gy) is used.

The distributions

The distribution function of y has a value F(y), which is the probability that the lineal energy is equal to or less than y. The probability density f(y) is the derivative of F(y) with respect to y:

$$f(y)=\frac{dF(y)}{dy} \tag{3.5}$$

It is known as the lineal energy distribution and it can be thought of as the fraction of events (normalised) over a small lineal energy interval dy. This distribution is valid for single energy deposition events only, it is independent of the absorbed dose or dose rate, and it has an expectation value called the frequency mean lineal energy which is given by:

$$\bar{y}_F = \int_0^\infty yf(y)dy \tag{3.6}$$

This is a non-stochastic quantity.

Another useful distribution is the dose distribution of y. Let D(y) be the fraction of absorbed dose delivered with lineal energy less than or equal to y. The dose probability density, d(y), of y is the derivative of D(y) with respect to y:

$$d(y)=\frac{dD(y)}{dy} \tag{3.7}$$

The dose distribution is also independent of absorbed dose or absorbed dose rate. It has an expectation value:

$$\bar{y}_D = \int_0^\infty yd(y)dy \tag{3.8}$$

It is known as the dose-mean lineal energy and is of course, non-stochastic. It is related to frequency-mean lineal energy by:

$$\bar{y}_D = \frac{1}{\bar{y}_f} \int_0^\infty y^2 f(y) dy \qquad (3.9)$$

The dose distribution is related to the lineal energy distribution by:

$$d(y) = \frac{y}{\bar{y}_f} f(y) \qquad (3.10)$$

There are also analogous distributions and mean values in specific energy, z, where y, in the equations above can simply be substituted by z.

3.2.0 The Tissue Equivalent Proportional Counter

The TEPC (tissue equivalent proportional counter) operated at low gas pressures is the typical instrumentation for microdosimetry. One was therefore specially designed, built and commissioned at the University of St.Andrews for the purpose of measuring photoneutrons in the vicinity of a LINAC (see Figure 3.1). Its major features are typical of other TEPCs which rely on the phenomenon of gas multiplication to amplify the charge created within the fill-gas. The majority of counters are spherical Rossi-type TEPCs, but the one built for the present work is cylindrical, mainly because of the better field distribution. In following sections some of the fundamental concepts behind TEPC operation are briefly discussed mainly to demonstrate the rationale behind the design of the counter used in this work. Fully detailed accounts of TEPC design, construction and use can be found in ICRU 36 [66] and in a EURODOS report[68].

3.2.1 Gas multiplication

The polarity of the TEPC is arranged such that the electrons are attracted towards the centre wire, the anode. The field strength at a distance, r, from the anode is given by:

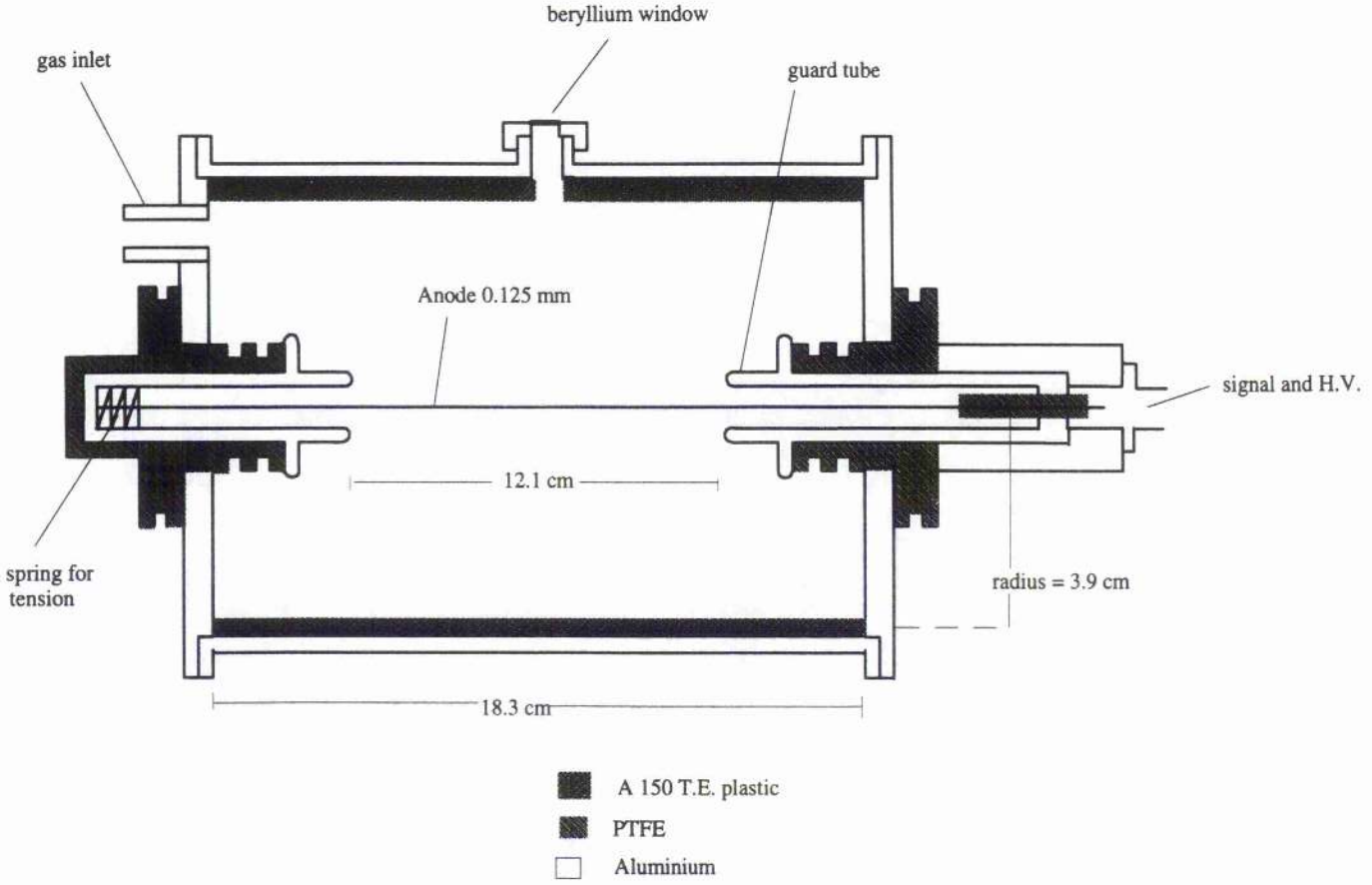

Figure3.1 The TEPC showing the materials used and some of the dimensions.

$$E(r) = \frac{V}{r \ln(b/a)} \tag{3.11}$$

where V = applied voltage; a = anode wire radius; b = cathode inner radius

When ionisation occurs within the volume of a proportional counter, the electron-ion pairs formed are immediately torn further apart by the electric field. Each electron is accelerated towards the anode and eventually gains sufficient kinetic energy that when it is involved in a collision with a gas atom, further ionisation occurs. The radial field ensures that these secondary ionising collisions only happen in the small volume of gas, known as the multiplication region, that immediately surrounds the anode and where the electric field is at its greatest. The original electron together with any new electron that is liberated by ionisation, will be accelerated towards the anode. These electrons in their next collisions release more electrons, and so the process continues. The number of electrons moving towards the central wire will therefore increase exponentially and this multiplication of electrons is known as the avalanche effect. Almost all of the primary ion pairs are formed outside the multiplication region into which they are accelerated, and so, in general, each electron undergoes the same degree of multiplication, regardless of its position of formation.

Despite the fact that many mathematical expressions for the multiplication factor have been derived none of the formulae can be applied satisfactorily to a wide range of gas pressures and types, and cathode and anode radii. However, several empirical formulae exist that are suitable for specific situations. The multiplication factor has been measured by Campion and Kingham[69] in a methane based T.E gas for cylindrical geometry. The following equation was derived:

$$\ln M = \frac{AV}{B \ln(b/a)} \left\{ \exp \frac{-aBp \ln(b/a)}{V} - \exp \frac{-bBp \ln(b/a)}{V} \right\} \tag{3.12}$$

where: M is the gas multiplication factor; V is the applied voltage; a is the anode radius; b is the cathode radius; p is the gas pressure; A and B are constants over a range of restricted field strengths (300 - 28000 $V.cm^{-1}.torr^{-1}$) which is the field measured at the surface of the anode. The importance of a stable voltage supply can be appreciated by examining equation (3.12). It can be seen that multiplication varies rapidly with a changing voltage.

3.2.2 Design of the counter

The following two factors were considered carefully when selecting the cathode radius, the anode wire radius, or gauge, and the operating voltage: (1) Ideally, the multiplication factor should be sufficient to raise the signal created by a single ion pairs above the electronic noise level; (2) The electric field must be great enough to reach saturation i.e. the complete collection of charge regardless of where the charge within the counter is formed. Approximate calculations for the multiplication factor and electric field were as follows:

(1) The total noise from the preamplifier, high voltage supply, and the amplifier was 1.5 mV for amplifier gain of unity. The combined capacitance of the pre-amp. and short coaxial lead was estimated to be 20 pF. The voltage pulse from one ion pair, without multiplication is then 8×10^{-9} V. The multiplication required to raise the voltage pulse due to one ion-pair above the electronic noise level is $>1.88 \times 10^5$. From Table 3.1 below, the required operating voltage is around 1200 V.

However, in practice the electronic noise from TEPC counting systems is such that it is difficult to measure energy deposition events of less than 100 eV[66] or about 4 ion pairs. The voltage required to raise the signal from 4 ion pairs above the electronic noise level is around 1100 V. To minimise the occurrence of spurious

pulses and sparks (which can damage the counter) 1100 V was taken as the upper limit of operation.

Table 3.1

The multiplication factor, M, from equation 3.12 as a function of voltage for the proportional counter with anode radius, a = 0.0125 cm, and cathode radius, b = 3.9 cm, filled with T.E. gas at a pressure, p = 7.1 torr to simulate a mean chord length of 1 μm (see section 3.3 later).

V (volt)	$(E/p)_a$ $V.cm^{-1}torr^{-1}$	B $V.cm^{-1}.torr^{-1}$	A $cm^{-1}torr^{-1}$	M
600	1307	374	31	6.82×10^2
800	1754	374	31	1.20×10^4
1000	2177	598	47	33.2×10^4
1100	2391	598	47	1.25×10^5
1200	2612	598	47	4.99×10^5
1400	3047	598	47	6.88×10^6
1500	3265	598	47	27.0×10^6

(2) The electric field in the counter should be strong enough to achieve the saturation collection of ions to ensure that the pulse height for equal energy deposition is constant. This is determined by the saturation factor E/p ($V.cm^{-1}torr^{-1}$). Watt[70] determined the saturation factor for α–particles in various gases, including T.E gas (64.4% methane, 32.4 % carbon dioxide, and 3.2% nitrogen) and found E/p = 0.85 $V.cm^{-1}torr^{-1}$. The saturation factor for propane based

T.E gas used in the present work, should be similar, or at worst the same order, as the saturation factor of methane based T.E gas.

Re-arranging equation 3.11, the voltage required for the saturation collection of ions is given by:

$$V = E/p\{pr \ln a/b\} \qquad (3.13)$$

where: E/p = 0.85 $V.cm^{-1}torr^{-1}$, a = 0.0126 cm, b = 3.9 cm , p = 7.1 torr, and r = b = 3.9 cm.

Therefore the minimum voltage required is 121.8 V and this will be easily surpassed if the operating voltage is selected for the multiplication criterion above.

3.3 The principles of small volume simulation

The TEPC is designed to simulate a mammalian cell in respect to energy deposition by ionising radiation. The small cellular volume, with a typical diameter of the order of 1 μm, is achieved by operating the counter at such a low gas pressure that the total interaction cross-section for charged particles traversing along equivalent trajectories is the same in the gas as it would be a single cell. The energy deposition over each trajectory would be the same which means the following condition holds:

$$\Delta E_t = (S/\rho)_t \rho_t d_t = (S/\rho)_g \rho_g d_g = \Delta E_g \qquad (3.14)$$

where: $(S/\rho)_t$, $(S/\rho)_g$ are the mass stopping powers in tissue and gas respectively; ΔE_t , ΔE_g are mean energy loss in tissue and gas respectively; d_t , d_g are the distance travelled in tissue and gas respectively; and ρ_t , ρ_g are the density of tissue and gas respectively.

For the same atomic composition the mass stopping powers will be equivalent (see section 3.4), then:

$$d_g = \frac{\rho_t}{\rho_g} d_t \qquad (3.15)$$

For a constant volume and temperature the density of a gas is proportional to its pressure, therefore:

$$\frac{P_g}{\rho_g} = \frac{P_{NTP}}{\rho_{NTP}} \qquad (3.16)$$

where: P_g - pressure of the gas for simulation; P_{NTP}- pressure at NTP

Now substituting for ρ_g,

$$P_g = \frac{\rho_t}{\rho_{NTP}} \times \frac{\bar{l}_t}{l_{NTP}} \times P_{NTP} \qquad (3.17)$$

The mean chord length of the TEPC in the present work is $\bar{l}_t$ = 5.9 cm. The density of the propane gas used at a pressure of 750.1 torr at 20°c is $\rho_g = 1.79 \times 10^{-3}$g.cm^{-3} whereas the density of tissue is 1 g.cm^{-3} . Thus, to simulate a mean chord in tissue, $\bar{l}_t$ = 1 μm, a pressure P_g = 7.1 torr is needed.

3.4 Tissue equivalence

Tissue equivalence, or near tissue equivalence in practice, is achieved by using T.E plastic walls and a T.E gas in the sensitive volume that closely match the atomic composition of tissue (see Table 3.3). In principle the interaction cross-sections and mass collision stopping powers of tissue and T.E materials should be the same. Also, the homogeneity in atomic composition of the wall and the gas is important if Fano's theorem is to be satisfied. The theorem states that the fluence is independent of the density variation, provided that the interaction cross-sections and stopping powers of the particles are independent of density.

However, homogeneity is impractical as there in no T.E wall and gas of the same composition, and a close match is the compromise (see Table 3.3). Examples of practical considerations that limit the selection of the counter materials are: the counter's wall is the cathode which is made from a rugged machinable plastic (A-150 plastic) and this requires a high carbon content to ensure electrical conductivity; and the T.E gas must contain no elemental oxygen as this has a high electron affinity and

will reduce the gas gain by scavenging electrons. The correction factor required for some charged particles to account for the slight inhomogeneity, can be significant[66].

Table 3.2. The percentage weight of each element of three different muscle-equivalent compounds and mixtures (from ICRU 36).

	H	C	N	O
ICRU tissue, muscle	10.2	12.3	3.5	72.9
A-150 T.E. plastic	10.1	77.6	3.5	5.2
Propane based TE gas	10.3	56.9	3.5	29.3

3.5 Wall effect distortions

Distortion of the microdosimetric measurements from wall-effects can occur due to the way in which energy deposition occurs. Particles not only travel in straight lines, they can for example, scatter, backscatter and produce branches with secondary particle tracks. This gives rise to wall-effects when simulating small volumes using a geometrically large gaseous cavity surrounded by a solid wall. The wall-effects generally result in an over-estimation of the observed mean event size and an underestimation of the observed number of events because two or more events occur simultaneously in the counter when only one would occur in reality within a cell. The following are the main ways in which the wall-effect arises[71,72]: (i) the δ-ray effect which is where δ-rays which would normally miss a cell traverse the counter together with the primary charged particles; (ii) the re-entry effect which is where after crossing the counter the charged particle is scattered back into the counter whereas in reality the back-scattered particle would miss the same cell; (iii) the V-effect which is where several charged particles from nonelastic nuclear

interaction intercept the counter, but in reality only one would intercept the cell; (iv) the scattering effect which is where uncharged particles produce two or more charged particles which cross the counter, whereas only one would intercept the cell.

To reduce the problem of wall-effects, wall-less TEPCs have been developed[66], but their construction is technically considerably more difficult than that of walled counters and their description is beyond the scope of this thesis.

3.6 The counting system and electronic set-up

A schematic representation of the counting system is shown below in Figure 3.2 below:

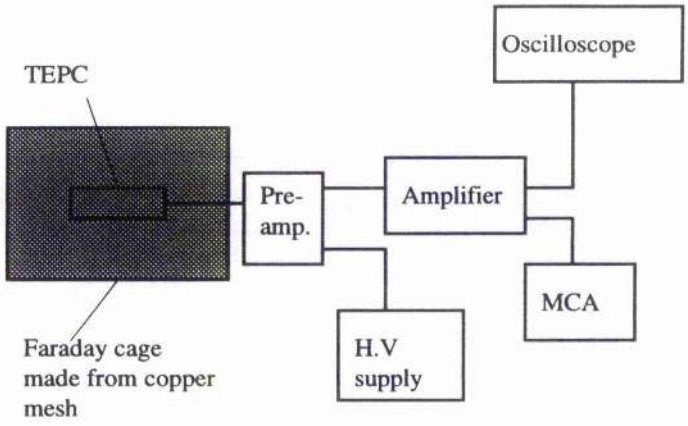

The Faraday cage was used to reduce electromagnetic interference in the counter which is particularly strong in the treatment room of a LINAC. The following components were all from EG&G Ortec: the pre-amplifier (type 142pc), the high voltage supply (type 572) and the multichannel analyser (Model 100T which utilises ADCAM ANALYST software called 'Maestro'). The amplifier was the spectroscopic Tennelec type 243. The linearity of the pre-amplifier and amplifier was checked using a precision pulser (EG&G Ortec type 448).

The monitoring of the pulses from the counter was performed via the oscilloscope. These pulses could then be adjusted for height and pulse shape by the

amplifier to produce positive leading bi-polar pulses with a 3 μs rise time that were suitable for the ADC input of the MCA. The conversion gain of the MCA was set to 512 channels and the maximum acceptable voltage pulse was 12 V.

Sub-spectra were collected for up to three amplifier gain settings. These energy deposition spectra were merged and converted into microdosimetric spectra using a specially written computer programme, "ymicro.bas", that is run in Microsoft Basic.

3.7.0 Calibration in Lineal Energy of TEPC Microdosimeters

The calibration of the TEPC can be the greatest source of uncertainty in microdosimetric measurement, and although the TEPC in this work was fitted with a thin beryllium window to allow for calibration by soft X rays, other calibration methods have been examined and explored.

The problem of calibrating TEPC's in lineal energy is essentially one of converting the produced charge (which is directly proportional to the pulse height of the signals) into energy deposited within the counter by the radiation event(s). There are various methods to do this, of which the single event calibration methods that all involve depositing a precisely known quantity of energy within the counter, are the most useful. The conventional methods for calibration, reviewed by Dietze *et al.*[73], are summarised below. An inherent calibration method for electrons has been developed in the present work as a more accurate and convenient alternative. For heavy particles, the 'proton-edge' method which has been studied elsewhere[74,75] has been initially re-appraised and a new calibration curve for a variety of simulated diameters has been produced. It is found that the extrapolated dose-weighted lineal energy provides a more rigorous calibration point (section 3.7.2).

Multiple event calibration of TEPCs is also possible. However there are many uncertainties with this method. It involves the use of an external photon source

delivering a precisely known dose in the wall of the counter adjacent to the gas cavity (assuming the Bragg-Gray principle is fulfilled) This enables the observed energy deposition spectrum to then be calibrated in terms of lineal energy. The photon source is convenient to use, but there are many corrections involved in calculating the dose supplied. These include corrections for wall attenuation, for in-scattering and for the non-uniformity of the field[76]. Extrapolations are also required for the lower and upper limits of integration[77]. Single event calibration is more accurate.

3.7.1 Single event calibration

Let ε_c be the energy event size of single particles with lineal energy y_c and the resultant pulse height be h_c. Then, y, the lineal energy of any other event that produces a pulse height, h is given by:

$$y = y_c .(W/W_c).(h/h_c) \qquad (3.18)$$

where W(eV) is the mean energy required by the measured radiation to produce one ion pair and W_c(eV) is the mean energy required by the calibration radiation to produce one ion pair.

The conventional calibration methods involve α-particles, or soft monoenergetic X rays[73]. However, there are many uncertainties associated with these methods[138]. With the α -particle technique, practical difficulties arise because the source has to be mounted internally, and then a mechanical facility, a shutter for example, is required for switching the source on and off. The α -particles are usually emitted from the source and then collimated through a small borehole to cross the cavity along its diameter. Schrewe *et. al.*[79] recommended α-calibration as being both fast and reproducible, but they found that the overall uncertainty was about 10%. The three major contributions to this uncertainty are: (1) large discrepancies in the stopping power data (used to calculate the average event

size) for TE gas; (2) a reduction in the effective α -particle energy compared with the nominal value due to self absorption in the source layer; (3) uncertainty in the exact portion of the α-particle track expended within the detector's sensitive volume. Values of lineal energy are approximately 90 to 100 keV.μm^{-1} and consequently considerable extrapolation is required to determine the lineal energies of the electron component in the region of 0.1 to 20 keV.μm^{-1}.

Sometimes other indicators can be used to estimate lineal energy for the calibration of fast neutron y spectra. The latter have characteristic features associated with the induced proton or α-particle components, such as the 'edges'. Typical y values for these features are determined by the extent to which the LET maximum (respectively ~100 keV.μm^{-1} and ~175 keV.μm^{-1}) is included in 'crosser' tracks. The use and the rigorous quantification of these features for calibration purposes is rare (see reference (78) and section 3.8.).

For the calibration of the electron component, soft X ray sources that produce a total absorption photopeak, are used as the typical calibration radiation. For simulated diameters greater than 2 μm, ^{55}Fe (E_k = 5.89 keV) can be used, but when the diameter is of the order of 1 μm even softer X rays such as the K_α-line of aluminium (E_k = 1.49 keV) are needed. At these low energies, the X rays are readily absorbed, thereby causing practical difficulties in providing access for the calibration radiation to the sensitive volume of the counter. Hence either the source must be mounted internally, or if an external source is used, a thin entrance beryllium window with low absorbency is required.

3.7.2.0 Inherent electron calibration using gamma rays

In this section it is demonstrated that the maximum observed dose-weighted lineal energy of the photon generated electron spectrum can serve as a reliable and reproducible method of self-calibration without the need for specified sources[80].

The method is based on the knowledge that, in the absence of electron backscatter, which is described in detail by Dahmen *et al*[81], the maximum energy event sizes for electrons are caused predominantly by 'exact stoppers' i.e. for electrons with a mean projected range that exactly equals the diameter of the sensitive volume of the TEPC. Results from analytical calculations (shown in Figures 3.4, 3.5, 3.6) show that it is not the 'exact crossers', but the maximum 'stoppers' that determine the slope of the 'dose distributions' in y at large y values. The calibration point is the extrapolated y value obtained from the large y value electron events seen in the dose distribution in lineal energy spectrum for photon interactions. For a microdosimeter having 1 μm simulated diameter, the energy of the 'maximum stopper' electrons is about 8 keV in tissue-equivalent (T.E) gas. Thus, the method is applicable provided there is an external photon field capable of releasing photo- or compton electrons with energy greater than about 8 keV. For the usual practical circumstances, under conditions of charged particle equilibrium, this is typically the case e.g. in photon fields and in mixed γ-n fields. Alternatively, a suitable external field of γ-rays from a source such as ^{241}Am,^{137}Cs, or ^{60}Co will suffice. Microdose spectra for these sources have been calculated using a form of Caswell's equation[93] modified for electrons, whereby their projected ranges and effective stopping powers are included. These spectra are shown in Figures 3.4, 3.5, and 3.6 for a 1 μm simulated diameter in water. Knowledge of the source activity is unnecessary. The calibration point at around 13 keV.μm^{-1} for a 1 μm simulated diameter, is of a more convenient magnitude than that obtained conventionally using soft X rays or α–particles.

3.7.2.1 Calibration procedure

The experimental dose-weighted lineal energy spectrum due to photons when displayed on a log-linear graph is characterised by a final linear portion, the 'electron-edge' that can be extrapolated to intercept the abscissa at a maximum value of y (see

Figure 3.3. A typical dose distribution in lineal energy from a high energy photon source

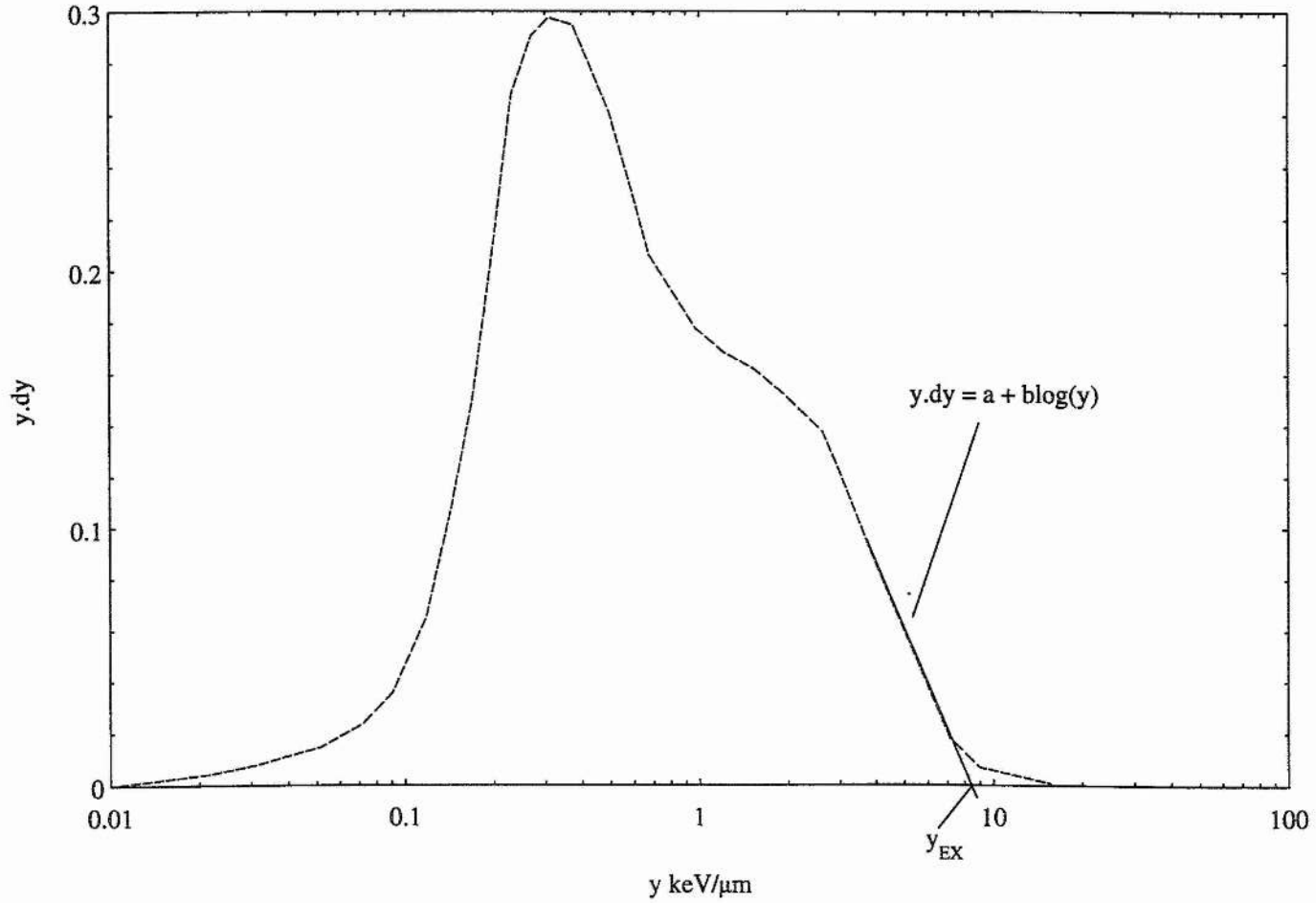

Figure 3.4 Calculated dose distribution in lineal energy

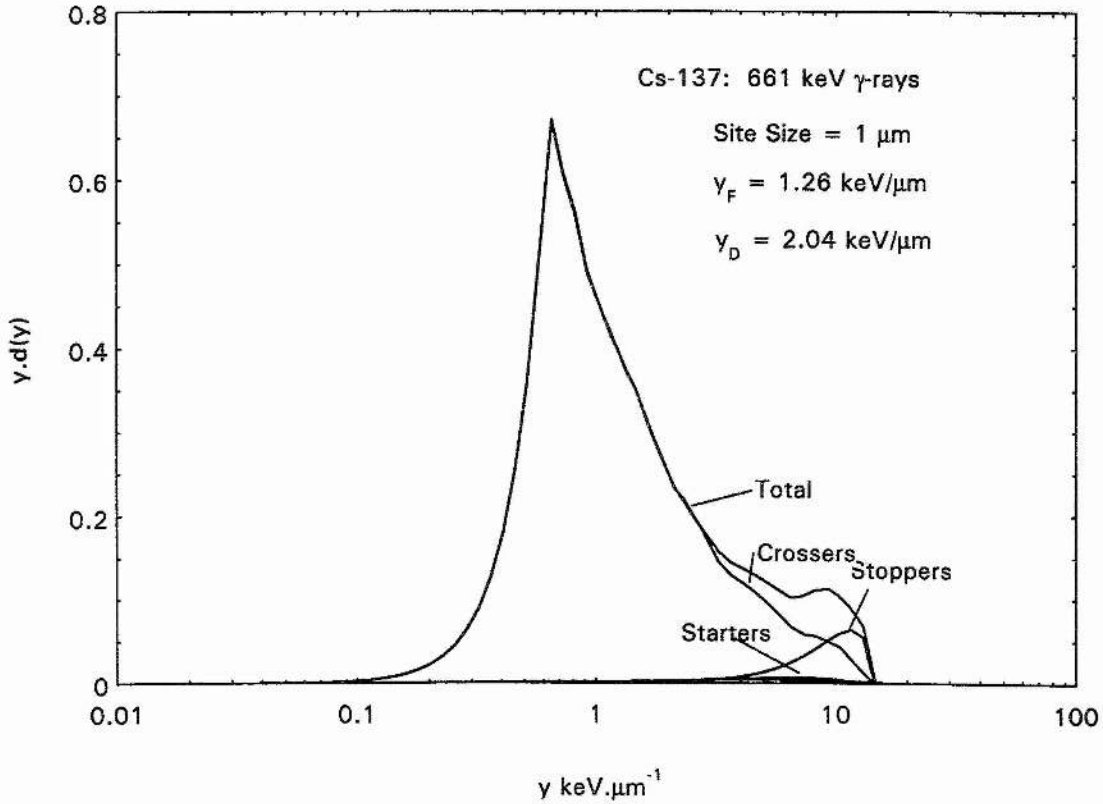

Figure 3.5 Calculated dose disitribution in lineal energy

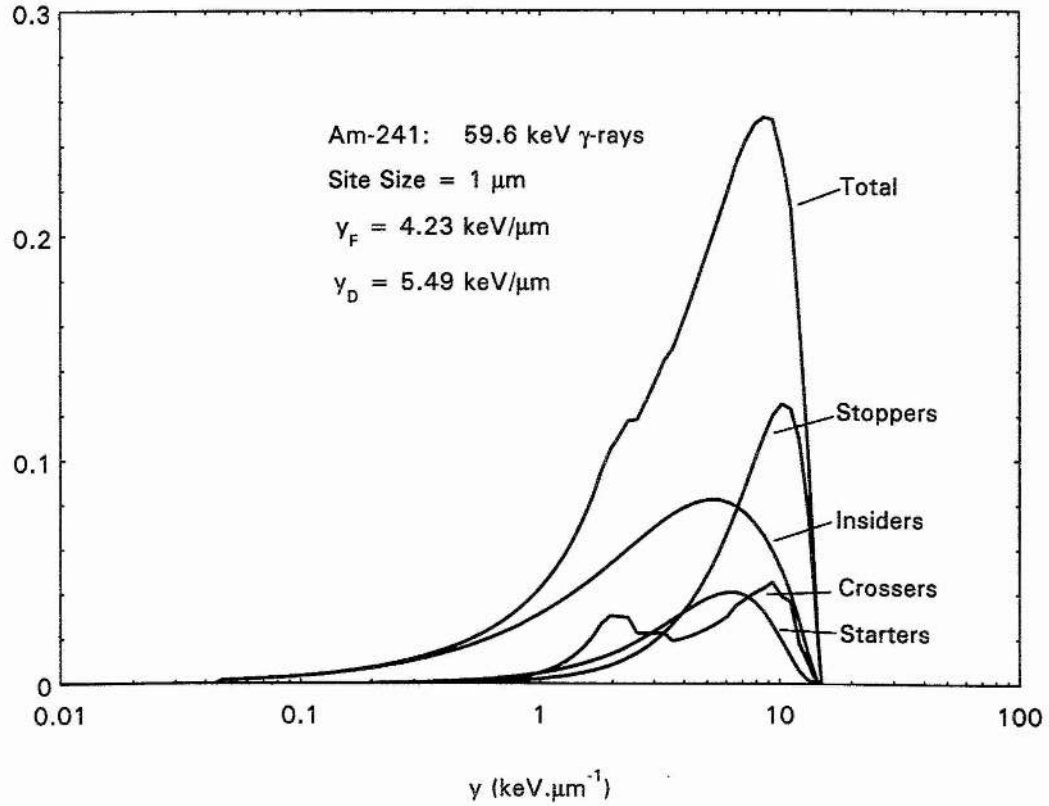

Figure 3.6. Calculated dose distribution in lineal energy

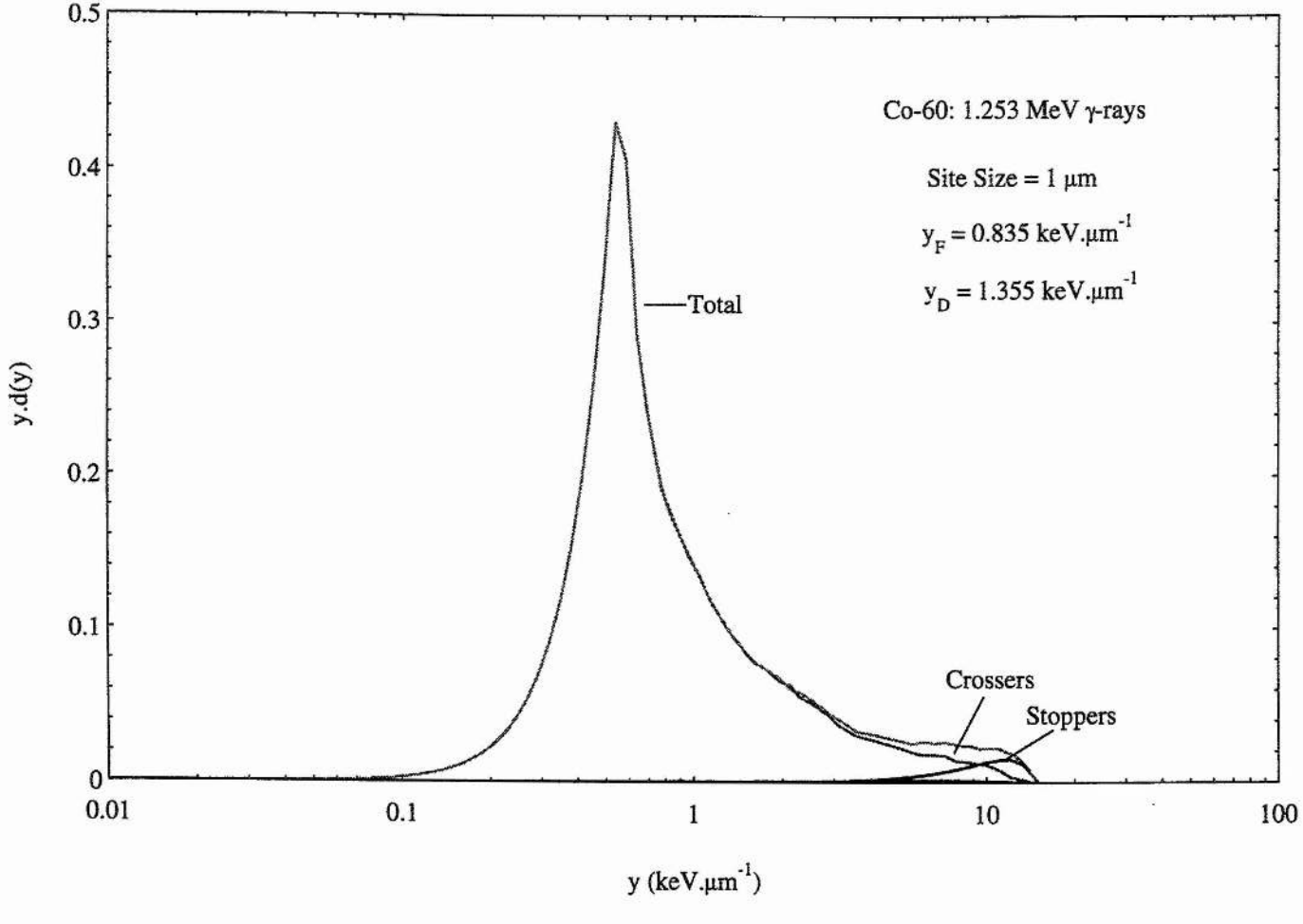

Figure 3.3). The extrapolation, by least squares 'best-fit' of an equation of the form y.d(y)= a + blog(y), of the linear portion of the curve onto the abscissa corresponds to the maximum lineal energy value of the maximal 'stopper' electrons in the counter. The extrapolated value of lineal energy, denoted here by y_{EX}, is given by $y_{EX} = 10^{(-a/b)}$ where the coefficients a and b are obtained from the fitted curve.

Each microdosimetric spectrum was calibrated in the following iterative manner. Firstly, a preliminary dose-weighted lineal energy, d(y), spectrum was calculated from the observed pulse height spectrum using an arbitrarily allocated calibration factor (say 10 keV.μm^{-1}) for the abscissa. Then an extrapolation of the curve at the large y values was carried out as previously explained, to obtain a reading for lineal energy. From the known channel number of this intercept, the actual value of y_{EX} can be allocated using the calibration data shown later in Figure 3.8. Repeating the calculation of the d(y) spectrum using the newly determined calibration factor, yields the final result. The whole procedure can be easily incorporated into the computer programme used for analysis of the experimental data.

3.7.2.2 Justification of the method

From the theoretical components of the microdose spectrum shown in Figures 3.4, 3.5 and 3.6 it is clear that the maximum event sizes are caused predominantly by 'stopper' electrons. To find the mean lineal energy of the 'exact stoppers' knowledge is required of the energy deposited which, in turn can be determined from the known CSDA range-energy relationship and a 'detour' factor to account for the increased energy deposition due to the zigzag nature of the electron tracks. The 'detour' factor is accommodated by use of the mean projected range. Exact stopper' electrons have, by definition, a mean projected range in the sensitive volume equal to the diameter. To good approximation the mean projected range is

equal to the median range which is denoted by R_{50} (see Appendix 1 for range definitions). To find the energy of electrons with a range R_{50}, it is first necessary to find their R_{csda} because range-energy tables exist for the latter type of range. Available data on mean electron ranges is limited especially at low electron energies. However, Iskef *et al.*[82] have analysed experimental transmission curves in different media from various authors, and by using a good empirical representation of the transmitted fraction, they have obtained a general expression for R_{50} ranges in terms of extrapolated ranges for electrons with energy from 20 eV up to 10 keV. Some of the values of the ranges obtained in organic media have been plotted in Figure 3.7. For electrons with energy from 2 keV up to 60 keV, values of the mean projected range in beryllium and in carbon have been calculated from an equation for the transmission fraction derived by Vyatskin *et.al*[83,84] together with data from Fitting[85] for the transmission parameter and maximum ranges (the maximum ranges that were used by Fitting are the 1% residual transmission ranges. Iskef *et.al* found these to correspond well with the extrapolated ranges above 1 keV). These derived values for the mean projected range have also been plotted in Figure 3.7 and can be represented by the following relationship:

$$R_{50} = 0.4842\ (R_{ex})^{1.093} \qquad (319)$$

valid for ranges given in micron, over the energy interval of 200 eV to 60 keV.

For low-energy electrons, R_{ex} is the quantity which most closely corresponds to the R_{csda} range in materials with Z-values ranging up to that of silver[86]. Thus, assuming that the two quantities are nearly equivalent, it is a simple matter to find the energy of electrons with R_{csda} equal to R_{ex} using range-energy tables such as those of Watt[87]. Then the extrapolated lineal energy, y_{EX}, may be written as:

Figure 3.7. The mean projected range against the extrapolated range

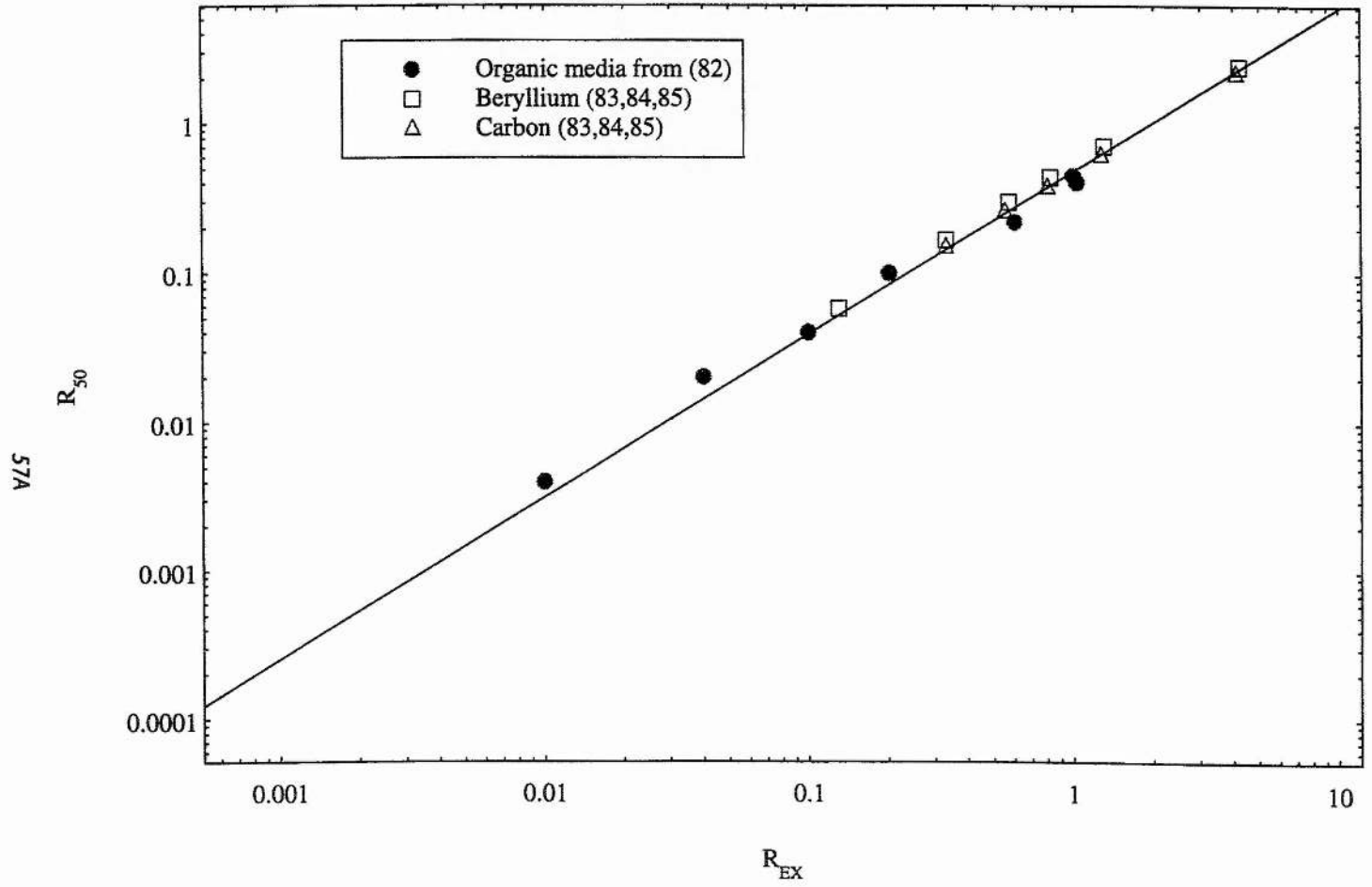

$$y_{EX} = \frac{\varepsilon}{\bar{d}} \qquad (3.20)$$

where ε is the energy of an electron which has a median range, R_{50} , equal to the counter's diameter.

The microdose distribution spectra produced by photons are dominated by the shape of the charged particle equilibrium spectrum, the range and energy straggling of the electrons and the chord length distribution in the counter. Factors such as the Fano factor, multiplication statistics, electronic noise and other contributions to the counter's energy resolution are of lesser significance in determining the shape at maximum y-values [66].

3.7.2.3 Experimental verification

Results were obtained using experimental data taken from Kliauga and Rossi[88]and Kliauga and Dvorak[89] showing the dose distribution in lineal energy due to γ-rays for different simulated diameters. The authors used soft X ray calibration and spherical Rossi-type wall-less TEPC's. The FWHM resolution of their counters for soft X-ray calibration were 34% and 33% respectively.

As a good comparison[66] a cylindrical TEPC containing a tight fitting sleeve of A-150 tissue-equivalent (TE) plastic housed in an aluminium container was used. The TE sleeve was of thickness (~1cm) sufficient to give CPE (charge particle equilibrium) for ^{60}Co photons, and the counter was filled with propane-based TE gas. The TEPC was calibrated using 5.89 keV Mn K_α X rays from an ^{55}Fe source with a FWHM resolution of 37%. Microdosimetric spectra showing the dose distribution from a ^{137}Cs (662 keV photons) source were collected for different simulated diameters. The effective mean chord length of the cylinder, was assumed to be equal to that of a sphere with an effective diameter, d, where:

$$d = \frac{3}{2}\bar{d} \qquad (3.21)$$

Figure 3.8. Experimental dose distribution in lineal energy

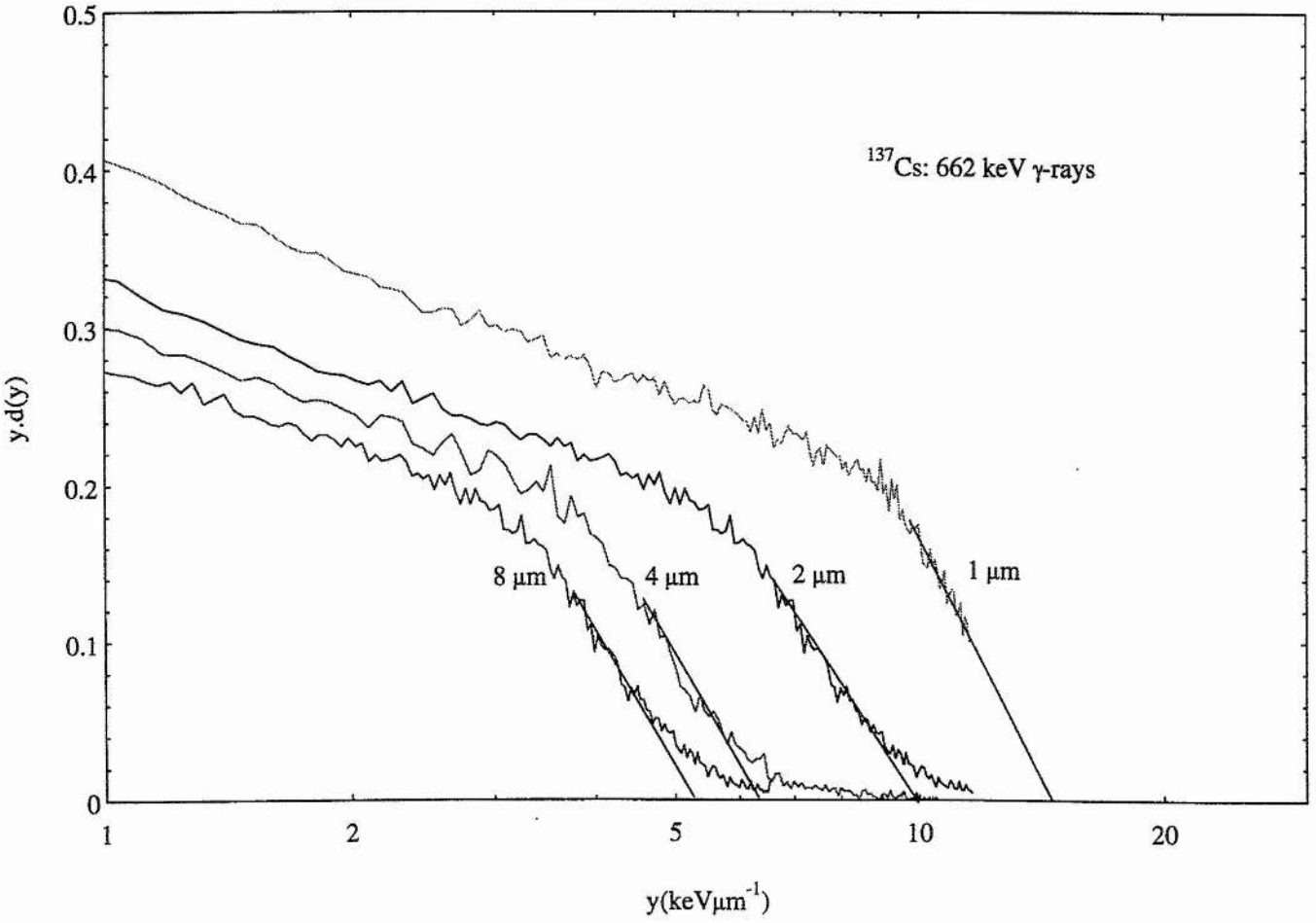

Values of y_{EX} were determined from the collected microdosimetric spectra of the cylindrical TEPC and from the examples of microdosimetric spectra taken from the literature[88,89]. These experimental values are plotted against the simulated diameters of the cavities in Figure 3.9. The errors shown (±7% for a 1 μm site size) decrease with increasing site size. They are the uncertainties in determining the position of the intercept y_{EX}, from the best-fit extrapolation at each simulated diameter. The latter is the main contribution to the error and is due to the rapid dependence of y_{EX} on the site diameter as may be seen in Figure 3.9.

Good agreement is obtained between the experimental points and fitted curve of the theoretical points in Figure 3.9 for simulated diameters up to 8 μm. The results from the literature[88,89] using spherical wall-less TEPC's lie on the fitted curve as closely as the experimental results from the walled cylindrical counter, showing that for a given simulated diameter, y_{EX} is the same for walled and wall-less TEPC's. The small number of lineal energy events recorded above y_{EX} are probably due to electron backscatter along the diameter. Electron backscatter is estimated to be about 4% for low-Z, tissue-equivalent materials.

The use of the theoretical curve plotted in Figure 3.9 enables inherent calibration, in units of lineal energy, of TEPC's simulating diameters of between 0.48 and 8 μm. If the TEPC is to be used for measurements of radiations other than photons then the appropriate W-value correction factor should be applied[90]. However, for mixed fields it is often difficult to identify energy deposition events due to specific radiations as there is frequently considerable overlap, and it is usual to assume a constant W-value over the entire spectrum. This would lead to an error of 6% if the counter is calibrated using α-particles and then used to measure low-LET microdosimetric spectra. This error increases to 15% when low energy photons are used for calibration of a counter used in heavy ion fields[90].

Figure 3.9. The 'universal' calibration curve

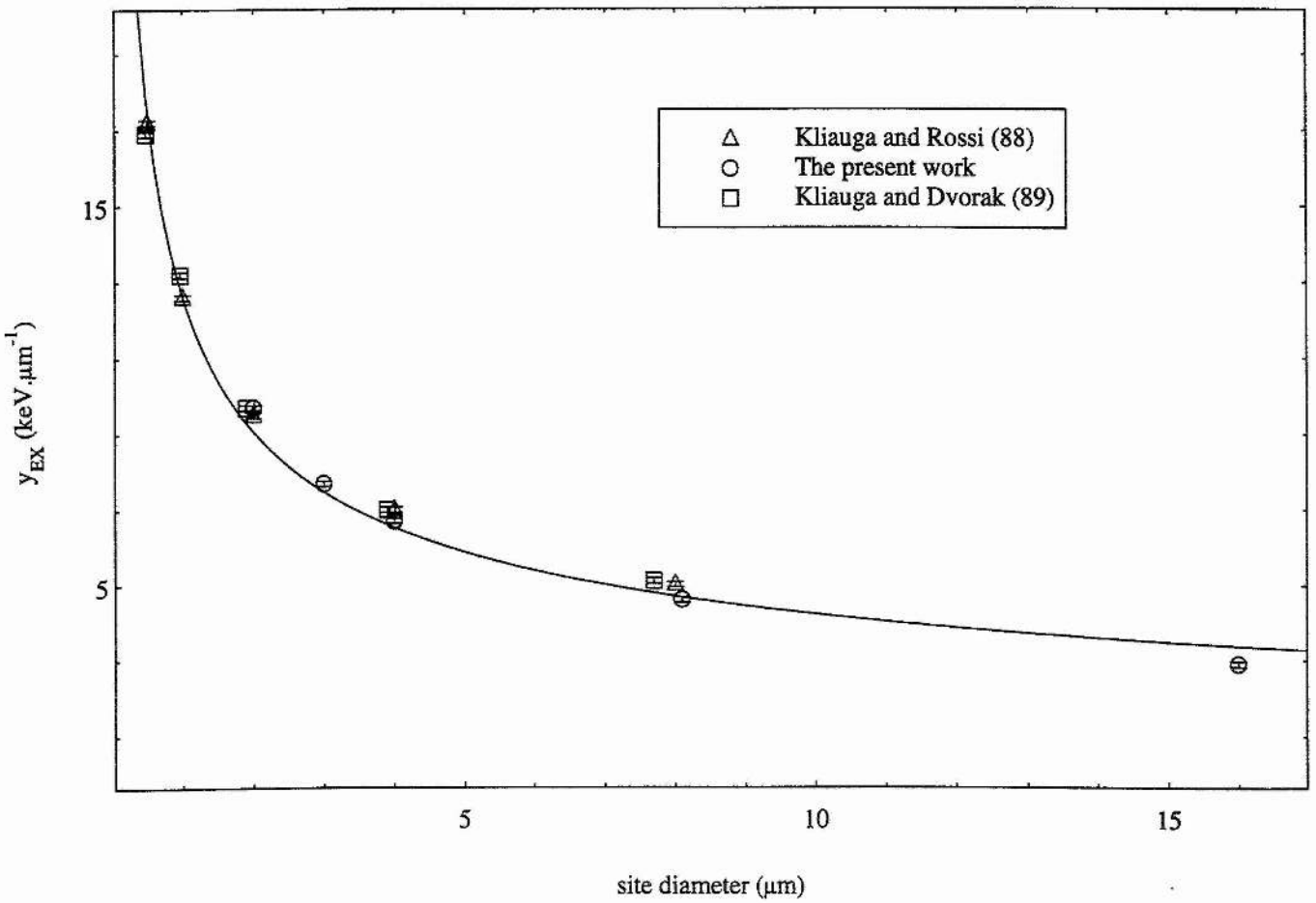

The microdosimetric spectrum of a ^{252}Cf source sealed in an aluminium housing has been measured using the aluminium cylindrical TEPC simulating a site diameters of 2 μm and 3 μm. For the purpose of comparison (with the 2 μm simulated diameter) calibration was carried out via the three calibration methods: ^{55}Fe soft X ray calibration, inherent electron calibration, and proton-edge calibration (see section 3.7). The first two methods mentioned have been corrected for the different W-values of protons, 27.9 eV, and electrons, 26.1 eV[74]. The dose distributions in lineal energy are shown are very closely matched Figure 3.10. The mean values and $\bar{y}_d$ are compared in Table 3.3 below:

Calibration method	$\bar{y}_d$ (keV.μm^{-1})	Error
X ray	41	± 10%
Inherent electron	43	± 10%
Proton edge	43	± 6%

The agreement in $\overline{y_d}$ values between the three methods is good, with the spread less than 5%. The maximal systematic uncertainty $\overline{y_d}$ is expected to be ±10%[66] and this is the value attributed to the error for the first two measurements. Although the systematic analysis of the uncertainties of microdosimetric spectra has been rarely tackled previously[66], Waker[66] has examined the uncertainties of $\overline{y_d}$ measurements utilising proton edge calibration. In cylindrical TEPCs simulating 2μm diameters, he estimated the overall uncertainty to be 6%; this is the error attributed to the proton-edge calibration measurement of $\overline{y_d}$ above.

The inherent electron calibration method is particularly convenient for use in radiation protection where it is a simple matter to irradiate the counter from a high energy photon source before measurements are carried out in the unknown field.

Figure 3.10. Dose distribution in lineal energy for ^{252}Cf source

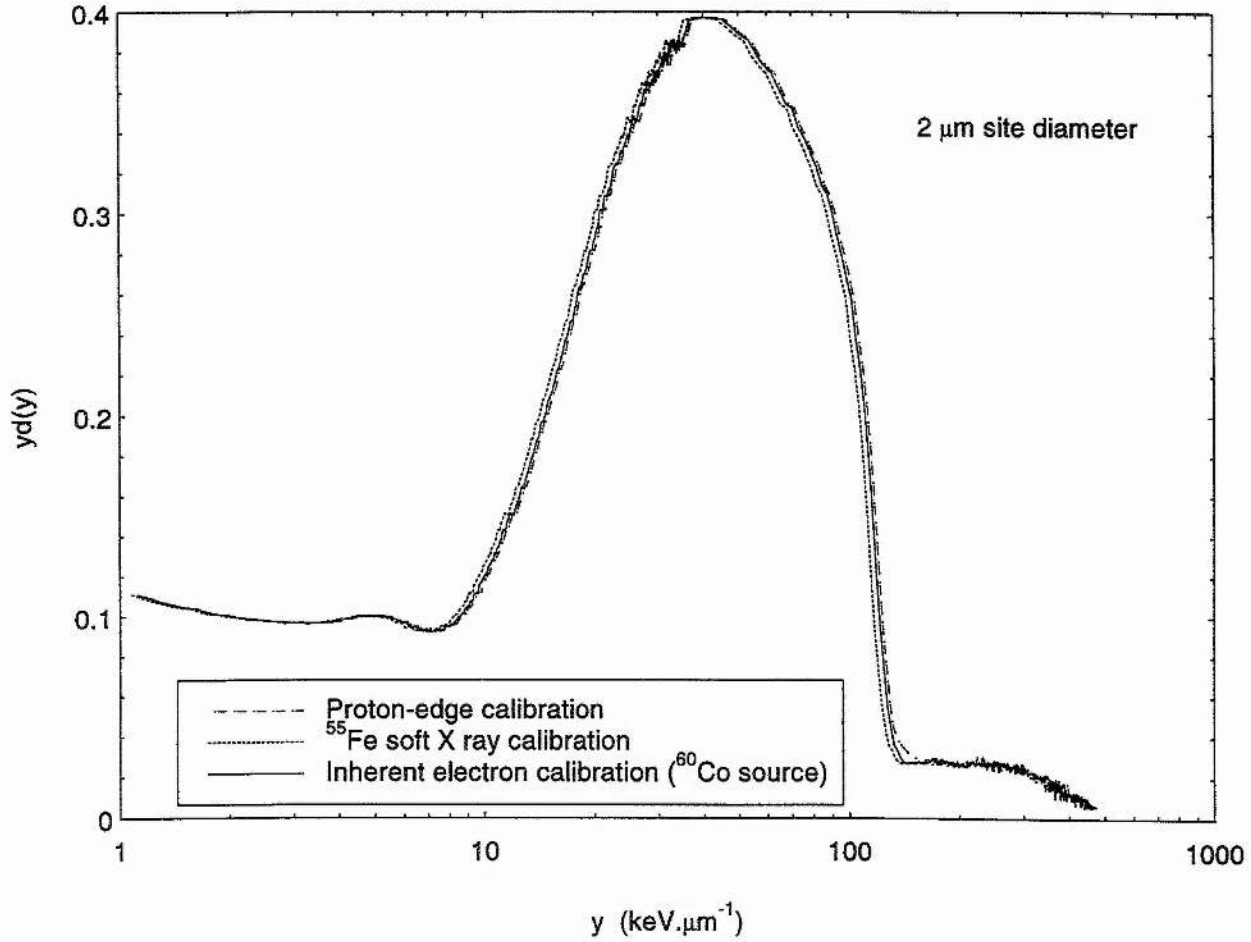

This method enables calibration, in units of lineal energy, to an uncertainty of $\leq \pm 7\,\%$, it is reproducible and in good agreement with other calibration methods.

3.8.0 Proton-edge calibration

The 'proton-edge' is the sharp cut-off at the proton y values of the dose-distribution in lineal energy (see Figure 3.11). This cut-off is often a very distinctive feature of the recoil spectrum in fast neutron spectra and its position can be used for calibration[74,75]. This calibration point occurs when the maximum energy is deposited within the counter by a 'maximum crosser' recoil proton (i.e. one that maintains a maximum possible average stopping power over the diameter - the maximum chord length). As previous attempts to determine the proton-edge are few in number and inconsistent in interpretation, it was decided to conduct a re-appraisal. The determined values are shown in Table 3.4 together with those calculated by others.

It is accepted that the proton edge is attributable to events which deposit maximum energy along the diameter of the counter. This, together with the knowledge that such events must include the stopping power maximum, form the basis of the quantitative approach adopted in the following section.

3.8.1 Methods for quantification

The maximum energy deposition, $\varepsilon_{d,max}$, occurs when a recoil proton of energy, denoted here by E_R, crosses the diameter of the counter and sustains a maximum average stopping power to deposit the maximum energy. The total collision stopping power of protons in propane based T.E. gas is shown against range (R_{CSDA}) in Figure 3.11 [91]. It can be seen that the stopping power maximum is at 101 keV.μm^{-1} for a proton with a R_{CSDA} of about 1 μm which corresponds to an energy of between 75-80 keV.

Figure 3.11. ^{252}Cf dose distribution in lineal energy

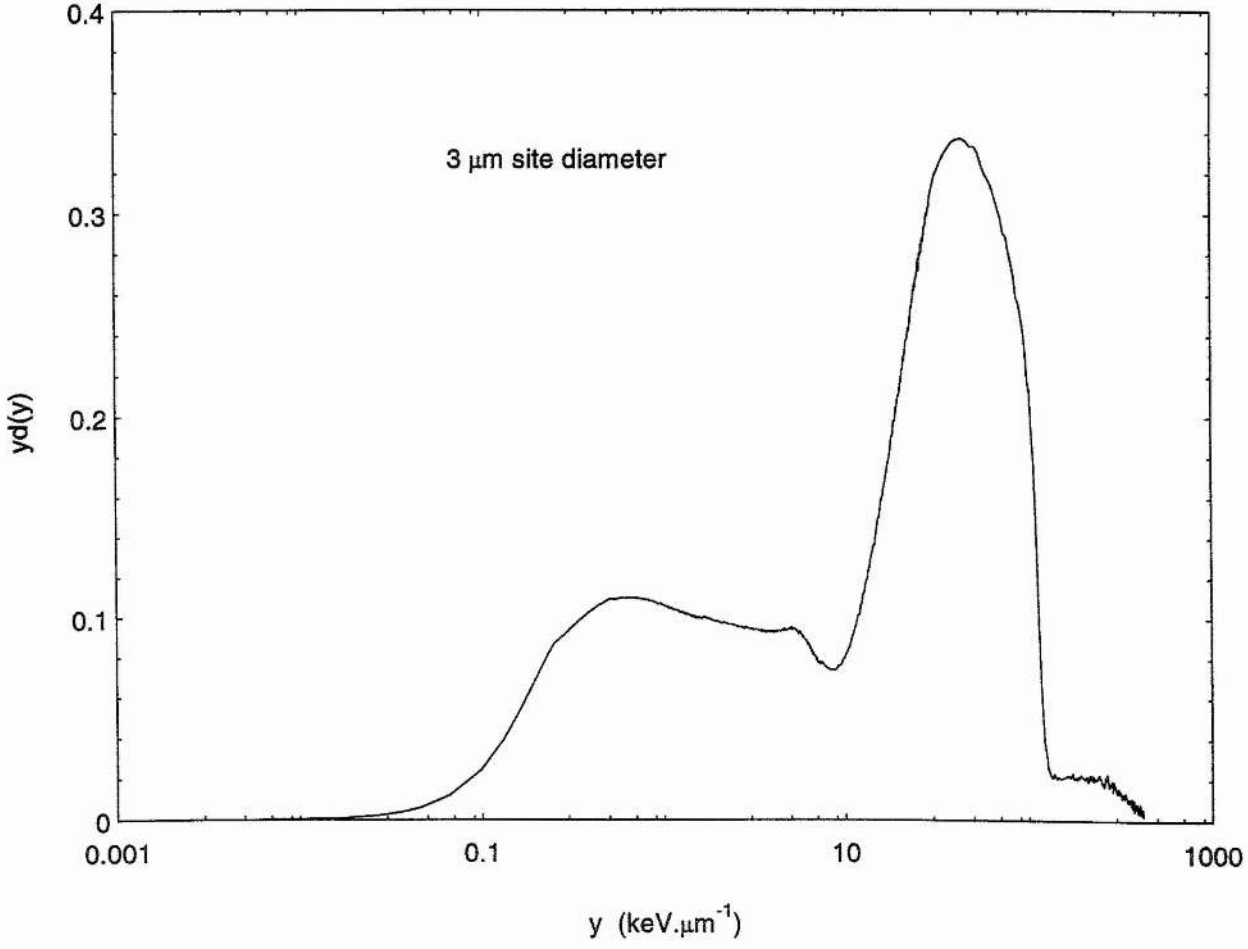

A proton of incident energy, E_R, emerges with energy, $E_{(R-d)}$, after crossing the diameter , d, of the counter energy, ε_d, deposited in the counter of diameter, d, is given by the implicit relation:

$$\varepsilon_d = E_R - E_{(R-d)} \tag{3.22}$$

where R and R-d are the respective ranges. Now, the condition that ε_d will be a maximum is:

$$\frac{d\bar{\varepsilon}_d}{dR} = 0 \tag{3.23}$$

This will occur when the stopping power of the incident proton is equal to that of the residual proton (which ensures that the stopping power maximum is fully included within the cavity). This condition is given by:

$$\frac{dE_R}{dR} = \frac{dE_{(R-d)}}{dR} \tag{3.24}$$

The mean energy deposited across the diameter, $\bar{\varepsilon}_d$, is given by the area, A, under the stopping power curve (see Figure 3.12) and this is related to the range, R, by:

$$A = \bar{\varepsilon}_d = \int_R^{R-d} -\frac{dE}{dR} dR = \int_R^{R-d} f(R) dR \tag{3.25}$$

Two polynomial curves were fitted about the stopping power maximum to obtain f(R). Values of ε_d were computed for a variety of simulated diameters by the numerical integration of (3.25) (see Figure 3.13.)

Alternatively, an empirical method to determine $\bar{\varepsilon}_d$ is: (1) plot the initial energy of the proton, E_R , as a function of range, R, $\leq$ 10 μm and fit with a polynomial spline[91] (2) read-off the energy of the residual proton, E_{R-d} at range (R-d); (3) calculate ε_d from equation (3.2); (4) plot $\bar{\varepsilon}_d$ against R. The maximum value $\bar{\varepsilon}_{d,\max}$ can then be read off.

Figure 3.12 Proton stopping power in propane based T.E gas

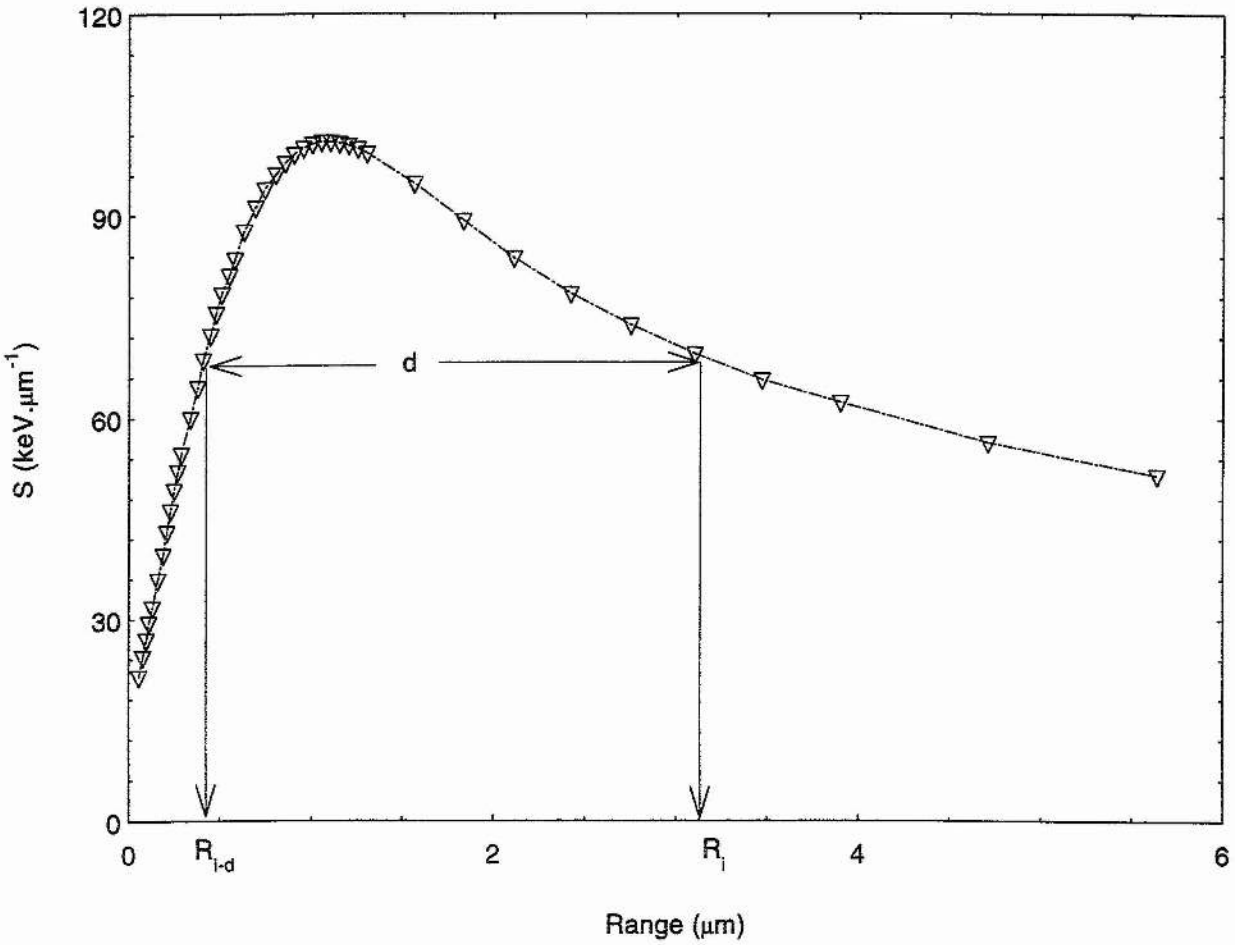

Figure 3.13 The energy deposition by protons of different energies crossing a given diameter

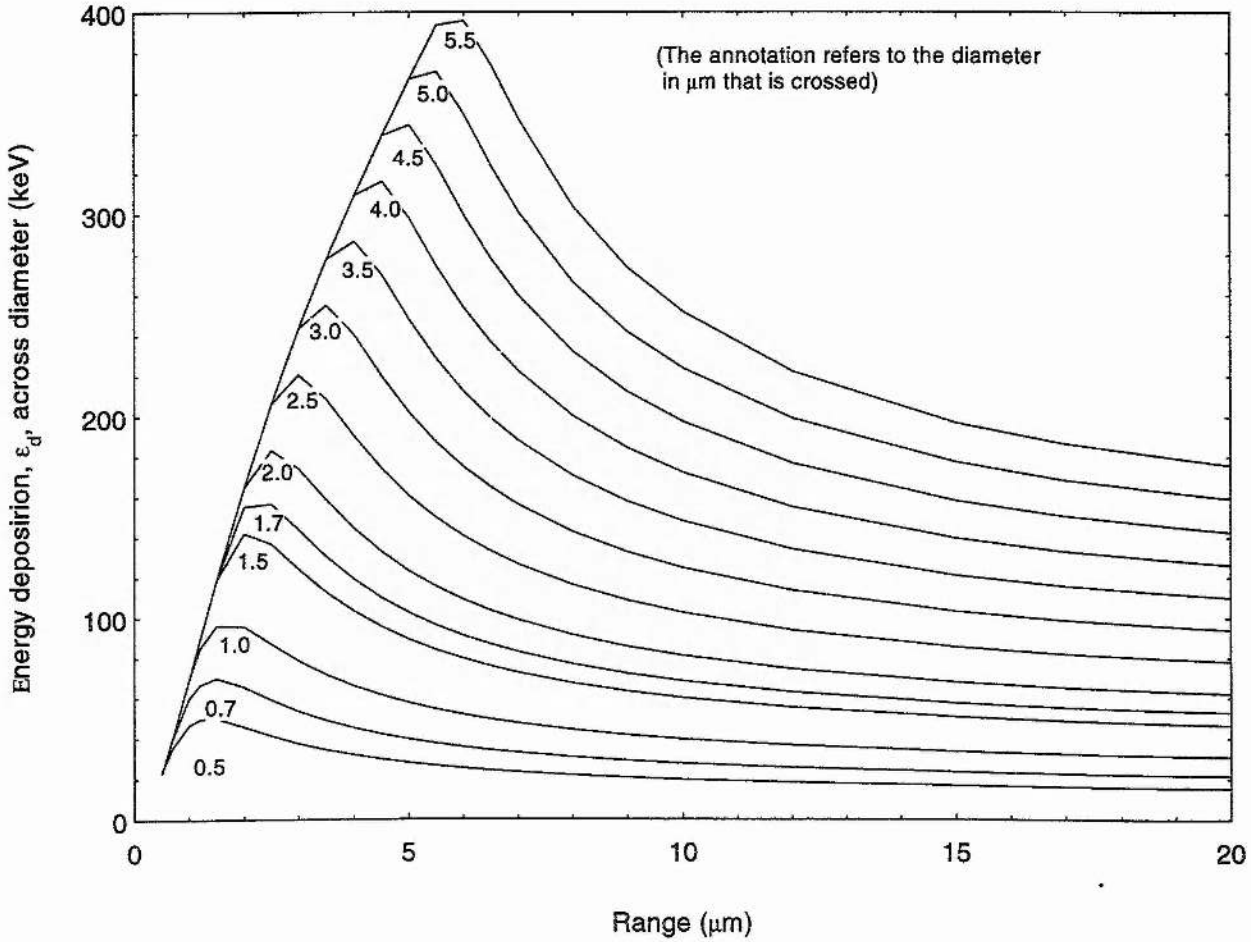

As $\bar{\varepsilon}_{d,\max}$ is the maximum limit of the stochastic variable the energy imparted, ε, the variation about which mainly depends on the chord length distribution, range straggling and energy straggling, the maximum lineal energy event due to proton recoils is given by:

$$y_{d,\max} = \frac{\bar{\varepsilon}_{d,\max}}{\bar{d}} \qquad (3.26)$$

$y_{d,max}$ is plotted against simulated diameter in Figure 3.14 the values for which are given in Table 3.4 .

The theoretical values in Table 3.4 are in excellent agreement and the largest difference which is for the 5 μm diameter is just 2.7%. The uncertainties in $y_{d,max}$ depend upon, and will be very similar to the uncertainties in the stopping power data (within a few percent) and will be greatest for small diameters (under about 1 μm) when the energy deposition is small. This occurs for protons of energy of between 75-80 keV at the Bragg peak when the uncertainty in the stopping power is approximately 10-15%[91]. Above about 1 μm the uncertainty will reduce to between 5-10%.

The theoretical values in Table 3.4 are also in good agreement with the experimental values of Srdoc[92] from measurements taken in a neutron field using different simulated diameters.

The 'proton-edge' has been satisfactorily quantified above, however the interpretation of where the maximum lineal energy, $y_{d,max}$ should be located on the dose-distribution in lineal energy spectrum differs among various authors. The location of the proton-edge is considered in the next section.

3.8.2 The position of the 'proton-edge'

The position of the 'proton-edge' (for convenience denoted onwards as 'y_p'), although never defined, is taken as the mid-point of the final linear portion of the

proton recoil peak (see Figure 3.15) by Pihet and Menzel[74], and Waker[75]. It is argued in the present work that the point, denoted here by y_{EX}, at which the extrapolation of the final linear portion intercepts the abscissa (in analogy to the inherent electron calibration method) is a better representation of $y_{d,max}$.

If 'y_p', is taken as the calibration point $y_{d,max}$, then it is necessary to explain the cause of lineal energy events that exceed 'y_p' by on average 19.9% (see Table 3.5) at y_{EX}. Range straggling, as quantified by the detour factor, for energies at the stopping power maximum and above, could only increase $y_{d,max}$ by about 9.1%[91]. The resolution of the counter even for a simulated diameter of 1 μm for protons of energy of around 100 keV is typically around 10% (not forgetting that the resolution improves with an increase in energy deposition). Combining these two factors by summing in quadrature only gives 13.5%.

Fast neutron spectra have been taken from the literature in order to investigate the relationship between y_{EX} and 'y_p', and to see which one relates better to other calibration methods (given by the percentage error between these two points on the spectrum and $y_{d,max}$). This data was taken from the dose distribution in lineal energy spectra and is given in Table 3.5 (together with two sets of data from 'proton-edge' calibration which are there just to illustrate the degree to which 'y_p' can exceed y_{EX}). (The difference between y_{EX} and $y_{d,max}$ as a percentage of $y_{d,max}$ is denoted by σ_{EX}, while σ_p denotes the variation between 'y_p' and $y_{d,max}$ as a percentage of $y_{d,max}$). For the measurements made with 2 μm simulated diameters, σ_{EX} and σ_p are approximately 4% and 13% respectively, and if the two measurements at 1 μm are included the mean values of σ_{EX} and σ_p are 6% and 12% respectively.

From the preceding results it is clear that y_{EX}, the intercept of the extrapolation of the final linear portion of the proton recoil peak, should be taken as the proton-edge with a value of $y_{d,max}$. In summary, for a 2 μm simulated diameter the proton-edge was found to be at 137 keV.μm^{-1} with an accuracy of ± 4 %. More

d (μm)	Pihet and Menzel[74] $y_{d.max}$ (keV.μm^{-1})	Waker[75] $y_{d.max}$ (keV.μm^{-1})	Present work $y_{d.max}$ (keV.μm^{-1})	Srdoc(92) $y_{d.max}$ (keV.μm^{-1}) Experimental
0.05			151.5	
0.5			149.1	
1	144.9		145.2	152 ± 5
2	134.8	136.0	136.7	133 ± 4
3			127.0	
4			118.1	114 ± 3
5	108.8		111.7	

Table 3.4

Figure 3.14 Proton-edge calculated for various simulated diameters

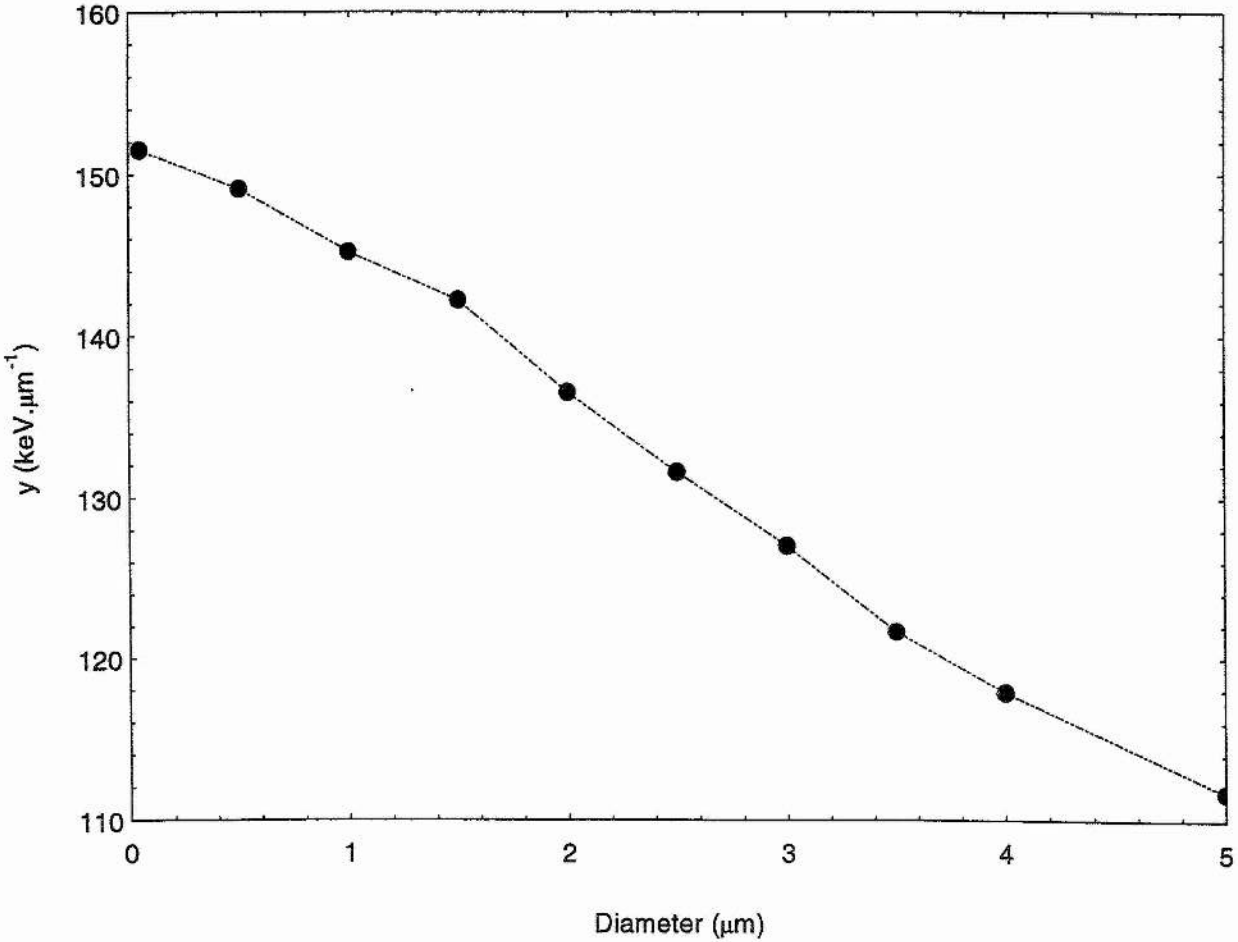

Figure 3.15. Dose distribution in lineal energy for ^{252}Cf source

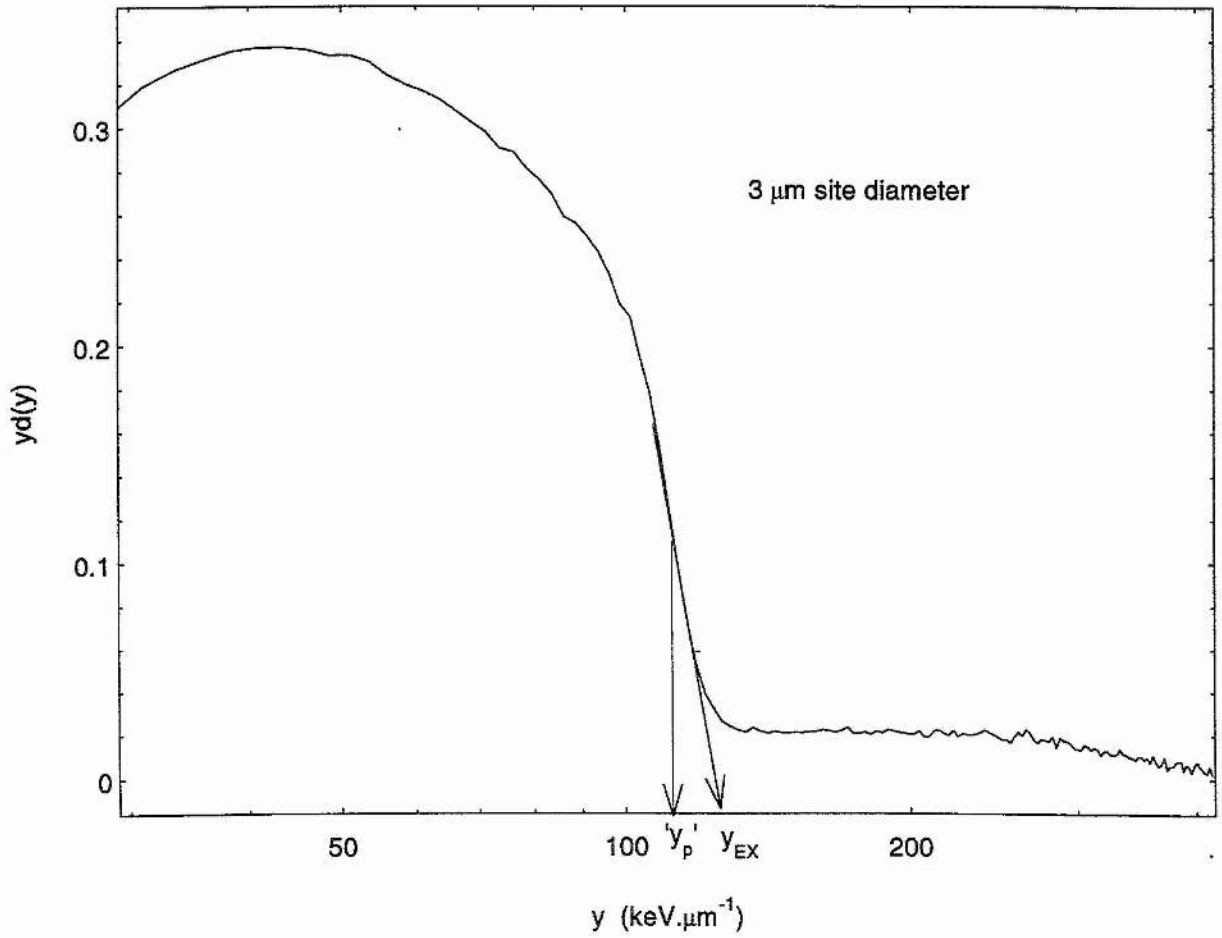

experimental data, however, is needed to estimate the accuracy of the proton-edge at other simulated diameters.

By taking y_{EX} as the proton-edge it was assumed that the resolution of the counter was not as important in affecting the slope of the final linear portion of the proton recoil peak, as the variance in the mean chord distribution. This assumption is supported by the following evidence: in the analogous inherent electron calibration method it was found from analytically calculated microdose spectra that it was the lineal energy of the 'stopper' electrons that were dominant over the resolution in forming the final linear portions of their spectra.

d (μm)	Pihet and Menzel[74] $y_{d.max}$ (keV.μm^{-1})	Waker[75] $y_{d.max}$ (keV.μm^{-1})	Present work $y_{d.max}$ (keV.μm^{-1})	Srdoc(92) $y_{d.max}$ (keV.μm^{-1}) Experimental
0.05			151.5	
0.5			149.1	
1	144.9		145.2	152 ± 5
2	134.8	136.0	136.7	133 ± 4
3			127.0	
4			118.1	114 ± 3
5	108.8		111.7	

Table 3.4

CHAPTER 4

DOSIMETRY AND MICRODOSIMETRY IN THE VICINITY OF LINACS USED FOR RADIOTHERAPY

4.0 General

The experiments performed in the present work, to determine the dosimetric and microdosimetric yields of photoneutrons in the vicinity of a LINAC, are described in this chapter. They include experiments using activation analysis to determine the spatial distribution of the neutron fluence within the treatment room; experiments to determine the optimum moderator thickness for use with the activation detectors to maximise sensitivity; and microdosimetry with a cylindrical TEPC in the maze of the treatment room for studies of the quantity and composition of the radiation field.

The results from the present project are compared with the work of others wherever possible. A critical review is made, in the last three sections of the alternative microdosimetric techniques that have been used around LINACs.

4.1.0 Thermal neutron activation analysis

The aim of the following experiment was to measure the photoneutron fluence and its spatial distribution in the beam and treatment room of the 10 MV LINAC. By knowing the fluence, the equivalent dose can be determined and the degree of hazard can be assessed.

Many isotopes are suitable for activation analysis for this application and some of these are listed in Table 2.1. Indium (^{115}In) was selected because it was readily available, it has a high thermal neutron cross-section, and with a 54 minute half-life it can be re-used in less than a day. The latter two properties ensured that sufficient activity could be induced in the limited LINAC time available. Gold, which like indium is a common choice, was rejected because it is a hundred times less sensitive, it has a longer half-life (although this can sometimes be advantageous if the calibration source is held at a distant laboratory or if there is possibility of irradiation throughout the day while patients are being irradiated), and it is expensive.

4.1.1 Methods and Materials

Samples of spectroscopically pure indium wire with a 1.6 mm diameter and mass of about 1 g were weighed precisely using a Stanton Instruments balance (model SM11) to ± 50 μg. Each sample was then placed in a closely fitting polyethylene phial which in turn was placed at the centre of a specially designed moderator (see section 4.2). For simple and economic construction, cubes of polyethylene with sides of 5 cm that provide close to the optimum thickness of moderator were made. The moderated-foils were then wholly encased in 0.3 mm thick cadmium foil which removes any sub-cadmium neutrons (neutrons with energies below 0.4 eV) and allows the intermediate and fast neutrons to pass.

The foils were irradiated at various positions within the treatment room in the plane of the patient (see Figure 4.1). For each sample the LINAC was set to deliver 10 MV bremmstrahlung at 3 $Gy.min^{-1}$ at the isocentre with a 1 m s.s.d. and a 10x10 cm^2 field for 10 minutes. Activation of the foils was also attempted with the machine operating at 6 MV.

A stopwatch was used to measure the cooling-down time, which is the time from the cessation of irradiation to the time of the first measurement of induced activity. At the cessation of irradiation the sample was taken to a sodium-iodide (NaI(Tl)) crystal for γ–ray spectroscopy where the induced activity was monitored and recorded over 90 minutes. The background count was subtracted for each sample.

4.1.2 Results and calculations

In this section the steps taken and the equations used to determine the photoneutron fluence rates and dose-rates in the treatment are given.

The activity of the indium wire was recorded against time elapsed from the termination of the irradiation (see Appendix: Figure A2 and Figure A3). The cooling of the activated wire was corrected for, by finding the activity A_o at cooling time, $t = 0$. The values of A_o were determined by extrapolation using a least squares fit.

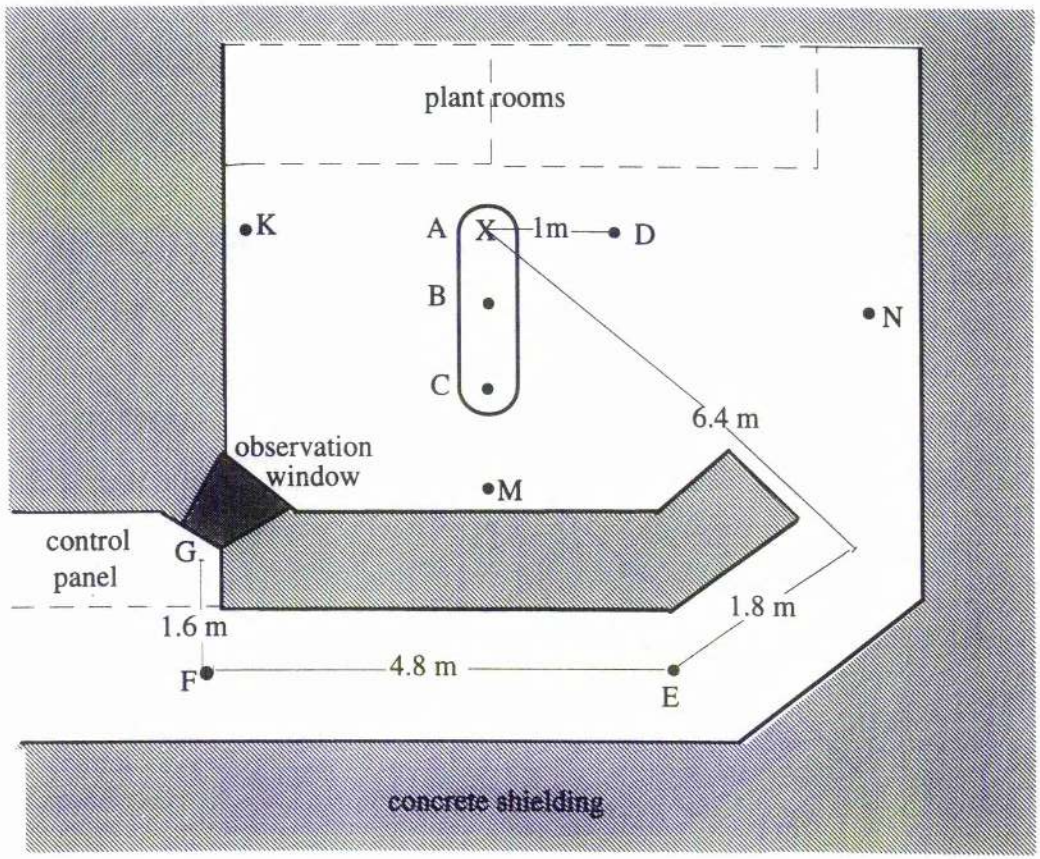

Figure 4.1. A plan of the treatment romm showing the positions of measurement and the distances from the isocentre, marked X, to the control panel.

The neutron fluence, corrected for the lack of saturation, is related to induced activity by equation (4.1) (see referrence 24):

$$\phi = \frac{A_0}{N\sigma_{act}\left\{1-\exp\left(-0.693\, t_i / T_{1/2}\right)\right\}} \qquad (4.1)$$

where N is the number of target atoms given by $\{N_A m / M\}$x 97.5% (the relative abundance of ^{115}In); σ is the activation cross-section = 1.62 x 10^{-24} cm^2; t_i is the irradiation time (s); $T_{1/2}$ is the half-life = 3204 s.

The observed fluence was corrected for the fast neutron detection efficiency by multiplying it by a calibration factor, F, which also takes into account the corrections for self-shielding and flux depression. This was found by a separate activation analysis using a ^{252}Cf source. At a position of known fluence, ϕ_{cf}, (calculated from the source's original activity and corrected for geometry) the moderated indium detector was irradiated and equation (4.1) was used to determine the observed fluence, ϕ_{ob}. F was simply ϕ_{cf} / ϕ_{ob} which was found to be 4.97.

The actual fluences, corrected for the fast neutron efficiency, measured at the various positions (at the isocentre, around the treatment room and in the exit of the maze) are shown in Table 4.1.

The dose rate, $\dot{D}$ was calculated using equation (4.2):

$$\dot{D} = K_f . \Phi \ (\mu.Gy\ s^{-1}) \qquad (4.2)$$

where K_f is the proton kerma factor in water = 1.87 x 10^{-11} $Gy.cm^{-2}$[99]. It is assumed that charged particle equilibrium was established and the photoneutron spectrum is similar to ^{252}Cf [66].

The equivalent dose-rate, H (Sv h^{-1}) has been normalised to the useful photon dose rate (usually given in units of $cGy.min^{-1}$) delivered at the isocentre under standard conditions: 10x10 cm^2 field size and a ssd of 1 m. The results have been normalised in this fashion in order to facilitate comparison with other machines operating under different conditions.

4.1.3 Discussion and conclusions

With the machine operating at 6 MV, the 6 MeV bremsstralung, which makes up a small part of the photon spectrum, has an energy only just above the photoneutron production threshold for high-Z materials, and unsurprisingly the response of the moderated activation detectors was negligible.

With the machine operating at 10 MV, there was such copious photoneutron production that even the moderated indium in the maze at about 5 m from the isocentre was activated. As expected, the highest neutron equivalent dose-rate was found at the isocentre. Using the results it can be calculated that over a complete radiotherapy treatment of 20 sessions, each of 2 Gy absorbed photon dose, for example the neutron equivalent dose would be 46.4 mSv. This is significant. However, this is 0.12% of the useful photon equivalent dose and it is less than the maximum recommended limit of 1% [100].

For comparison, data has been taken from NCRP 79 which contains an extensive review of photoneutron measurements around LINACs. The measurements were all performed using 10 MV X rays around Varian Clinac 18 machines. The data has been transformed into the equivalent dose (μSv) normalised to the useful photon equivalent dose (cGy) as shown in Table 4.2. Where only the fluence was given in NCRP 79, the proton kerma factor used earlier in this section was assumed, and where only the absorbed dose was given, a quality factor of 20 was assumed. The results from this work are in reasonably good agreement with those from the other authors considering that the yield and the spectrum of photoneutron production is characteristic to each machine type and the local treatment conditions.

The results from the present work have been published[51]. They are in good agreement with the results above. However, it should be noted that the published value at the isocentre (which was taken at position A in Table 4.1) is approximately a factor of 2 smaller than the value from the present work and also from similar results reported in the literature (see Table 4.2). This was probably a clerical error. It is believed that two different samples from different positions were accidentally

Table 4.1 Equivalent-dose rates for photoneutrons

Postion (see Figure 4.1)	**Neutron fluence** ($cm^{-2}s^{-1}$)	**Dose rate** ($\mu Gy.s^{-1}$)	**Equivalent dose rate, H_{TR}** ($Sv.h^{-1}$)	**Normalised H_{TR}** ($\mu Sv.\ cGy^{-1}$)
A	16.50	3.0	0.210	11.70
B	-	-	-	-
C	8.04	1.45	0.104	5.78
D	6.34	1.19	0.086	4.78
E	0.22	0.04	0.003	0.158
M	3.92	0.71	0.051	2.83
K	5.24	0.94	0.068	3.78
N	2.17	0.39	0.028	1.56

Table 4.2

Distance from isocentre in patient plane (cm)	**Neutron leakage per neutron cGy at isocentre (μSv/cGy)**	**Method**	**Reference**
10	12.06	A	M^{C}Ginley (47)
100	2.00	A	Deye and Young (48)
30	1.42	B	M^{C} Giney (49)
100	0.80	C	Rodgers (50)
15	12.60	C	Oliver (103)

Methods: A - moderated activation foil, B- activation foil in remmeter, C- silicon diode.

switched around and then the unexpectedly high reading found outside the isocentre (which was actually from the isocentre) was discarded as a spurious result. This highlights one of the disadvantages of activation analysis which is a relatively difficult technique that requires considerable care particularly in labelling the samples and organising the data when several samples are irradiated simultaneously.

The dose at the operating personnel's consul can be estimated by using Kersey's method[101] which is normally used for calculating the equivalent dose at the entrance of the maze. This is an empirical method which errs on the conservative side by overestimating (in comparison with measurements) the equivalent dose by approximately 20% for mazes with a single bend and by 2.5-5.4 times for mazes with a double bend[102], such as the one at Ninewell's hospital. The equivalent dose-rate, H is given by:

$$H = (H_0)(d_o/d_1)^2\, 10^{(-d_2/5)} = 3.4 \times 10^{-3}\ \mu Sv/cGy \qquad (4.3)$$

where Ho the neutron dose equivalent at a distance do from the source; d_1 is the distance to the position on the centre line of the maze from which the source is just visible; d_2 is the distance (from the last point) straight down the centre of the maze to the point of measurement. In this case Ho= 5.78 μGy/cGy; d_o=1 m (position D in Figure 4.1); d_1 = 6.4 m; and d_2 = 8.1 m. Therefore,

$$H = 3.4 \times 10^{-3}\ \mu Sv/cGy$$

This means that the annual neutron equivalent dose to the operator for a high annual turn-over of 800 patients[116] each receiving a 40 Gy dose of 10 MV photons in an entire course of treatment (this would be unlikely because the CH-20 is a multi-mode machine) would be 11.2 mSv. This is a significant, but acceptable dose (20 mSv is the annual maximum dose for a classified worker). Standing away from the console at point F in the maze entrance, a very persistent visitor could receive about 21.6 mSv. This however, would not be permitted as the current status of the aforementioned areas is 'restricted access' (access permitted to certified personnel and patients only).

Further assessment of the neutron dose levels is recommended particularly in the treatment room where the patient, of course, receives the highest dose. Even the operator could accumulate a significant neutron equivalent dose that according to the principle of ALARA should be monitored through the use of TLDs, for example. A better knowledge of the photoneutron spectrum in particular is required if significant improvements to the conventional dosimetric techniques, such as activation analysis. are to be made.

4.2.0 Optimisation of the moderator thickness

For the neutron activation of indium, fast neutrons must be thermalised, or slowed-down to the resonance of indium, to approximately 1.4 eV (see Figure 4.2). A hydrogenous moderator that slows the neutrons by elastic scattering, such as polyethylene is needed.

The recommended moderator[21] for neutron activation experiments around high energy electron accelerators is a cylinder of 15.2 cm (height) by 15.2 cm (diameter). This design has been used for many commercial remmeters (e.g the NM-1 Anderson-Braun type BF_3 tube) and sievert-meters for radiation protection usage because of the 'flat' response it produces, i.e. it provides an energy independent thermal neutron fluence to fast neutrons typically from 0.025 MeV to 10 MeV. However, the use of such a large moderator has several disadvantages including: poor sensitivity (which means long counting times are required for good statistics), poor spatial resolution, and the weight (at over 11 kg it is cumbersome). The aim of the present experiment was to establish the optimum moderator thickness for indium foils for photoneutron activation analysis around a 10 MV LINAC. The technique partly relies on the assumption that the response of the moderated activation foils to the fast fission spectrum of ^{252}Cf is similar to the photoneutron spectrum [21]. In the following experiment it was found that a 2.5 cm thickness of polyethylene moderator is sufficient to provide near maximum sensitivity in two different proportional counters.

Figure 4.2. In -115 total cross-section taken from (27)

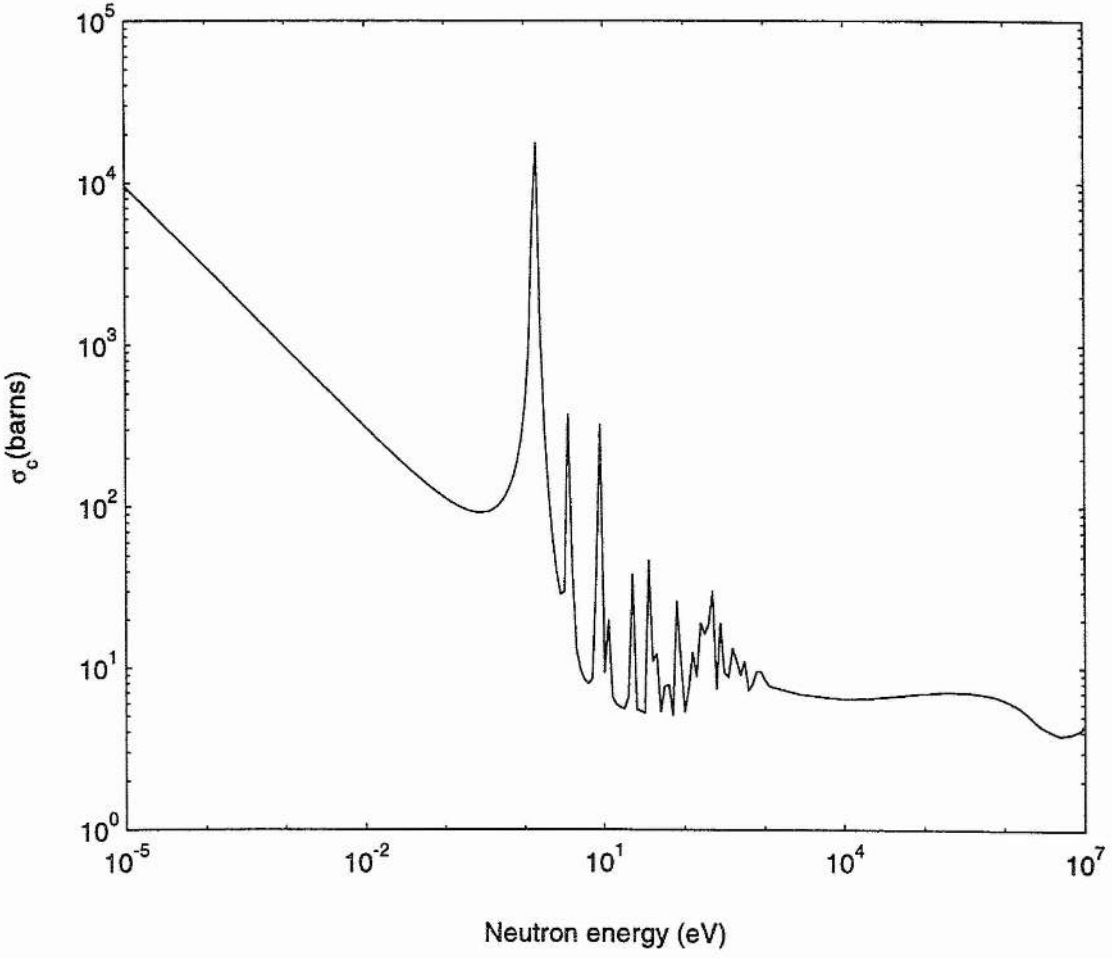

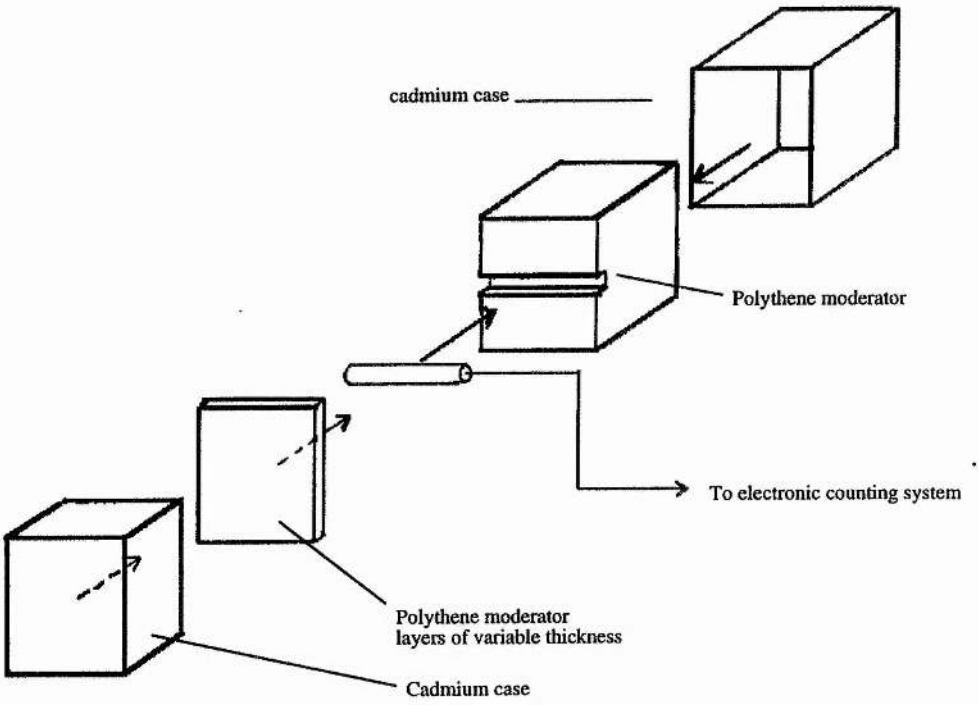

Figure 4.3. The construction of the equipment for the optimum moderator thickness experiment (neutrons were incident in broad geomettry in the same direction as the dashed lines with arrows).

The net efficiency is almost two fold greater than the 15 cm diameter moderator used hitherto.

4.2.1 Optimisation of the moderator thickness for a californium source

Rectangular polythene $(CH2)_n$ slabs of thickness ranging from 10 mm to 50 mm, and of area 30.5x30.5 cm^2 were precisely manufactured. Also a large polythene block of the same area, but of thickness 25 cm, effectively infinite to scattered neutrons, was made to provide a mount for the detector and to provide neutron shielding for its rear. A 1 mm thick cadmium case for the removal of incident thermal neutrons, enclosed the entire assembly (see Figure 4.3).

Two different proportional counters were used:

(1) a BF_3 proportional counter (LND type 20276) filled to a gas pressure of 700 torr with an ideal operating voltage of 1900 V.

(2) A ^3He proportional counter (LND type 2531) filled to a gas pressure of 4560 torr with an ideal operating voltage of 2000 V.

Both counters have an excellent response to thermal neutrons, with ^3He having greater sensitivity, but with its lower Q value (764 keV compared with 2.33 MeV for BF_3), discrimination through amplitude alone against gamma fields is worse. The gamma dose rate at 1.68 m from the ^{252}Cf source was approximately 10 $\mu Gy.h^{-1}$ measured with a Mini-Monitor GM meter (type 5.10). The gamma component of the field gave a negligible response in both detectors (tested by monitoring the response with and without lead shielding).

The ^{252}Cf source was housed in a perspex holder at the centre of heavy shielding which consisted of large blocks of polyethylene, lead-impregnated polyethylene for shielding of the γ component, and boron impregnated polyethylene. These formed a cube of sides of approximately 1 m. Access to the source was via a rectangular collimator, 15 cm wide, 10 cm high and 50 cm long.

The moderated detector was placed at 1.68 m from the source and irradiated for 300 s. For each experimental run a different thickness of moderator was used for

the front of the detector. The results shown in Figures 4.4 and 4.5 show the count rate versus the moderator thickness for the two proportional counters used.

The graphs clearly show that the maximum sensitivity occurs for a 30 mm thickness of polythene moderator for the BF_3 counter, and for a 20 mm thickness for the ^3He counter. The mean value of optimum moderator thickness for the two detectors is 2.5 ± 0.5 cm. The peaks are broad and variations in thicknesses of as much as ± 1.0 cm from the mean optimum thickness, result in only small reductions in sensitivity (18% and 9% for the BF_3 and ^3He counters respectively). The results also show that the response of the detectors steadily increases as moderator is added until the thickness at which the production of thermal neutrons is a maximum. Beyond this point the thermal neutrons are absorbed at a greater rate than they are produced and the response of the detector falls. With a moderator thickness of 70 mm, corresponding to the previously mentioned recommended dimensions, the sensitivity of the detector is reduced by over 50% for both counters.

In the above experiment the fast neutrons were moderated to thermal energies and in the activation of indium they only need to be slowed to 1.4 eV requiring a slightly smaller moderator thickness. However, the correction amounts to only 2%[22].

4.2.2 Discussion and conclusion

The depth in tissue-equivalent liquid of the thermal neutron flux peak has been measured by Lawson and Watt[104] (see Figure 4.6). The depth in tissue for which the thermal neutron flux is a maximum, X_{max}, is 4.8 ± 0.1 cm for broad beam incidence of monoenergetic 2.5 MeV neutrons. There is good agreement with their work and the calculated values of Block and Schon[105] who describe how X_{max} can be derived from the diffusion length, L_D, and the relaxation length, L_R, through the equation:

$$X_{max} = \frac{L_R . L_D \ln(L_R/L_D)}{L_R - L_D} \qquad (4.4)$$

Figure 4.4. The sensitivity of a BF_3 proportional counter moderated with different thicknesses of polethylene

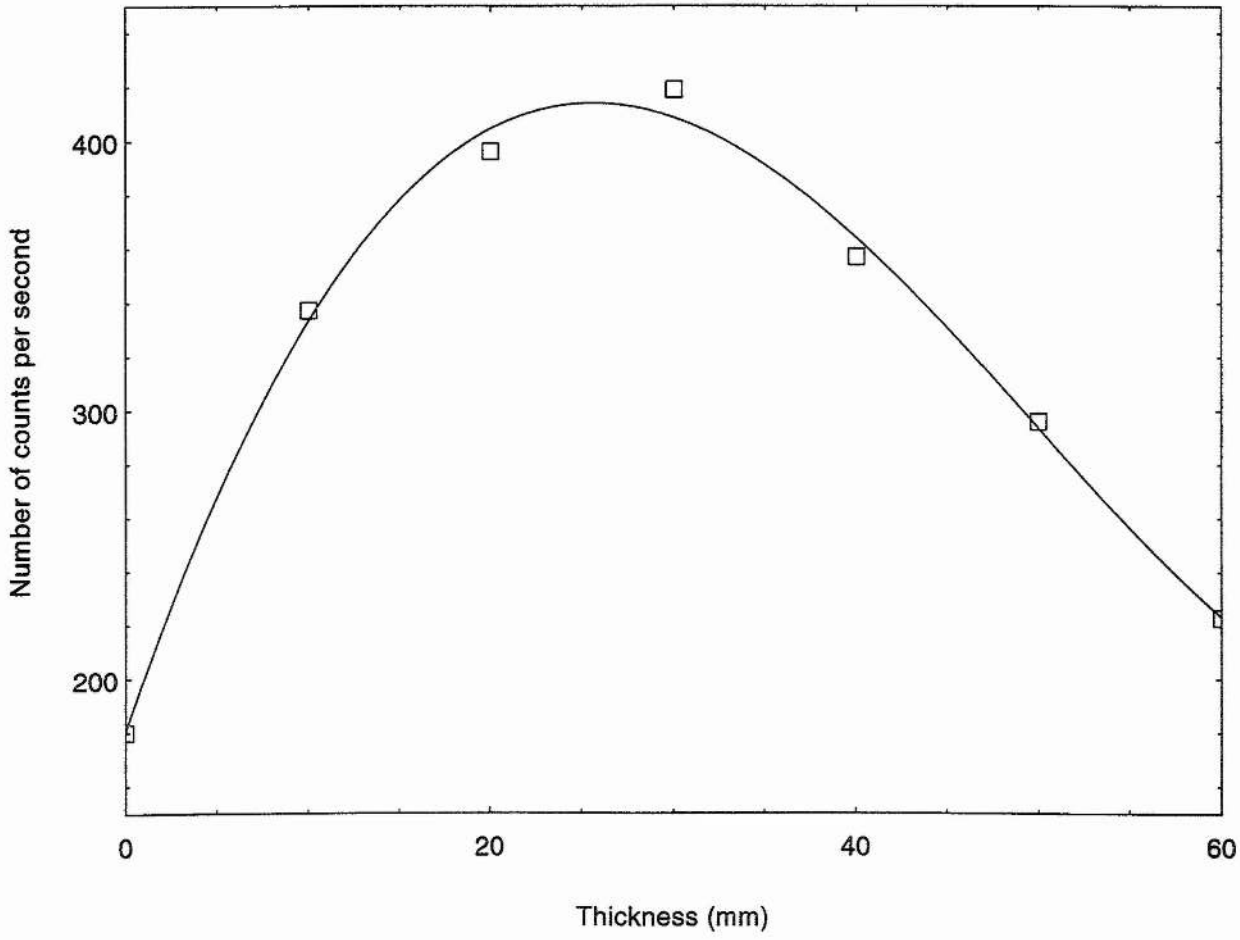

Figure 4.5. Sensitivity of a ^{3}He proportional counter moderated with different thicknesses of polyethylene

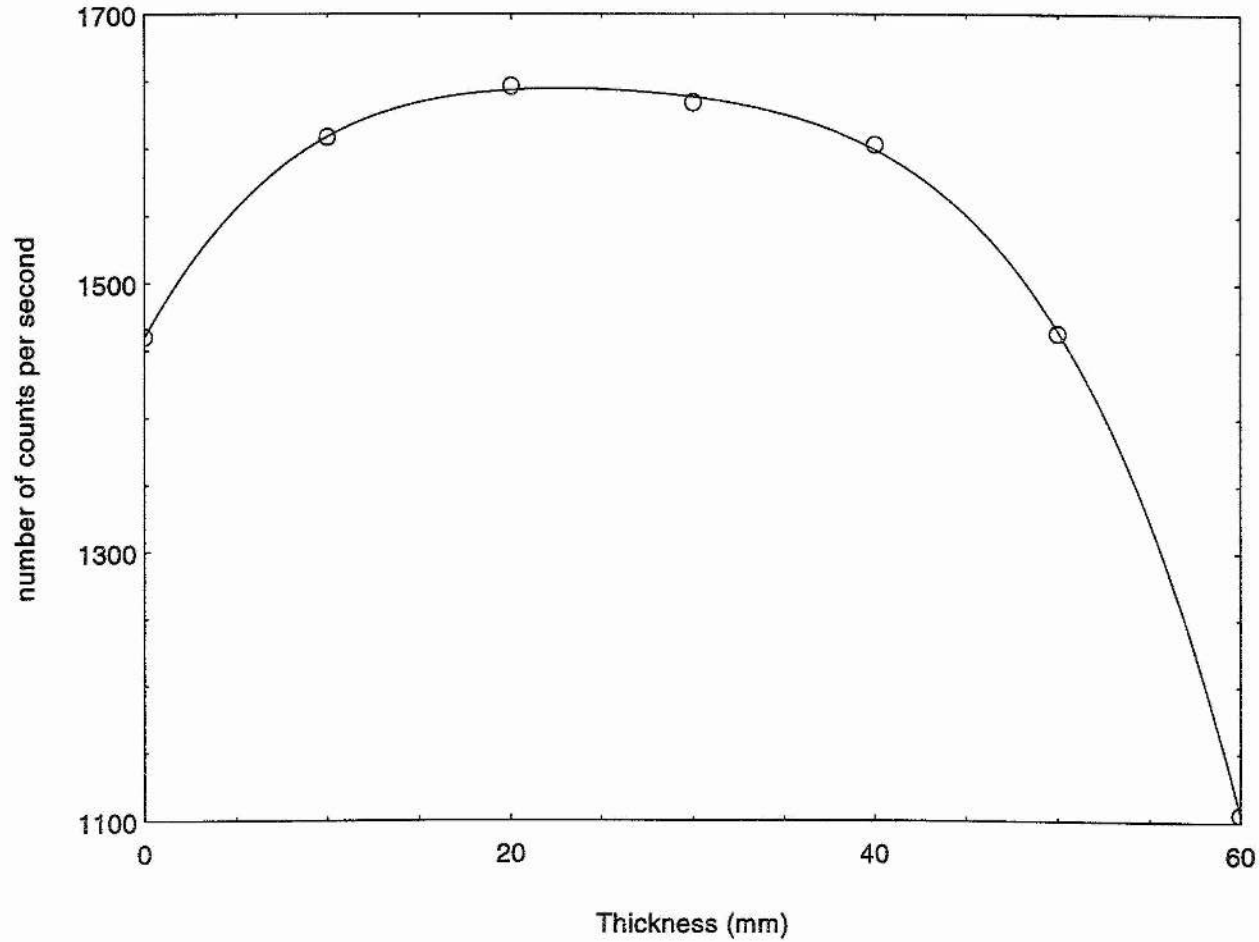

Figure 4.6. Thermal neutron flux distribution in tissue

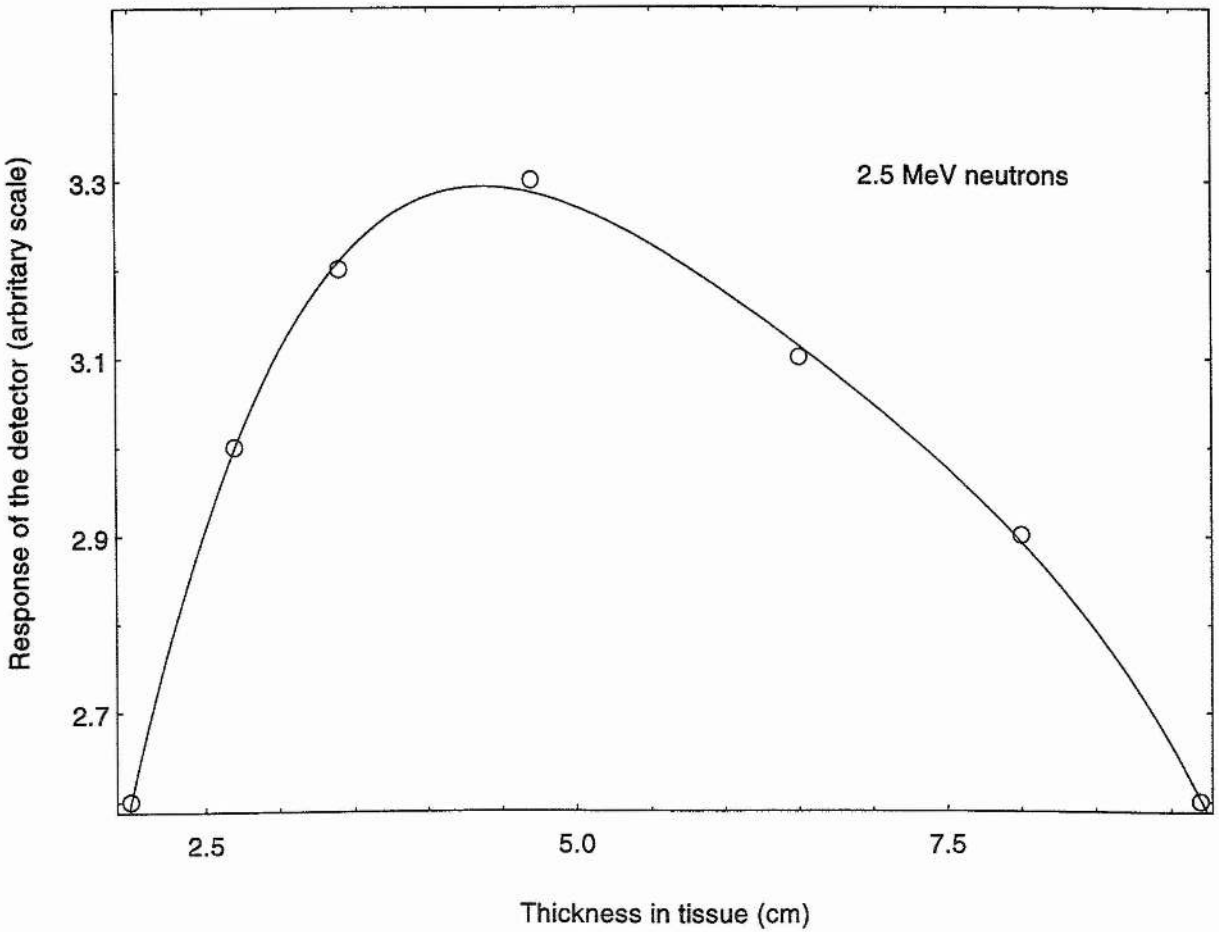

Using the experimentally measured values of 2.68 cm for the diffusion length and 9.2 cm for the relaxation length for 2.5 MeV monoenergetic neutrons, X_{max} = 4.7 cm, which is in excellent agreement with Lawson's and Watt's value.

These previous results have significance to the present work by confirming that the optimum moderator thickness (i.e. 2.5 cm) is such, that the counters used were indeed positioned close to the point of maximum thermal flux. According to the results of Lawson and Watt, a 2.5 cm thickness of tissue-equivalent liquid moderator will give a thermal neutron flux that is 11% less than X_{max}. However, it should be noted that the mean energy of the fission neutrons from ^{252}Cf is initially 2.15 MeV, and then reduced by scattering in the collimator, although unmeasured, is considerably less than the 2.5 MeV monoenergetic neutrons used by Lawson and Watt, and therefore a thickness of less than 4.8 cm would be expected for X_{max}.

Experiments with lower energy neutrons have been carried out by Watt [106] when attempting to optimise the sensitivity of a delayed neutron detector for use at the electrostatic precipitators of the cooling tower of a nuclear power station. Using a similar experimental setup to the present work, that included polyethylene moderator and a BF_3 proportional counter, the mean energies of the neutrons was up to and including 0.6 MeV. The optimum thickness of moderator was found to be 3 cm.

Although the photoneutron spectrum produced by a 10 MV LINAC has never been precisely measured it can be considered, from Monte Carlo simulations, to comprise a direct component from interactions between bremmstrahlung and the tungsten target with a mean energy of 0.6 MeV, and a scattered component throughout the room which is of lower energy. The combination of the two components is a complex spectrum with a mean neutron energy of approximately 0.3 MeV only (see NCRP for the 'cookbook' method)[66]. Thus for this application there are several advantages to be gained by using a moderator thickness of 2.5 cm. These are:

1. Higher sensitivity to these low energy photoneutrons (This means that shorter counting times , with better statistical precision are achieved.).

2. Improved spatial resolution.

3. Easy to handle, light-weight compact detectors.

4.3. Experimental microdosimetry results using the cylindrical TEPC

Conventional TEPCs are unsuitable for measurements in the treatment room of a LINAC because of the intense r.f. fields and the ultra-intense γ fields. In the present work, although valuable experience was gained, all attempts of acquiring sensible results within the treatment room of the 10 MV LINAC at Ninewells Hospital, Dundee, were unsuccessful.

In an attempt to overcome the problem of the intense r.f. fields a Faraday cage was constructed and utilised to enclose the counter, the short coaxial cable to the pre-amplifier, and the pre-amplifier itself. Furthermore, the electronic counting system was kept outside the treatment room by using 25 m long coaxial cables. However, the electronic screening was inadequate and the pulsed electromagnetic interference (EI) more than doubled the normal electronic noise. This problem, although serious, perhaps would have been solved by the use of tri-axial cable instead of coaxial cables, but a more serious problem was encountered. The intense pile-up that resulted from multi-events due to the geometrical cross-section of the counter being far too great for the ultra-high fluence rates in the mixed photon-neutron field, prevented the pulse height analysis of single events. Even by taking advantage of the inverse square law and moving the TEPC 5 m away from the treatment beam, severe pile-up still occurred.

Some success was finally achieved by further increasing the distance from the treatment beam, and taking advantage of the massive concrete shielding that separates the treatment room from the maze. At the exit of the maze (i.e. at the treatment room end) a microdose spectrum was obtained (see Figure 4.7). The simulated diameter size was 2.7 μm and calibration was via proton-edge calibration at 130 keV.μm^{-1}. The frequency and dose mean lineal energies of the proton recoils was determined to be 4.0 keV.μm^{-1} and 27.7 keV.μm^{-1} respectfully. The major features of this spectrum

Figue 4.7. Dose distribution in lineal energy in the maze of the treatment room

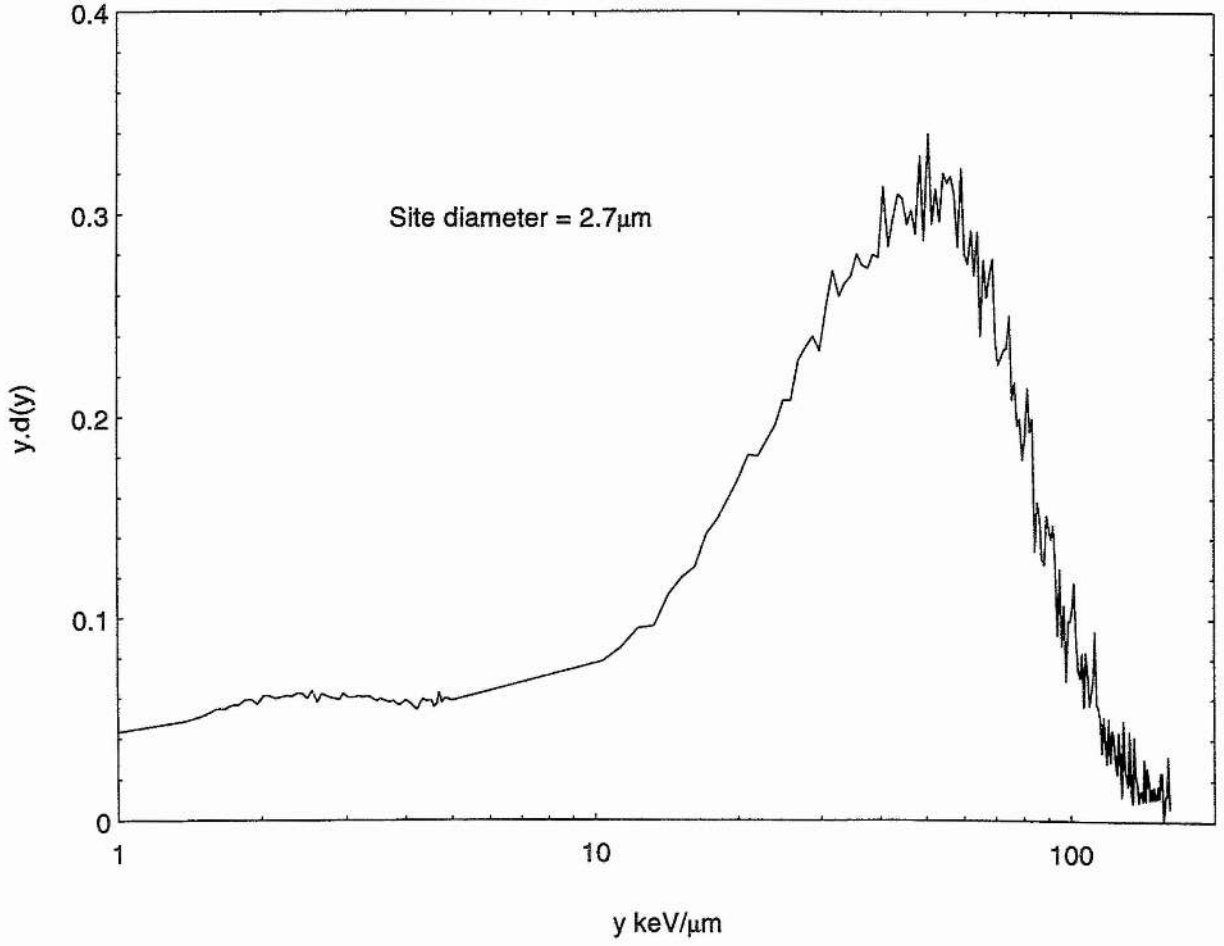

include a proton recoil peak at about 60 keV.μm^{-1} and a sharp proton-edge (the calibration point). There is little evidence of heavy ion recoils. Only the high y portion of the photon event spectrum was obtained, as the portion below about 0.9 keV.μm^{-1} was submerged in the heightened electronic noise region (for a simulated diameter of 3μm the minimum threshold of y events obtained in the laboratory was 0.14 keV.μm^{-1}).

The dose rate measured by the TEPC was 0.26 $\mu Gy.s^{-1}$ which can be compared to a neutron dose rate measured by indium wire activation analysis of 0.04 $\mu G.s^{-1}$. The two results are in reasonable agreement considering the strong photon response of the TEPC and the negligible photon response of the activation detector. However, the magnitude and accuracy of the measurements was considered less important at this stage than the discovery of the limitations and capabilities of the TEPC for measurements around the LINAC.

It was concluded that the TEPC is suitable for measurements in some parts of the maze leading to the treatment room. However, the value of spectral measurements for radiotherapy research, or for protection purposes, in this region of the treatment room, neither close to the machine operator nor the patient, is minimal. For use in the treatment room itself a radical re-design of the counter would be necessary.

4.4 Measurements by Kliauga and Amols using the Ultra-Miniature Counter

A radical re-design of the TEPC was achieved by Kliauga and Amols[6] with the ultra-miniature counter (UMC) which they originally developed when aiming to improve the simulation, by TEPCs, of site sizes of the order of tens of nanometres (this application, however, is beyond the scope of this thesis). Taking advantage of the counter's miniature proportions, they successfully applied the UMC to obtain microdosimetric spectra from the vicinity of a LINAC treatment beam, with the LINAC operating under normal clinical conditions. This is a remarkable

achievement considering the difficult problems that had to be overcome and it is the first time that such measurements have been achieved!

A measurement position of 1.4 m from the isocentre was chosen, at which point the photon dose rate, and fluence rate had fallen to 0.1% of the treatment dose rate which was 3 $Gy.min^{-1}$ delivered at 120 $pulses.s^{-1}$. The miniature cylindrical sensitive volume of equal height and diameter (0.5 mm) means the cross-sectional area of the UMC is only 0.25 mm^2, which was small enough to ensure that a single event occurred for each LINAC pulse. A Lucite plastic phantom was used to simulate the patient.

The electromagnetic interference problem, although not entirely overcome, was managed in the following manner. The precaution of leaving most of the counting electronics outside the treatment room was taken, and the connecting leads were passed through the maze wall to the pre-amplifier and high-voltage supply, inside the treatment room. The counter was placed in a grounded aluminium shield which was found to reduce the r.f. noise. Further reduction was achieved through the trial and error positioning of the high voltage leads to a position of minimum r.f. pick-up. However, some r.f. noise occurring regularly and with constant pulse height, remained and onto this noise the true counter pulses were superimposed. By simply subtracting the noise signal from each one of the signal pulses and adjusting the energy calibration 'accordingly' (the calibration method used was unreported), Kliauga and Amols were able to effectively minimise spectral distortions from r.f. noise.

Conventional signal processing and standard microdosimetric algorithms were used to obtain the dose distribution in lineal energy transfer for a simulated site diameter of about 0.9 μm. This is shown in Figure 4.8.

The photon component has been distinguished from the photoneutron component in the figure. The photoneutron component is characterised by a photon recoil peak at about 100 $keV.\mu m^{-1}$ and a distinct proton-edge at about 170 $keV.\mu m^{-1}$. However, the values for this simulated diameter should be between 80-90 $keV.\mu m^{-1}$ and 150 $keV.\mu m^{-1}$ respectfully (see proton-edge calibration section). The apparent

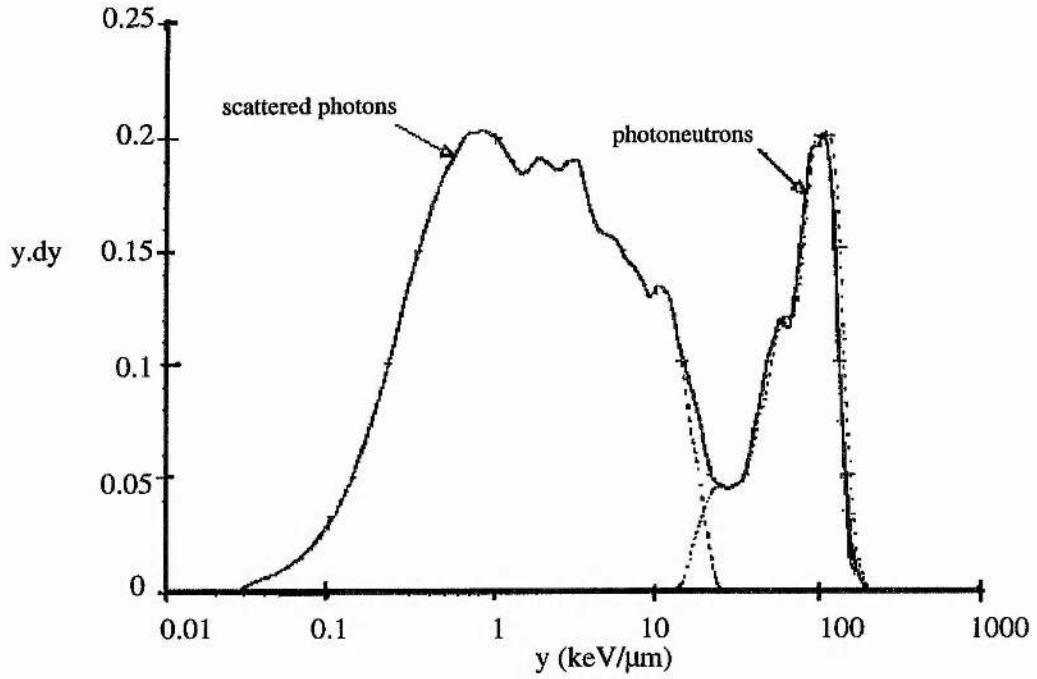

Figure 4.8. The microdose spectrum at 4 m from the isocentre of a 20 MV LINAC as measured by Kliagua and Amols[6] using their UMC tissue equivalent proportional counter. The photoneutrons have been clearly distinguished from the photon component. The spectrum is consistent with an average neutron energy of approximately 1 MeV or less.

lack of heavy ion recoils above the proton-edge is consistent with a photoneutron mean energy of about 1 MeV or below, and this is consistent with what is expected from a LINAC operating at 20 MV. The frequency and dose mean lineal energies of the proton recoils was determined to be 62.2 keV.μm^{-1} and 83.8 keV.μm^{-1} respectively, and these will be overestimates by a factor of approximately 1.14 due to the high calibration factor used.

Kliauga and Amols estimated that the photon component would have a Compton energy of 500 keV with the UMC at 90° to the beam, and furthermore they assumed that this would create a spectrum similar to that from a ^{137}Cs source. From this they expected the electron-edge to appear at 25 keV.μm^{-1}, however for a simulated diameter of 0.9 μm the electron edge is nearer to 14 keV.μm^{-1} (see section 3.7). Their over-estimation of the lineal energy of the photon component is probably due to the overlap of low lineal energy proton recoils in the 1-10 keV. μm^{-1} region.

The dose rate measure using the UMC was consistent with that measured by others (equating to an equivalent dose of 60 mSv for a 40 Gy course of treatment - see section 2.3.1.1). Kliauga and Amols also measured the photoneutron dose rate with two bubble neutrometers, which are types of bubble detectors, and found a dose rate that was approximately half of that measured with the UMC. Despite this, they considered the dose measurements to be in good agreement given the uncertainties with the use of the UMC.

Kliauga and Amols, from the microdosimetric spectrum, estimated a quality factor of 23 using the Theory of Dual Radiation Action[107] and remarked that neutrons with an average energy of about 1 MeV have a biological effectiveness near to the maximum. This justifies the use of a quality factor of 20 from ICRP 60 for application to photoneutrons from high energy LINACs.

Although the use of the UMC for microdosimetry in the treatment room of a LINAC is an on-line technique that allows for the usual clinical operation of the LINAC, the measurements for the data to construct Figure 4.8 took approximately 8 hours of LINAC time to perform. This, and the technical difficulties involved in

constructing a miniature counter mean that the UMC, is at present, strictly a research tool.

4.5 Microdosimetry using TEPC's around 'de-tuned' LINACs

Several researchers[108,109,110] have opted to reduce the dose rate of the LINAC or electron accelerator by a factor of around 10^6 to permit the use of TEPCs for microdosimetry at the isocentre.

Amols and Zellmer have provided details to explain how this reduction in dose rate can be achieved experimentally[108]. They explored the following four methods: reducing the filament current in the electron gun; varying the voltage on the gun grid; 'de-tuning' the phase difference between the electron gun and the klystron; and reducing the injection potential between the electron gun and the waveguide. They found that a combination of the last two techniques could be used to bring about the required reduction in dose rate to approximately 1-10 $\mu Gy.min^{-1}$. To ensure that these de-tuning methods had not altered the energy characteristics of the beam, they measured the isodose profiles in a phantom at various depths, and found that their experimental results were in good agreement with their calculations. They concluded that these dose reduction methods, although altering the beam slightly, would not significantly effect the energy dependent microdosimetric characteristics of the beam.

Using a Rossi-type TEPC filled with propane based TE gas and simulating a site size of 2 μm, they measured the photon contribution of the dose distributions in lineal energy of 10 MV and 15 MV bremsstrahlung beams at their isocentres. As expected the ^{60}Co distribution was the least 'hard' (i.e. a highly penetrating beam) , but surprisingly the 15 MV beam was the next hardest, with the 10 MV being the hardest. The explanation given for this was that the mean energy of the compton recoil electrons of the 10 MV beam was approximately 1.5 MeV and at this energy electrons have the lowest stopping powers.[111].

Table 4.3

Beam	Simulated diameter (μm)	$\overline{y_d}$ (keV.μm^{-1})	$\overline{y_f}$ (keV.μm^{-1})	Reference
^{60}Co	0.95	2.34	-	Lindborg (110)
8 MV *	0.9	1.97	-	Honré *et al.* (115)
8 MV*	1.95	1.47	-	Honré *et al.* (115)
10 MV*	2	1.40	-	Kliauga *et al.* (114)
10 MV	2	1.53	0.34	Amols and Zellmer (108)
10 MV	2	1.08	0.20	Tilikidis *et al.* (109)
15 MV	2	1.79	0.37	Amols and Zellmer (108)
16 MV*	0.9	1.84	-	Honré *et al.* (115)
16 MV*	1.95	1.41	-	Honré *et al.* (115)
42 MV	0.95	2.08	-	Lindborg (110)
50 MV Be-W target	2	2.76	0.30	Tilikidis *et al.* (109)
50 MV W-Cu target	2	2.82	0.24	Tilikidis *et al.* (109)

* Variance-covariance technique

The results are compared with those of Tilikidis *et al.*[109] and Lindborg[110] for 0.95 μm and 2 μm simulated diameters in Table 4.3. The result of Tilikidis *et al.* for 10 MV are in reasonable agreement with the result of Amols and Zellmer and shows that this energy beam is harder than the 50 MV beam. Tilikidis also obtained the photoneutron component of the microdose spectrum. It is interesting that they used proton edge calibration, nominating the mid-way of the final linear portion of the proton recoil peak as 150 keV.μm^{-1} (in section 3.7 it is explained why the intercept onto the abscissa should be taken and why the proton edge has a value of 136 keV.μm^{-1} for a 2 μm simulated diameter), causing an overestimate in the y values a factor of 32% (their intercept occurs at around 179 keV.μm^{-1}).

The other main conclusion drawn by the various authors include: there is not a significant variation (outside the build-up region) of the microdosimetric parameters, $\bar{y}_f$ and $\bar{y}_d$ with depth in a phantom; and these parameters of the beam are dependent on the energy of the beam, varying by as much as 30%.

The method of 'de-tuning' the radiotherapy machine is useful for obtaining microdosimetric results, so long as complex precautions are taken to ensure that the energy characteristics and spatial distribution of the beam are unchanged. This may be a suitable radiobiological research technique, but it is not suitable for routine clinical monitoring and assessment. The variance-covariance method., may be a better alternative.

4.6 Microdosimetric measurements of radiotherapy beams using the variance-covariance technique

In high dose rate fields, in nanometer simulated volumes, and in pulsed fields where single events cannot be resolved, the variance technique.[112], an alternative method of microdosimetric measurement, has found its niche. Instead of pulse-height measurements usual in conventional TEPC operation, repeat measurement of the charge released in an ionisation chamber, or a TEPC, over a specified time interval are performed. The relative variance in these groups of measurements as random

distributions is then determined. The relative variance, which can be thought of as a dimensionless index of the width of a distribution (the distribution used in the following is f(z, D) which is the distribution of specific energy with absorbed dose), is defined by:

$$V_r = \frac{\sigma^2}{\bar{z}^2} \tag{4.5}$$

where z is the specific energy and σ is the standard deviation.

Kellerer and Rossi.[107] have shown that the dose average specific energy, $\bar{z}_d$, per event is related to the absorbed dose, D, by:

$$\bar{z}_d = V_r . D \tag{4.6}$$

also,

$$\bar{z}_d = \frac{\overline{z^2}}{\bar{z}} - \bar{z} \tag{4.7}$$

In practice , $\overline{z^2}$ and $\bar{z}$ are found experimentally from a number, N, of individual measurements, i (typically of the order of 10^3). They are given by:

$$\overline{z^2} = \frac{1}{N}\sum_i^N z_i^2 \quad \text{and} \quad \bar{z} = \frac{1}{N}\sum_i^N z_i$$

For the accurate measurement of the desired variance, in this case the variance of the specific energy, spurious signals and unwanted variances must be minimised as they are a source of error. Fluctuations in the intensity of the radiation field, for example can make the variance technique impractical. Recognising that this source of error can be eliminated by dividing each value of z_i by a correction factor proportional to the intensity of the radiation during the measurement interval, Kellerer and Rossi[113] invented the variance-covariance technique, a special case of the variance technique. They realised that the correction factor could come from a second independent detector, denoted B, used simultaneously and close up to the first detector, denoted A.

The dose mean specific energy per event in detector A is

$$\bar{z}_d = (V_A - C_{AB})\bar{z}_A \tag{4.8}$$

where $$V_A = \frac{\overline{z_A^2}}{\overline{z_B^2}} - 1 \qquad (4.9)$$

and $$C_{AB} = \frac{\overline{z_A z_B}}{\overline{z_A}\,\overline{z_B}} - 1 \qquad (4.10)$$

If the two detectors are identical and they are placed close together and symmetrically in the radiation field then the average of their dose mean specific energies can be taken in order to reduce errors further.

The dose mean lineal energy, y, which is analogous and directly proportional to the specific energy, z, can be also be determined.

Kliauga *et al.*[114] were the first to perform microdosimetry using the variance-covariance technique in the vicinity of a LINAC. Applying de-tuning methods (see section 4.2) they reduced the dose rate such that only 40 - 500 events per LINAC pulse occurred within their two detectors, TEPCs (1-inch). Limiting the number of events was necessary to avoid causing saturation in the preamplifiers. The problem of r.f. interference was minimised by using r.f. filters in the preamplifier and high voltage supplies; careful grounding; and keeping the data acquisition electronics outside the treatment room. The results they obtained in electron beams and in X ray beams were in good agreement with others (see Table 4.3 for their measurement of the dose mean lineal energy in a 10 MV X ray beam). The authors concluded that the variance-covariance technique holds several advantages over conventional single-event microdosimetry around LINACs. These include: a faster acquisition time (15 s compared with several hours); a greater signal-to-noise ratio that reduces the problem associated with r.f.; and measurements in higher dose rate fields are possible.

Honré *et al.*[115] used two identical spherical TEPCs to measure the dose mean lineal energy from a medical accelerator for 8 and 16 MV X rays. To reduce the dose rate and to avoid problems with electromagnetic interference they took their measurements at 8 m from the isocentre and directed the beam through a hole in the wall to their detectors in an adjoining room. Their results with build-up caps are

shown in Table 4.3 and although comparison is difficult, they are in broad agreement with the other results.

The variance-covariance technique is a more complex method than conventional microdosimetry, requiring two detectors with at least double the amount of electronic modules. Furthermore, apart from the microdosimetric mean values, no other spectral information is available, which is a disadvantage particularly in a mixed field. Thus, the approach in the present work has been to develop a miniature detector for a pulse height analysis system.

CHAPTER 5

THE PRELIMINARY DEVELOPMENT OF A NEW CONDENSED PHASE MICRODOSIMETER

5.0 Introduction

A novel approach to overcome the problems associated with conventional microdosimetry in the vicinity of a LINAC was adopted. It was decided that the use of a miniature scintillator would overcome the problem of the ultra-high fluence rates. Furthermore to avoid the strong r.f. fields and any gamma response of the photo-detector, an optical fibre would transport the scintillation light to a photomultiplier tube outside the treatment room (see Figure 5.1).

The various aspects for the design of the detector are discussed including the choice of materials; estimates of the light losses and the threshold signal in the detector; and estimates utilising calculated microdosimetric spectra, of the size of the scintillator required. Some preliminary results are reported that highlight the fundamental limitations of the detection system, and confirm the results of others[117]. These limitations are explained and future work to overcome them is outlined.

Although there are no reports of microdosimetry being attempted using miniature scintillators, scintillator-optical fibre devices have been used previously, but mainly for the purposes of dosimetry.

5.1 Scintillator-optical fibre devices for radiotherapy and radiography

Optical fibres with scintillators have been used for radiotherapy where absorbed dose measurements were performed in a (γ,n) mixed field[118] and for radiography as radiation sensor[119]. Similarly, the use of scintillator fibres for general dosimetry has been reported[120], but in all cases no spectral information was obtained. Also, a microdosimeter probe that consisted of a thermoluminesence dosimeter (TLD) mounted upon the tip of a hypodermic and an optical fibre reader[121] was developed to obtain *in vivo, in situ* measurements. More recently Beddar[122,131]

developed a miniature, water-equivalent, plastic scintillator dosimeter in which an optical fibre bundle was coupled to a remote photomultiplier tube. The specific applications to which its use would be appropriate were identified as follows: real-time dose mapping of radiotherapy beams in water, *in vivo* dosimetry, and small-field dosimetry.

5.2.0 The development of the new microdosimeter

Pile-up in the pulse height measurement in the high intensity field can be avoided if the probability of a radiation track being recorded per LINAC pulse is less than unity. Thus miniaturisation was considered essential if single event spectra were to be counted in the vicinity of a LINAC. The diameter of a spherical scintillator were estimated in the following manner.

The frequency of events per unit absorbed dose[66] is, Φ^*, which is given by:

$$\Phi^* = n / D \qquad (5.1)$$

where n is the mean number of events for an absorbed dose, D (Gy), and:

$$n = \frac{D}{k \times \overline{y_f}} \qquad (5.2)$$

where $k = 0.204 / d^2$ for a spherical volume of diameter, d, and $\overline{y_f} = 0.3$ keV.μm^{-1} for high energy photons. Then d is given in micron by:

$$d = \sqrt{\frac{0.204 \times n \times \overline{y_f}}{D}} \qquad (5.3)$$

For a dose rate of 3 Gy.min^{-1} at the isocentre the pulse rate is 114 s^{-1} (for 10 MV bremmstrahlung) then for a single counter pulse for each LINAC pulse the diameter of the counter should be less than 11.8 μm (incidentally, this is typical of the diameter of a mammalian cell). For measurements at 1 m away from the isocentre the dose rate reduces by a factor of about 1000 and the diameter of the scintillator for single event spectra could be increased to 379 μm, which is similar to the diameter of the UMC (see section 4.2) . Naturally the energy deposited in such tiny volumes will be small,

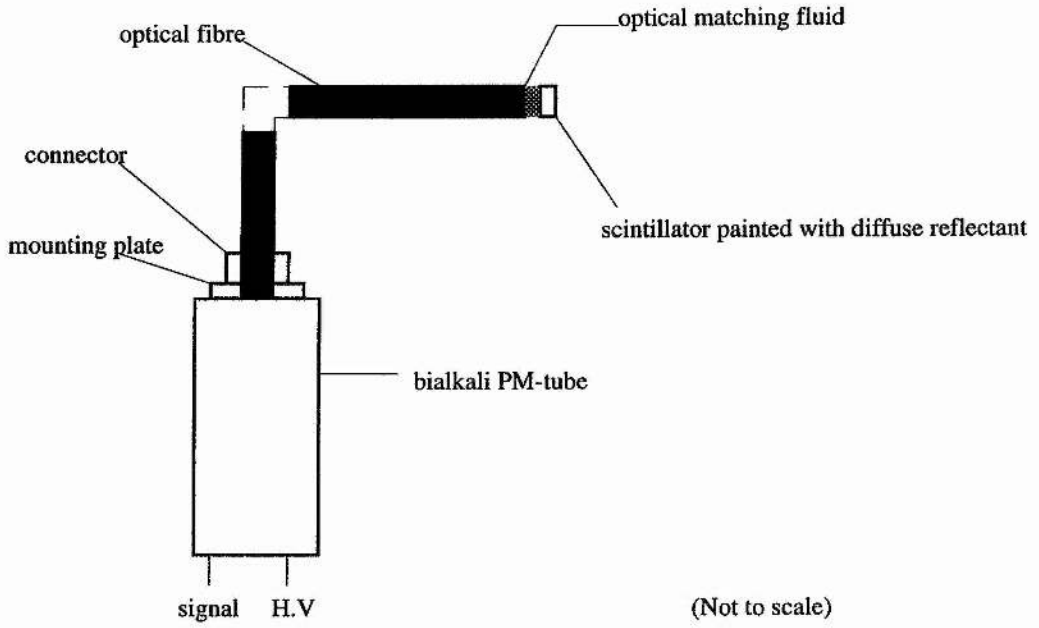

Figure 5.1. The basic construction of the detection system. The whole arrangement was made light-tight to exclude ambient lighting. The external width diameter of the sleaved fibre was under 1 cm and the dimensions of the scintillator are discussed later in this Chapter.

therefore maximising the efficiencies of light production, collection, and transmission are particularly important. The materials used in the detector were selected on this basis.

5.2.1 The scintillators

The physical mechanisms for the conversion of the energy deposited by ionising radiation into scintillations is described in the excellent account by Birks[123]. Scintillators were one of the first radiation detectors, initially used visually by expert operators from 1908 to the early 1930's. A major advance came in 1944 when light from a scintillating screen was electronically converted by a photomultiplier tube (PM-tube) for the first time[124]. Since then scintillator-photomultiplier systems have developed into invaluable tools for many applications such as radiation detection, spectroscopy, imaging, and nuclear research. Consequently the physical and chemical properties of scintillators are well known and there is a wide variety which are commercially available (see Table 5.1).

The criteria considered most important in selecting the scintillator materials were: a high absolute scintillation efficiency (which is the fraction of energy deposited in the scintillator that is transformed into fluorescence photons); an emission spectrum that closely matches the spectral response of the photo-detector (over the range 350-550 nm for a bialkali PM-tube); and a lack of hygroscopicity in order to avoid the need of encapsulement - with such a high surface area to volume ratio absorption of water vapour could be large for hygroscopic material.

Matching the refractive index of the scintillator to the glass of an PM-tube is important when they are coupled directly because only rays incident on the scintillator- optical fibre interface at angles less than the critical angle, c, are transmitted (those incident at angles greater than c are lost through multiple total internal reflections). The critical angle can be expressed in terms of the ratio of the refractive indices of two different materials:

$$\sin c = n_1 / n_2 \qquad (5.4)$$

Material	Wavelength of maximum emission λ_{max} (nm)	Refractive index at λ_{max}	* Absolute scintillation efficiency for fast electrons (%)	Pulse 10-90% RiseTime (μs)	Principle decay time (μs)	Density (g/cm^3)
NaI(Tl)	415	1.85	11.3	0.5	0.23	3.67
CsI(Tl)	540	1.80	11.9	4	1.0	4.51
CaF_2	435	1.44	6.7	4	0.9	3.19
ZnS(Ag)	450	4.09	12.5	-	>1 (depends on fromer treatment)	4.1
Anthracene	445	-	3.8	-	0.025	1.24
NE 102 A	423	1.58	2.5**	-	0.002	1.03

Key- * The fraction of energy deposited by an electron that is converter in fluorescent photons
** Taken from Birks (123)
*** Taken as 65% of the scintillation efficiency of anthracene

TABLE 5.1.

where c is the critical angle, and n_1 is the lower refractive index (for a silica optical fibre this will be around 1.5) and n_2 is the higher refractive index (see Table 5.1). Optical matching fluid can be used effectively at the scintillator-fibre interface to increase the critical angle and reduce light trapping in the scintillator (Midlands Silicone Ltd. silicone fluid type MS 200 with a viscosity of $6x10^4$ cs was used in the present work).

Several scintillator materials have been considered as suitable, with caesium iodide doped with thallium, CsI(Tl), deemed the most suitable. CsI(Tl) has an absolute scintillation efficiency for fast electrons of 11.9%[125] that is greater than NaI(Tl) (an even better option if it were not highly hygroscopic), but its emission spectrum is a relatively poor match to the spectral response of a bialkali PM-tube (see Figure 5.2). However, it can be machined into sheets as thin as 250 μm and it can be easily cut and shaped with a scalpel. Another useful property of CsI(Tl) that may be of use is that it has a variable decay time for different exciting particles and this may be used to differentiate between various types of radiation. Although not atomically tissue equivalent, it was anticipated that transfer functions could be derived to convert spectra and quantities. Hygroscopicity for CsI(Tl) is slight, but deterioration may occur in high humidity.

Calcium fluoride doped with europium, CaF_2(Eu), is one of the most robust scintillators and it is not hygroscopic. It has a peak wavelength of emission at 435 nm that is similar to that of NaI(Tl) and that matches the spectral response of a bialkali PM-tube well, but with an absolute scintillation efficiency that is 6.7%, the relative pulse height compared with that CsI(Tl) will probably be smaller (if its emission spectrum is taken as that of NaI(Tl) in Figure 5.2 the relative pulse height is about 80% of the pulse height from CsI(Tl)). If the slight hygroscopicity of CsI(Tl) was found to be a problem then CaF_2(Eu) would be good replacement.

Zinc sulphide doped with silver ZnS(Ag) has one of the highest scintillation efficiencies with one measurement putting iit as high as 25% for α-particles[123]. Its absolute scintillation efficiency for fast electrons is 12.5% which is even higher than

for CsI(Tl) and NaI(Tl). The major problem with zinc sulphide is its high self-absorbance for the emitted scintillation light which means that it is only available as a polycrystalline powder with a mean particle size that is typically 1-25 μm. Another problem is the high refractive index of ZnS(Ag) of 2.36 means that there is increased light trapping and reduced light collection.

The organic scintillators were also considered for use as they are available in almost every possible shape, size and form. Moreover, they are more nearly tissue equivalent in composition and because they contain hydrogen, they are better for neutron detection and spectroscopy than are the inorganic scintillators. However, their scintillation efficiencies are poor, with anthracene being the most efficient having an absolute scintillation efficiency of only 3-4 %.

The main properties of the aforementioned scintillators are given in Table 5.1.

5.2.2 The photomultiplier tube and the electronic setup

The efficient conversion of light into electronic charge by the photo-detector is another crucial factor in the maximimization of the signal. The quantum efficiency, QE, is a measure of this efficiency and it is simply defined as:

QE = Number of electrons emitted / Number of incident photons

The QE for photodiodes is the highest of all photodetectors. It typically peaks at 60-80% and extends into the red. However, they possess no internal gain mechanism and this means that the tiny signals from a miniature scintillator would be swamped in the electronic noise. Avalanche photodiodes in which higher applied voltages are used to produce a gain of about 50 are a more recent improvement, but they are unstable at room temperature and require cooling.

PM-tubes on the other hand are relatively stable and are capable of gains that exceed avalanche photodiodes by 10^6. This adequately makes up for the lack of QE which typically peaks at around 25%. A thorn EMI 9789 bialkali PM-tube was therefore selected. It features a small photocathode with a diameter of 10 mm that has a particularly low dark emission that is typically 50 counts per second, and it has

Figure 5.2. The relative response of the bilkali PM-tube and the relative emission spectra of NaI(Tl) and CsI(Tl)

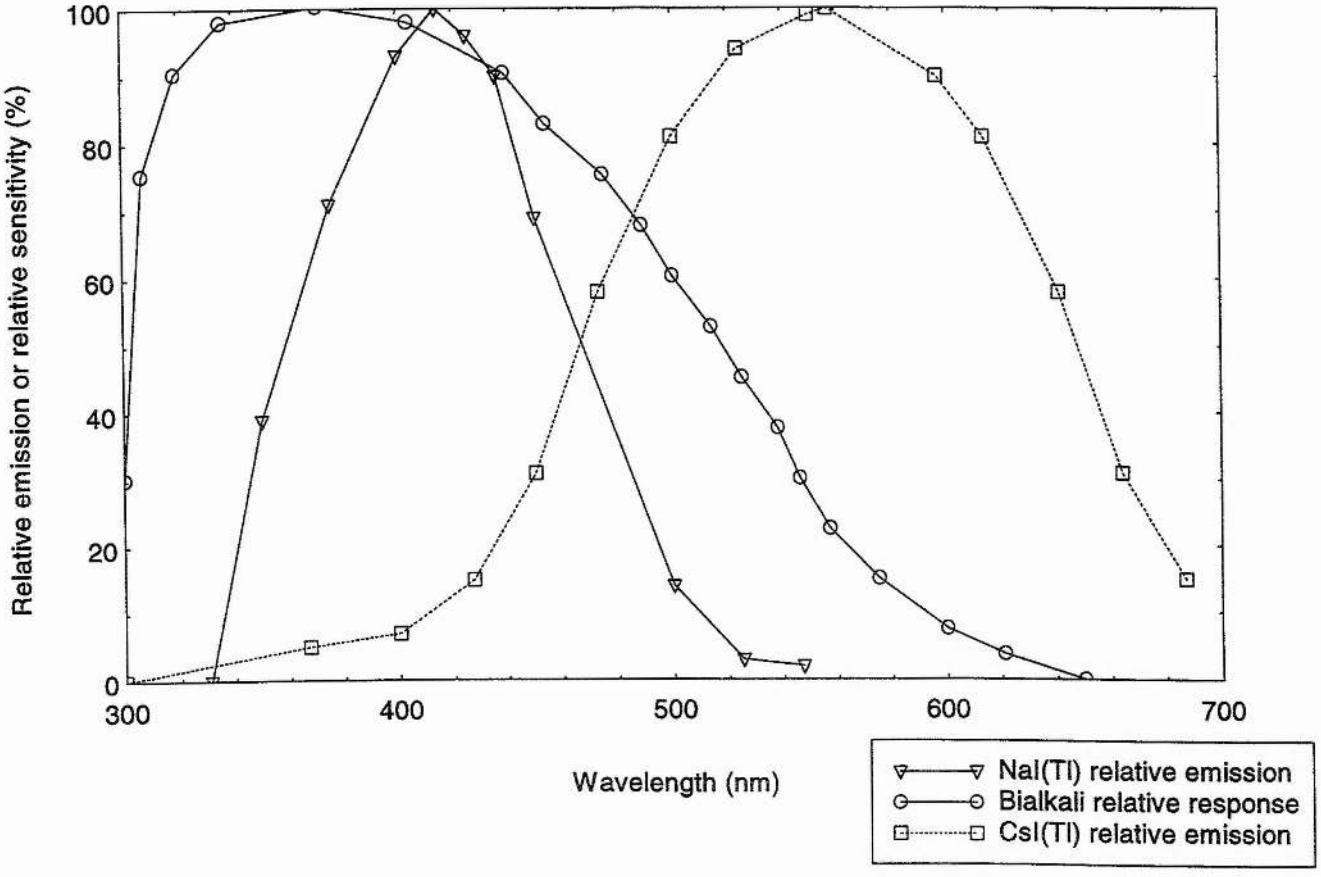

13 dynodes that are capable of producing a maximum gain of 2.5×10^7. Its relative spectral response is given in Figure 5.2 which has been produced from the manufacturer's data.

The high voltage supply and the pre-amplifier were types 572 and 142pc respectively from EG&G ORTEC and the amplifier was a TENNELEC type 243. The multi-channel buffer EG&G ORTEC type 918 was interfaced to a 486-SX IBM compatible PC and operated using Maestro for the 100-T software. The conversion gain was set to give 512 channels full scale. All data processing and analysis was performed on the PC.

5.2.3 The optical fibre

Light pipes are commonly used to guide light to a photomultiplier tube from a scintillator when strong electromagnetic fields, magnetic fields, or harsh conditions need avoiding. In the present work light would need to be guided over 20 m for remote measurements in the vicinity of a LINAC. Light pipes would be unsuitable however, due to the high light losses from relatively poor transmission (between 48-61% for typical materials over 1 m and negligible transmission over 20 m) and their rigidness (there would be several bends to negotiate). Optical fibres on the other hand, suffer low transmission losses and they are flexible.

In optical fibres light is transmitted by a series of total internal reflections. These can occur because the refractive index of the core (n_1) is greater than the refractive index of the cladding which has a refractive index n_2 (see Figure 5.4). Only light rays entering the fibre from the surrounding medium of refractive index n_0 (usually air with $n_0 = 1$) with an angle of incidence less than the acceptance angle θ_i will be transmitted without Fresnel reflection losses. Rays entering the optical fibre at angles greater than the acceptance angle will undergo reflection losses, but over short lengths of fibre significant transmission can occur. Using Snell's law and simple geometry it can be shown that:

$$n_0 \sin\theta_a = \sqrt{n_1^2 - n_2^2} \qquad (5.5)$$

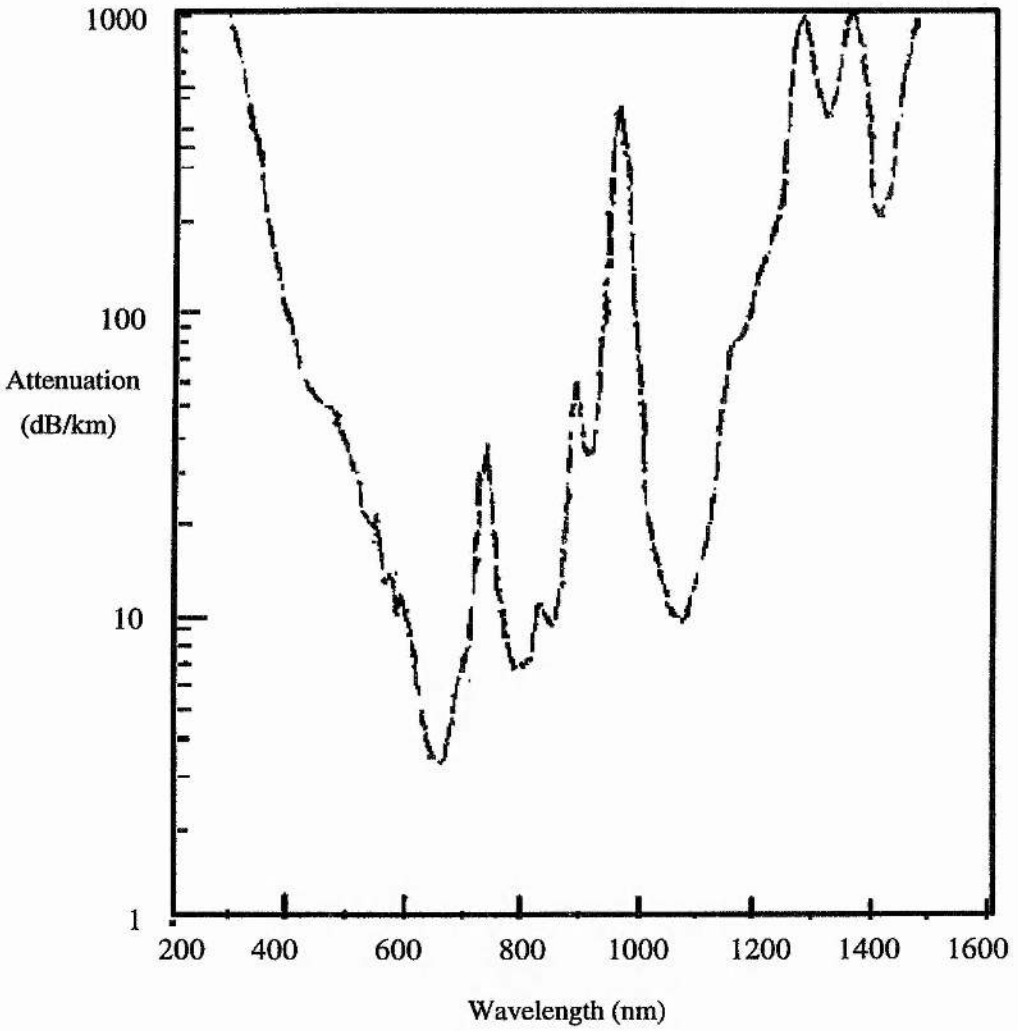

Figure 5.3. The attenuation in dB/km as a function of wavelength for a high purity silicon fibre (3M TECS type UMT-200) taken from the manufacturer's data. The fibre used in the present work had a core diamter of 1000 μm, but will have similar attenuation. Note the low attenuation for light from the emission spectrum of CsI(Tl) over the range 300 - 700 nm.

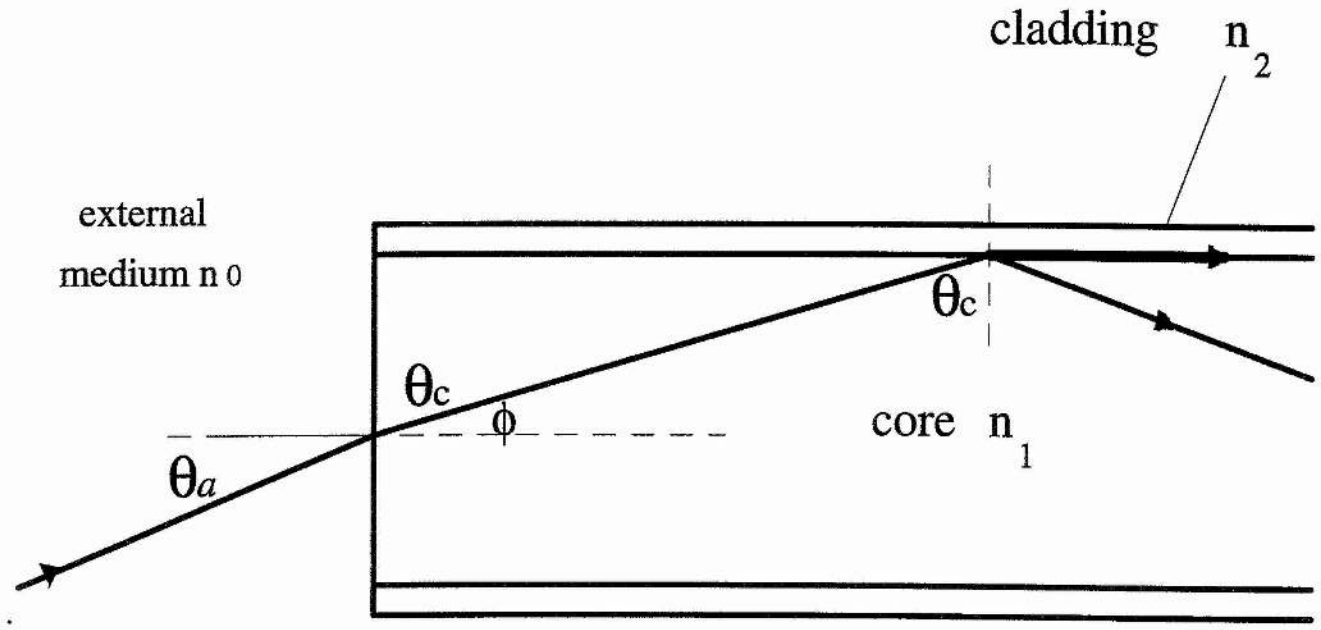

Figure 5.4. The principle of transmission by total internal reflection in an optical fibre. Rays incident at angles less than the acceptance angle θ_a are transmitted by total internal reflection. Rays outside the acceptance angle undergo partial reflection with a portion being lost by transmission into the cladding. These rays are attenuated rapidly, but for short lengths of fibre, transmission can still be considerable.

The term on the left is known as the numerical aperture, (NA), and is quoted by manufacturers for rays of light incident from air (n_0=1) . In the present project it is important to maximise the light collection at the PM-tube. Consequently, only multi-mode optical fibres with large numerical apertures were considered.

High transmission over the scintillation emission spectrum of the scintillator is essential if light losses in the optical fibre are low. Outstanding transmission can be obtained by using high purity silicon fibres. A 3M TECS™ (Technology Enhanced Clad Silica) low-OH fibre was selected for this work because of its high numerical aperture of 0.37; its low attenuation (see Figure 5.3); and hard cladding. One end was terminated with a SMA 905 Crimp and Cleave connector while at the other end, the buffer was cut away with a scalpel and the core was nicked with a diamond cutter pen for cleaving (the arrangement of one terminated end and one bare end is known as a 'pig-tail'). The terminated end was screwed into the connector of a brass plate that was used to hold the optical fibre flush to the window of the photomultiplier tube onto which a thin layer of optical matching fluid had been smeared. The scintillator could then be attached to the bare end of the optical fibre using viscous optical matching fluid or a very thin layer of cryolite clear adhesive. Light tightness along the length of the optical fibre was assured by placing the fibre within black PVC tubing. A large core diameter of 1000 μm was selected to maximise light collection and ensure the stable mounting of the miniature scintillators.

Initially a high purity fused silica fibre clad in nylon (type SFS200220N) had been purchased from Tech Optic Ltd. with a core diameter of 200 μm and a cladding diameter of 220 μm. However, mounting miniature scintillators to the end of such a narrow fibre was a technically difficult task and it was decided that wider core diameters would be more suitable for the preliminary experiments.

Preliminary work was also carried out with a polymer fibre supplied by RS Components Ltd. Comprising a polymethyl methacryalate core surrounded by a fluorinated polymer cladding and sheathed in black polyethylene, the core-cladding

diameter was 1000 μm and the numerical aperture was very high at 0.47. Although the attenuation was quite high over 20 m (about 45%) it was convenient to use as it was much less expensive and various lengths could be easily cleaved using just a scalpel.

5.2.4 Light losses along the scintillator-optical fibre system

There are three main sources of light loss in the scintillator-optical fibre system. They are: trapping of light due to total internal reflection within the scintillator; Fresnel reflection losses at the core-cladding interface of the optical fibre; and absorption losses in the optical fibre itself.

The first of these losses occurs when the light in the scintillator is incident on the scintillator fibre interface at an angle greater than the critical angle and when the scintillator has a higher refractive index than the fibre (this is often the case). Only light incident at an angle less than the critical angle will be transmitted. If the opposite face of the scintillator to the interface is covered in an excellent diffuse reflector then the total escaping fraction of light is given by:

$$E = 2\frac{\Omega}{4\pi} = \frac{1}{2\pi}\int_{\theta=0}^{\theta=\theta_c} d\Omega = \frac{1}{2\pi}\int_{0}^{\theta_c} 2\pi \sin\theta . d\theta$$

$$\therefore E = 1 - \cos\theta_c = 1 - \sqrt{1 - \left(\frac{n_1}{n_0}\right)^2} \qquad (5.6)$$

where θ_c is the critical angle, n_1 is the higher refractive index, and n_0 is the lower refractive index. It can be seen from the above equation that by matching the refractive indices as closely as possible the escaping fraction will be maximised.

In the present work the optical fibre has a refractive index of approximately 1.5 and the refractive indices of CsI(Tl) and NaI(Tl) are 1.8 and 1.85 respectively yielding escaping fractions of about 45% and 41% respectively.

The second source of light loss occurs when light is launched into the fibre at angles greater than the acceptance angle, θ_a. Referring to Figure 5.5 , the rays of light

leaving the scintillator at angles of incidence less than θ_i will be incident on the optical fibre surface within the acceptance angle, where θ_i is given by:

$$\theta_i = 1.5/1.8\ (\sin^{-1}\theta_a) \qquad (5.7)$$

The fraction of light that escapes the scintillator and is launched at an angle within the acceptance angle for transmission to the other end is denoted here by E_T, given by:

$$E_T = 1 - \cos\theta_i \qquad (5.8)$$

For the silica fibre and the plastic fibre used in this work values of E_T are 2.1% and 3.5% respectively. Some of the remaining light can be transmitted by multiple Fresnel reflections, but only over short lengths is transmission considerable. The light is lost through partial transmission into the cladding.

Attenuation by absorption and scattering, in the core material, scattering at irregularities at the core-cladding interface, and curvature of the fibre is the third source of light loss. Absorption at certain wavelengths is caused by molecular impurities. These impurities also cause scattering, as do fluctuations in temperature and composition (causing Rayleigh scattering) by interrupting the reflection paths of the light rays. Irregularities at the core-cladding interface can scatter light into the cladding. This also occurs if the curvature of the fibre is too great, because some rays will be incident at the core-cladding interface at angles less than the critical angle. The attenuation due the combination of the preceding effects in dB/km in a silica fibre is shown in Figure 5.3. For 20 m lengths of the silica fibre and the plastic fibre, the percentage transmission averaged over the CsI(Tl) emission spectrum are 72% and 43% respectively (see section 5.2.6).

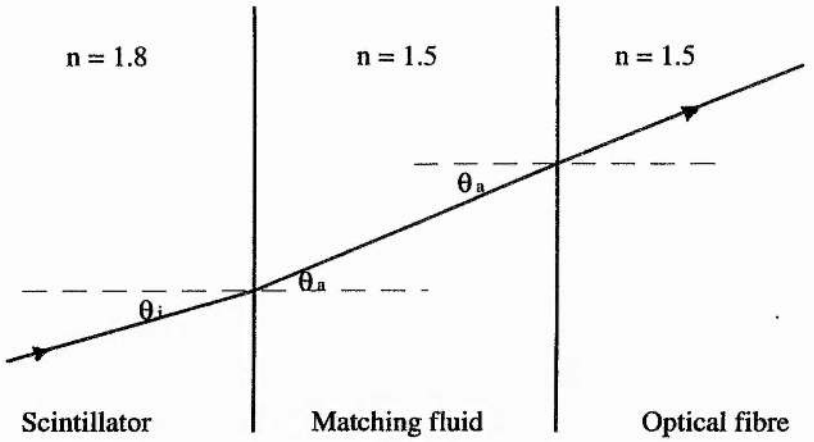

Figure 5.5. A ray diagram to illustrate the relationship between the angle of incidence and the acceptance angle of the optical fibre. The refractive indices are for CsI(Tl), the optical matching fluid, and the core of a typical optical fibre are given.

5.2.5 Estimation of the threshold signal in the scintillator-optical fibre system

When a NaI(Tl) crystal is coupled to a PM-tube directly, under optimum conditions an energy deposition of 120 eV[125] is required to release a photo-electron from the cathode of the PM-tube to give the minimum threshold signal. If the relative response of the PM-tube to the CsI(Tl) - optical fibre system is known, then the minimum energy deposition to create a threshold signal in this system can then be estimated.

The relative emission spectra of NaI(Tl) and CsI(Tl) are shown with the relative response of the bialkali PM-tube used in the present work as a function of wavelength in Figure 5.2. By multiplying the relative emission by the relative response at each given wavelength, the relative response curves of the PM-tube to scintillation light of both of the scintillators has been determined and the relative response curve of CsI(Tl) has been multiplied by a factor (11.9/11.3) to normalise it to the absolute efficiency of NaI(Tl) (see Figure 5.6).

The response curves have been multiplied by the percentage transmission through 20 m of silica fibre (see Figure 5.7) and 20 m of plastic fibre at each given wavelength to determine the effect of attenuation. Similarly the reduction in pulse

height due to the attenuation through a 2 m length of the plastic optical fibre has been obtained and is shown in Figure 5.8.

The areas under the curves are proportional to the response in pulse height at the PM-tube. The attenuation factors determined by taking the ratios of these areas are shown in Table 5.2 below together with the attenuation due to the light loss from unacceptable launch angle into the optical fibre. The threshold energy was determined by multiplying 120 eV by the inverse of the total attenuation factor, and the minimum thickness of CsI(Tl) required to see a fast electron event was determined assuming that the stopping power is approximately 0.5 keV.μm^{-1}.

	Attenuation (%)		
Process	2 m plastic fibre	20 m plastic fibre	20 m silica fibre
Bialkali response	69	69	6 9
Attenuation	91	43	72
E_T (escape transmission fraction)	12.0	12.0	7.6
Total	**7.5**	**3.6**	**3.8**
Threshold energy	1.6 keV	3.3 keV	3.2 keV
Minimum thickness of CsI(Tl) for detection of fast electrons	3.2 μm	6.6 μm	6.4 μm

Table 5.2

From the table it is evident that for 20 m lengths, the silica fibre with its superior transmission has a slight advantage over the plastic fibre. However, over a 2 m length the plastic fibre is better due to its higher numerical aperture (even 100% transmission for 2 m of the silica fibre would give a total attenuation of 5.3% - see Table 5.2 for the method used).

It is also evident that CsI(Tl) is a slightly better scintillator to use than NaI(Tl) for the 20 m lengths of optical fibre giving a relative response that is a factor of 1.06

Figure 5.6 The bialkali reponse weighted by the relative spectrum and normalised to the absolute efficiency of NaI(Tl)

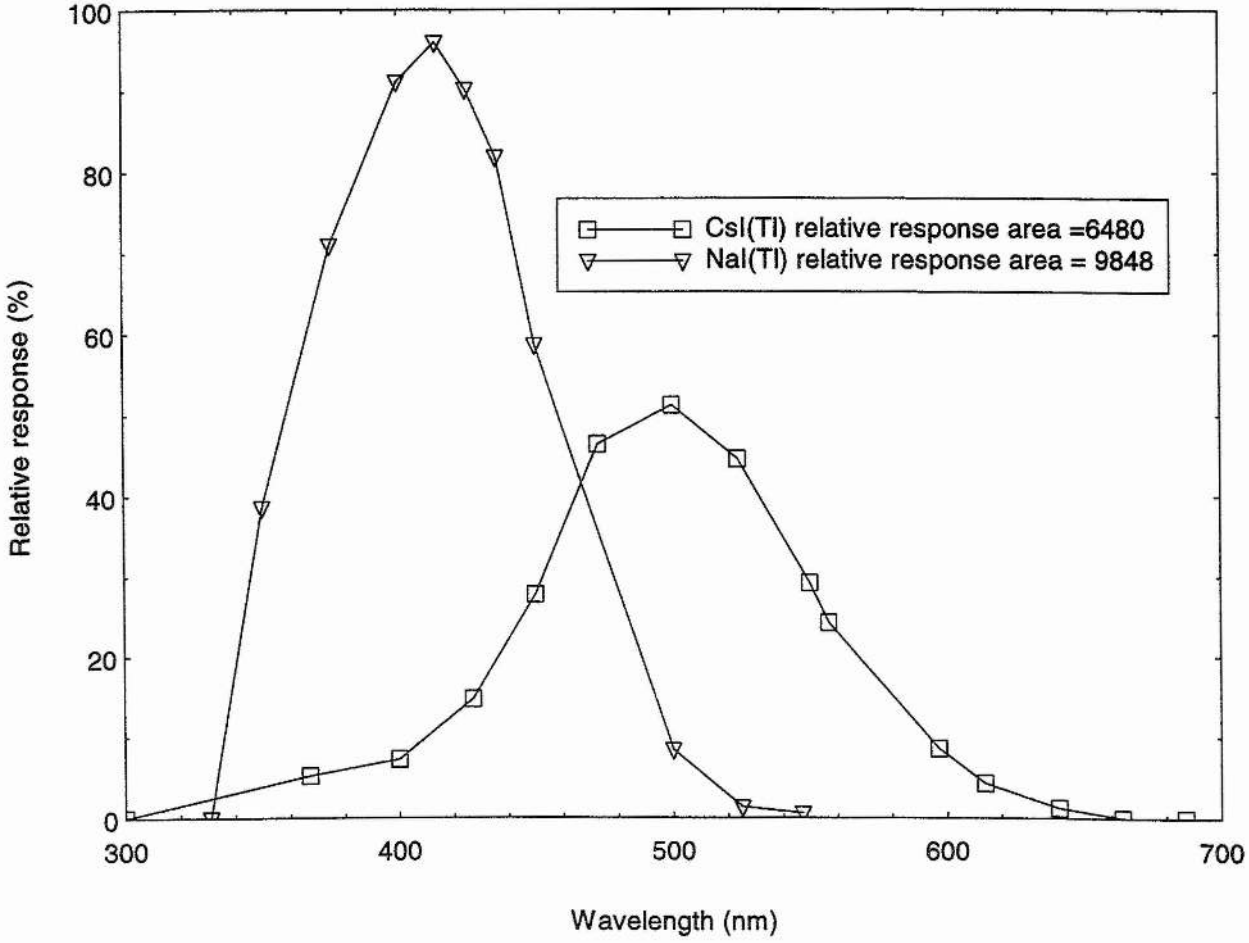

Figure 5.7 The bialkali reponse weighted by the relative spectrum and normalised to absolute effieciency of NaI(Tl)

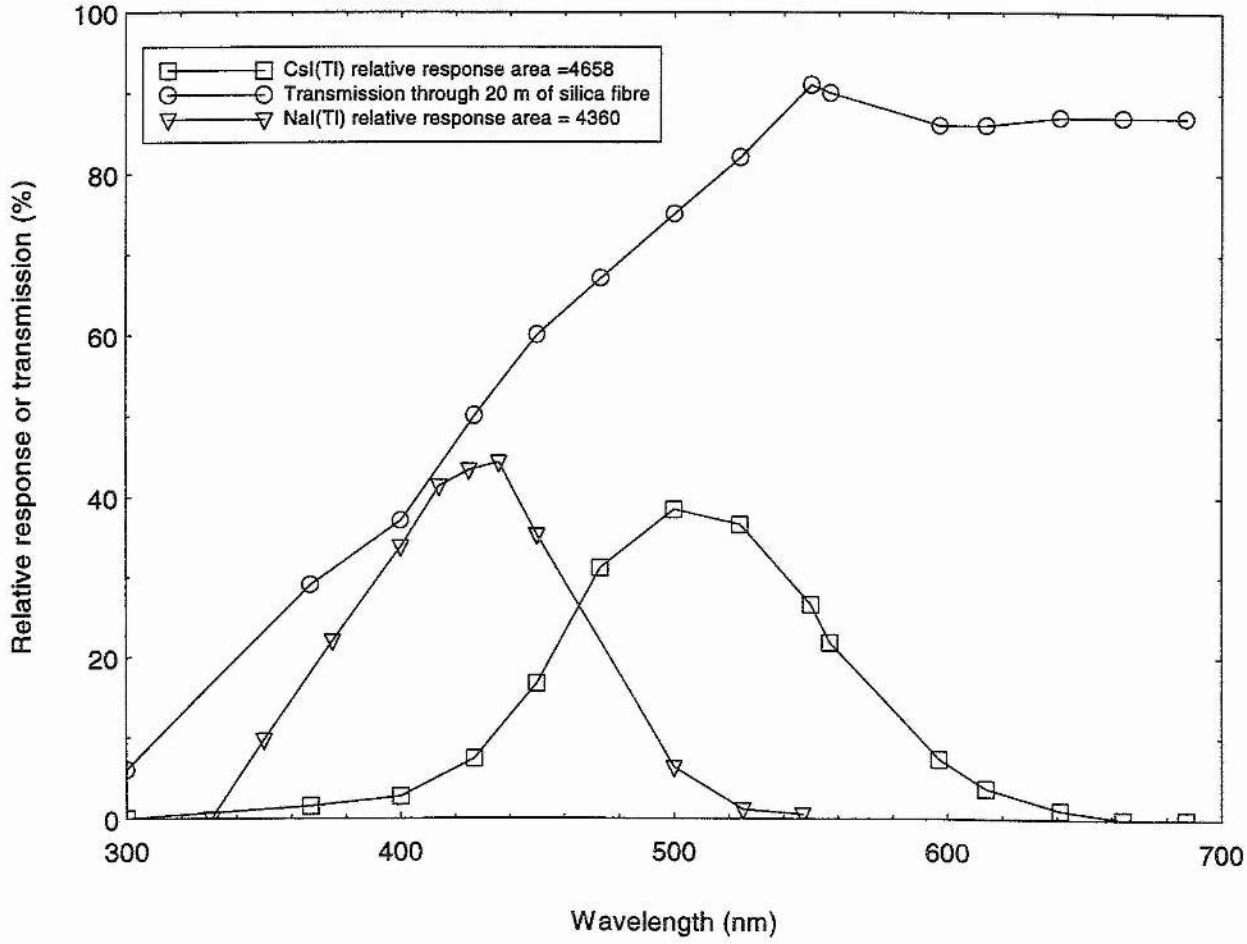

Figure 5.8 The bialkali reponse weighted by the relative spectrum and normalised to absolute efficiency of NaI(Tl) and attenuated by 2m of plastic optical fibre

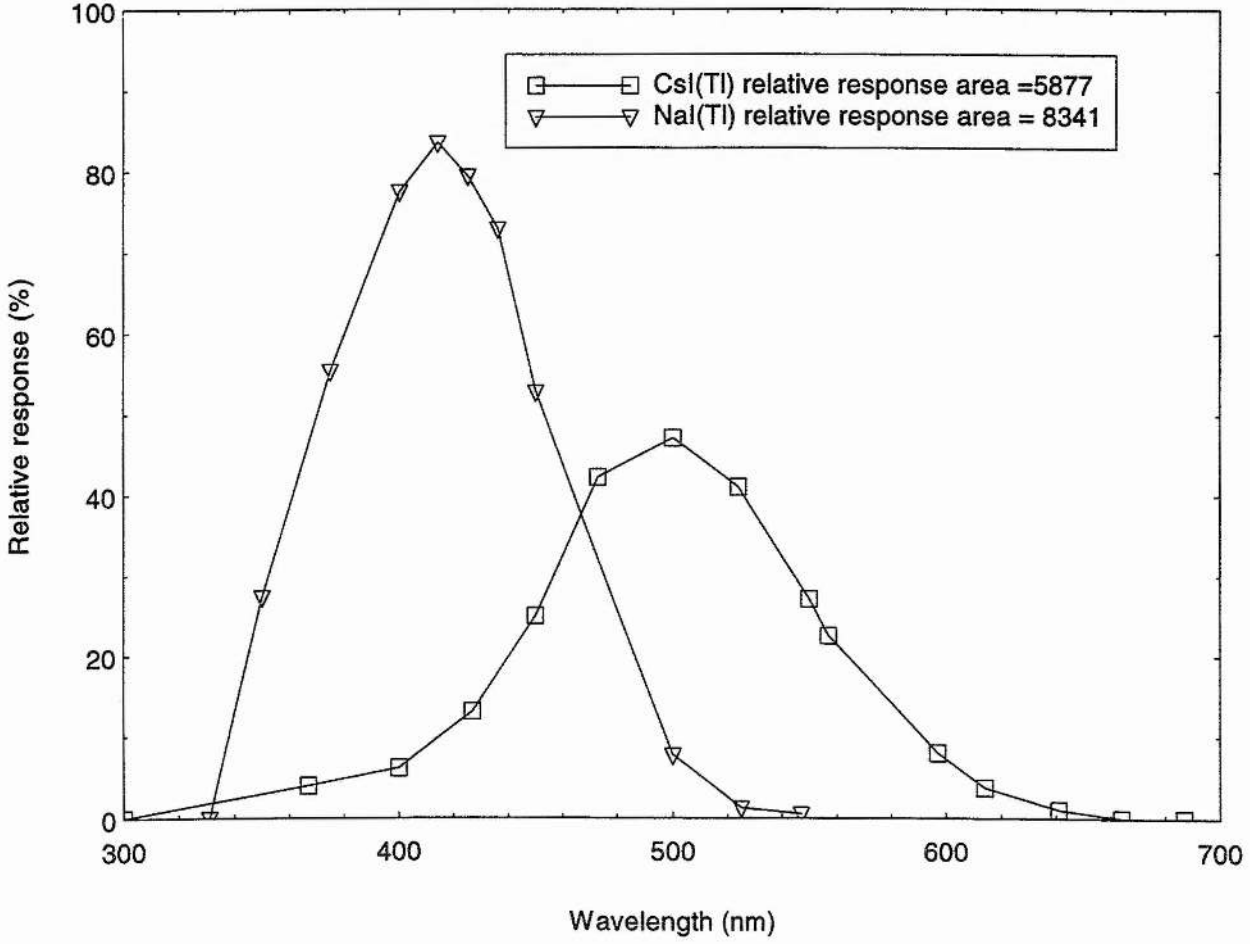

greater. Over 2 m, but for its hygroscopicity, NaI(Tl) would be the better scintillator to use.

5.3 Preliminary results

A characteristic X ray set, once capable of producing up to 4 $Gy.min^{-1}$[126], was recommissioned for the present work at the University of St.Andrews. High dose-rates were required to ensure that the intensity of photon fluence would be sufficient to yield an adequate count rate in the miniature detector.

Upon irradiation of the bare (i.e. no scintillator) plastic optical fibre, a strong signal was recorded that was attributed to scintillations from impurity traps within the fibre. Therefore it was decided to use the 200 μm core diameter high-purity silica fibre which when tested alone showed no signs of scintillations.

Field trials were conducted around the Brown-Boveri CH-20 LINAC operating in X ray mode at Ninewell's hospital, Dundee. The preliminary results using a 500 μm chip of CsI(Tl) and also CaF_2 granules attached to the 1000 μm core diameter silica fibre have been published[127]. As expected, the optical fibre was immune to noise signals induced by the r.f. fields. By monitoring the pulse shapes on an oscilloscope no pile-up, or saturation of the electronics was evident except at the isocentre. The possibility of optical fibre scintillations were discounted when irradiation of the bare 200 μm core diameter silica fibre yielded no signal above the background (this fibre was used in order that the miniature scintillators could be left attached to the larger fibre).

However, further experimentation involving changes in energy of the beam, changes in dose-rate output, variation in the source to detector distance and insertion of lead filters, revealed a strong dose-rate effect that was inconsistent with the collection of single event spectra in a miniature scintillation detector. By irradiating the bare 1000 μm core diameter silica fibre it was shown that the strong signal was actually produced in the optical fibre itself.

An extensive literature review revealed that this effect had already been discovered previously and published recently[128,129]. Suggested causes that led, in the present work, to the incorrect assumption that silica fibres do not produce light in a radiation field are as follows: a foreign body, a spec of dirt for example, obstructed the end of the 200 μm optical fibre; the end of the optical fibre may have been aligned to a insensitive part of the photocathode, resulting in a lower than expected signal that went undetected; all the measurements were spurious. Alternatively, the fibre may be of a composition not that does not scintillate at all, and the angle of irradiation may have been such that resulted in the negligible collection of the Cerenkov light (see next section).

5.4 Scintillations and Cerenkov radiation in optical fibres

Beddar *et al.*[122] when, performing measurements with their miniature water-equivalent dosimeter discovered that their silica-core optical fibre was emitting its own light from radiation interactions. Two light producing processes were isolated: Cerenkov radiation and fluorescence scintillations.

Cerenkov light, is emitted when a charged particle exceeds the speed of light through an optically transparent medium which has a refractive greater than 1 (the refractive index of light in a vacuum), or

$$\beta n > 1 \tag{5.9}$$

where β is the ratio of the velocity of the speed of light in the medium to that of light in a vacuum. For charged particles of energies in the tens of MeV and lower encountered in the present work, only electrons can meet this velocity criterion. The threshold for Cerenkov light production for electrons is given by:

$$E_{th} = m_o c^2 \left(-1 + \sqrt{1 + \frac{1}{n^2 - 1}} \right) \tag{5.10}$$

where $m_o c^2$ is the rest mass energy of the electron (0.511 MeV). For a refractive index of 1.5 (approximately the refractive index of the core of a silica fibre) then

E_{th} = 175 keV. The threshold energy needed for gamma-rays to produce Compton electrons of this energy by 180^0 scattering is approximately E_{th} = 313 keV[130]. This energy can be easily exceeded by even the scattered photons produced at high fluences around LINACs. The production of Cerenkov light is strongly directional, following the path of the charged particle in a cone with a vertex angle θ where

$$\cos \theta = 1/\beta n \qquad (5.11)$$

By irradiating a silica-core optical fibre at different angles with a mono-directional 2 MeV electron beam produced by a high energy accelerator Beddar *et al.*[128] were able to establish that the light produced in the optical fibre was indeed Cerenkov light. For their fibre with a refractive index of 1.46 the maximum light production occurred when the fibre was irradiated by the beam at 45^0 to the fibre axis, which they found was in good agreement with the theoretical value[129]. However, an unexpected result was obtained when the electron beam was fired at 90^0 to the axis of the fibre. The light emission was expected to drop to zero, and although a minimum light yield was obtained, light was still being emitted. Irradiation with a 125 kVp orthovoltage unit that produced X rays of a maximum energy 125 keV, which are below the Cerenkov production threshold, also caused light production. It was concluded that a second mechanism, fluorescence, was also responsible for the light production in the optical fibre.

The problem of light emission from the optical fibre was tackled by using a bare optical fibre in parallel to the scintillator-optical fibre combination and generating a background signal that could then be subtracted form the scintillator-optical fibre signal. The main problem with this arrangement, however, was that the background signal was often very large and variable, and in some irradiation conditions equal to the scintillator signal. Thus large errors were possible.

A second solution has been explored to eliminate the effect of the unwanted light generation by the optical fibre[17]. A spectral analysis of this light revealed that it was predominantly produced in the blue-visible region with the fluorescence portion having a peak wavelength around 460 nm, and with the Cerenkov portion which

follows an inverse cubic wavelength dependence, also located predominantly in blue. By using scintillators with added optical shifters that shifted the scintillator's light to longer wavelengths, the blue-visible light generated by the optical fibre was removed by optical filters that were inserted between the optical fibre and the PM-tube. The overall result was to reduce signal from the optical fibre generated light by up to 50%. It was anticipated that this reduction would help to reduce errors when performing the background subtraction technique.

A much greater reduction in optical fibre generated light would be required in the present work with the condensed phase microdosimeter, because the dimensions (which are proportional to the energy deposition, and hence light output) of the optical fibre exposed to radiation are of the order of three orders of magnitude greater than those of the miniature scintillator. However, the production of Cerenkov light is inefficient, at around two orders of magnitudes less than a typical scintillator, and furthermore the scintillation efficiency of the optical fibre is of a similar magnitude to the Cerenkov radiation[128]. Therefore, the signal-to-noise ratio for a condensed phase microdosimeter will be very small unless the optical fibre produced light can be reduced by over ten-fold.

5.5 Future work

A possible solution to the problem of optical fibre produced light will be applied in the near future. Through the use of pulse shape discrimination (PSD) the light from a miniature CsI(Tl) scintillator will be processed while the light produced by the optical fibre will be rejected. To understand how this can be achieved the difference in pulse shapes is explained here.

The pulse rise time of CsI(Tl) is 4 μs and its principal decay time is 1 μs making it a relatively slow scintillator. In contrast Cerenkov radiation is due to a process determined by the time interval that elapses from when a charged particle travelling with some initial velocity (described already) slows down past its threshold velocity. This occurs in a matter of picoseconds. The rise time and decay time and

decay times of fused silica (the optical fibre core material) are unknown to the present author, however, they are currently being investigated. It is expected that they too, are fast in relation to the scintillation light production of CsI(Tl) because silicate glasses incorporating lithium are used for neutron time-of-flight measurements. If it is found to be the case that the pulse shapes of the silica optical fibre and CsI(Tl) are similar than alternative optical fibre materials would be used. Polymers, which probably act as organic scintillators would be expected to have similar nanosecond rise times and decay times.

Pulse shape discrimination (PSD) techniques would be applied to reject the fast pulses expected from the optical fibre produced light. Two well established approaches for PSD are under consideration. The first method involves passing the pulse through a shaping network, such as a double delay line shaper, to produce a bipolar pulse. The time interval between the start of the pulse and the zero cross-over point does not depend on amplitude, but instead it is a function of pulse shape and rise time. A leading trigger set to its minimum threshold and a second trigger that senses the zero cross-over point are the usual means to measure this time interval. This measured time interval is then converted to pulse amplitude by a TAC. On feeding the output of the TAC to a single-channel analyser (SCA), the selection of pulses within a desired time interval band is made possible. The SCA is then used to gate the pulse-recording system for acceptance of pulses in the accepted band only.

The other conventional PSD technique under consideration involves independent measurements of the integrated charge over two different time regions of the pulse. For similarly shaped pulses, even of differing amplitudes, the ratio of the signals is approximately constant.

Assuming the problem of the optical fibre produced light is overcome, further improvements that involve maximising the light collection from the miniature scintillator will be adopted. Firstly, the length of the optical fibre will be reduced to about a metre, or less, to reduce attenuation, and secondly wider diameter fibres that distribute the light more evenly over the PM-tube photocathode will be used to

overcome problems such as the non-uniformity of the photocathode or small particles of dirt obstructing the end of the optical fibre. Liquid light guides produced by LUMATEC are available in core diameters of up to 8 mm. They are relatively inexpensive with high transmission charactersitics.

Naturally, short lengths of fibre will make the detector impractical for application around LINACs. Brachytherapy, radiotherapy utilising implanted radionuclides, is the main application envisaged.

CHAPTER 6
CONCLUSIONS, DISCUSSION, AND FUTURE WORK

6.1 Photoneutron dosimetry

Measurements of the spatial distribution of the photo-neutron yield from the Brown Boveri CH-20 LINAC operating at 10 MV at Ninewells Hospital, Dundee, were completed successfully using a neutron activation technique involving indium wire housed in a new design of moderator that was optimally designed to suit the photo-neutron energy spectrum. Notably, the optimum thickness of moderator was found by experiment to be only 2.5 cm which is very much smaller than the 15 cm normally recommended for fast neutron measurements [7]. The new neutron fluence monitor has a sensitivity enhanced by a factor of two over previous monitors, and it greatly improved the accuracy in measuring the low intensity photo-neutron fluence rates in the treatment room. Photoneutron equivalent dose-rates of up to 0.1% of the useful treatment dose were measured and even these levels are sufficient to constitute a potential radiological hazard.

The use of a phantom for *in-vivo* style measurements is recommended because the patient-produced photoneutrons can be measured at the same time as the accelerator-produced photoneutrons. In general there is a lack of photoneutron measurements, particularly so at the lower X ray energies (6-10 MeV nominal photon energy). More measurements are therefore needed to establish the degree of hazard at these lower energies near the photoneutron production threshold.

A review of the literature revealed the dramatic increase in photoneutron production (a function of the cross-section) evident for high energy LINACs producing X rays with energies of $\geq$ 18 MV. Over the course of a typical treatment of 40 Gy of 25 MV X rays, for example, the accelerator produced photoneutrons alone would induce an equivalent dose of 400 mSv.

Added to this would be the equivalent dose due to the photoneutrons and other photonuclear products produced in the patient (see section 2.4.2.2).

Recently Manfredotti *et. al.*[29] through calculation and measurement estimated that the neutron effective dose received by the patient from a typical treatment dose of 40 Gy of 15 MV X rays is 900 mSv. This value of effective dose is about a magnitude higher than that expected by comparison with the measurements of equivalent dose around other 15 MV LINACs. This discrepancy is explained as follows: Manfredotti *et al* used TLDs and albedo dosimeters at various depths and positions within a phantom, and this included placing them within the treatment field where they found an over-response due to the massive photon fluence there. This apparently, they left unaltered. Their value of 900 mSv, however is not inconsistent with what might be expected from a 25 MV treatment.

Expecting there must be a significant risk from such high equivalent doses of photoneutrons, it was decided by the present author to review risk estimates for photoneutrons. In NCRP Report 79, which is the main authority on photoneutron contamination, the risk is considered to be very low. The report quotes a risk assessment that 5×10^{-6} fatal malignancies per year from a typical treatment of 50 Gy of 25 MV X rays. This was a surprisingly low risk to the present author and further investigation that was warranted revealed a misprint. The work that NCRP were quoting was by Nath *et al.*[2] who had actually put the risk at an order of magnitude greater.

6.2 Photoneutron risk assessment

Nath *et al.*'s estimation that 5×10^{-5} fatal malignancies per year due to neutrons may follow a typical treatment of 50 Gy of 25 MV X rays was based on the best available risk coefficient of Rossi and Mays[132] of 2.8×10^{-5} excess leukaemias per neutron cGy per year per person. This they multiplied by 5 to take into account all the possible fatal malignancies to arrive at 1.40×10^{-4} fatal

cancers per neutron cGy per person per year (note the use of absorbed dose rather than dose equivalent). Since then the risk coefficients have changed significantly. Repeating the estimation, with a neutron integral dose of 5 g.cGy/(treatment cGy), to a 70 kg patient (the same values used by Nath *et al.*, which take into account the photoneutron production in both the accelerator and the patient's body), but this time using the current nominal probability coefficient from ICRP 60[17] of 5×10^{-2} Sv^{-1}(fatal cancers) per year, the number of fatal cancers per year per person is found to be 3.6×10^{-3} due to neutrons following a typical treatment of 50 Gy of 25 MV X rays.

Using Manfredotti *et al.*'s neutron effective dose to the patient of 900 mSv from a typical treatment of 40 Gy of 15 MV X rays, the number of fatal cancers per year per person is 4.5×10^{-2}! This alarming result is probably an order of magnitude too high.

The most recent risk assessment published is from Kliauga and Amols[6]. They attempted to take a worst case scenario. Using the manufacturers' data for the maximum photoneutron yield permissible from a 20 MV LINAC, they estimated that this would result in a dose equivalent of 200 mSv for a treatment dose of 70 Gy. Furthermore, they assumed that all of the 42,000 radiotherapy patients treated by high energy LINACs in the USA in a year were treated on these 20 MV machines and would be long-term survivors. Using Q = 10 and the nominal probability coefficient of 0.06 $Sv.yr^{-1}$ they estimated that 500 fatal malignancies per year would occur. This corresponds to 1.2×10^{-2} malignancies per year per course of a 70 Gy treatment. Modernising, as previously with Nath *et al.*'s risk, and considering a treatment of 50 Gy, 1.4×10^{-2} malignancies per year, would result.

The above calculations are, of course, just rough estimates. The validity of the assumptions used will not be discussed here as the approach to determining a precise value of the risk would be misconstrued. After all, the risk being assessed is to people who already have a serious form of cancer, and the

activity of radiotherapy is required for their survival. In a United National Scientific Committee on the Effects of Atomic Radiation (UNSCEAR) report[133] it is stated in effect, that the seriousness of the primary disease requires that little consideration be given to any deleterious effects of radiation that might occur many years after successful treatment. Therefore, as already mentioned, ALARA is the appropriate principle to follow to minimise photoneutron hazards to patients. This means that LINACs working at under about 18 MV should be used preferentially.

This conclusion is reinforced by a study into the optimisation of the X ray treatment beam energy[134]. It was found that there is no treatment that cannot be optimally performed by an X ray beam energy of 15 MV, or less. Even in the treatment of deep-seated tumours in large patients where energies of over 15 MV were expected to be best, it was shown that the treatment could be performed just as well by 10-15 MV machines, (although the former higher energies would be better if the patient was extremely large, or obese). It was concluded, that with advances such as multi-leaf collimators, a radiotherapy department should seriously consider whether the number and types of treatment they were expecting to perform merited the use of higher energy machines (> 15 MV). One experienced clinical physicist reported that even an energy as low as 8 MV was the maximum treatment energy that was routinely required throughout his working life[135].

6.3 Microdosimetry in low-LET radiotherapy

Kliauga and Amols[6] were the first to prove that microdosimetry was possible in close proximity to the isocentre of a high energy LINAC utilising a TEPC, albeit the ultra-miniature counter (although microdosimetry had already been achieved in this work in the treatment room's maze exit using a more conventional TEPC). However, this miniature TEPC is still very much a

research tool and there is still a need for instrumentation that can routinely monitor the quality of the radiation under clinical conditions.

The application of such a microdosimeter would be mainly for radiation protection. The quality of the radiation field can be obtained directly with the quality factor, Q(y), expressed as a function of lineal energy. Moreover, as microdose spectra are differential spectra of radiation quality, their shape is very sensitive to slight changes in the radiation energy and intensity as may be caused, for example, by the slight non-alignment of a wedge filter, or a collimator.

Microdosimetric parameters do not relate well to clinical RBE's in low-LET radiotherapy[134]. Even for beams ranging form 1-50 MeV where there can be considerable variation in $\overline{y_d}$ (see Table 4.1) the variation in RBE's is generally slight. However, high-LET microdosimetry has been more successful and it can be used by the clinician to confirm the correct selection of RBE's for the treatment beams. Brachytherapy using low-LET radiations has been identified as a field where microdosimetry may be useful to fulfil such a role.

6.4 Condensed phase microdosimeter for application in brachytherapy

Brachytherapy is radiotherapy through the interstitial, intracavitiy and surface application of discrete sources in the treatment of malignant disease. In general the mean energy of the photon sources used in brachytherapy are much lower than those encountered in external beam therapy. Typically they range form 1.25 MeV for ^{60}Co down to 28 keV for ^{125}I.

Microdosimetric parameters could be useful for confirming the RBE to allocate for use with some of the lower energy sources. For example, the microdose spectrum of ^{125}I has y values that are approximately one order of magnitude greater than those of ^{60}Co with the value of $\overline{y_d}$ being twice as large. The RBE of ^{125}I should be taken as 1.85 relative to ^{60}Co for low dose-rate treatments, but this reduces to 1.15 for high dose-rate treatments[136].

In brachytherapy the spatial distribution of the dose is calculated by recommended methods [139] but because of complicating factors such as the type, number, intensity and geometry of the radiation sources; and the size and shape of the tumour, this is never entirely satisfactory. Consequently much of the scientific effort has concentrated on devising methods for the direct internal measurement of the dose distribution.[137]. Some small degree of practical success has been achieved in this but here also there are limitations associated variously with the stability and reproducibility of the detector; the minimum sensitivity for an energy deposition event; calibration of event sizes; safety factors for the patient and, importantly, the inability of the detectors to provide information on the radiation field quality which may change despite constant dose.

It is proposed to apply the condensed phase microdosimeter to the monitoring of the quality and dose delivered to the tumour by a complex arrangement of radionuclide sources mounted internally in the patient. It has the advantage that no voltages are applied to the detector and this is important from patient safety. On the other hand there are complications to be solved in relating the interpretation of observed spectra in caesium iodide to tissue for conditions of charged particle equilibrium.

The condensed phase microdosimeter will initially give a measure of the dose in caesium iodide, D_{cs}, and a measure of the microdosimetric quality in caesium iodide. This will be useful for obtaining the relative distribution of dose and quality around the brachytherapy sources. For a measure of the dose in tissue, however the situation is more complex.

In a gamma field of fluence, Φ, and energy, E, assuming conditions of charged particle equilibrium and negligible perturbation of the photon spectrum, the kerma[142] in the caesium iodide detector, K_{cs}, can be scaled to the kerma in tissue, K_t, using the appropriate mass energy transfer coefficients, thus:

$$\frac{K_t}{K_{cs}} = \Phi E\left(\frac{\mu_{tr}}{\rho}\right)_t \Big/ \Phi E\left(\frac{\mu_{tr}}{\rho}\right)_{cs} \qquad (6.1)$$

where $\left(\frac{\mu_{tr}}{\rho}\right)_{cs}$ and $\left(\frac{\mu_{tr}}{\rho}\right)_t$ are the mass energy transfer coefficients in caesium iodide and tissue respectively. In these conditions of charged particle equilibrium the kerma is approximately equal to the absorbed dose, then:

$$D_t = D_{cs}\left(\frac{\mu_{tr}}{\rho}\right)_t \Big/ \left(\frac{\mu_{tr}}{\rho}\right)_{cs} \qquad (6.2)$$

Thus, the dose in tissue, D_t can be determined. For a spectrum of photon energies the mass energy transfer coefficient should be averaged over that spectrum. In brachytherapy the sources used have well known spectra for which the mass energy transfer coefficients are also well known[143]. However, *in vivo*, these spectra are likely to change drastically through considerable scattering and absorption by inhomogeneities e.g. bones. Thus further work is needed to correct for the degradation of the spectra if the dose in tissue is to be determined using the condensed phase microdosimeter.

For measurements of absorbed dose in tissue in a photoneutron field (relevant to teletherapy and also brachytherapy using ^{252}Cf) the caesium iodide scintillator would have to be replaced by an organic scintillator with a high hydrogen content, such as NE-102. This would allow for the detection of proton recoils. The conversion factors for the transfer of a tissue substitute (i.e. the organic scintillator) dose in a neutron field to a dose in tissue are given in ICRU in Report 44[142].

The microdose spectrum for a CsI(Tl) 1 μm simulated sphere from a ^{241}Am photon source has been calculated analytically and is shown in Figure 6.1. It clearly shows that the crossers dominate the spectrum. Microdose spectra will be obtained for other radiation sources and site diameters as a means to guide the choice of detector size.

Figure 6.1 Calculated microdose spectrum in CsI

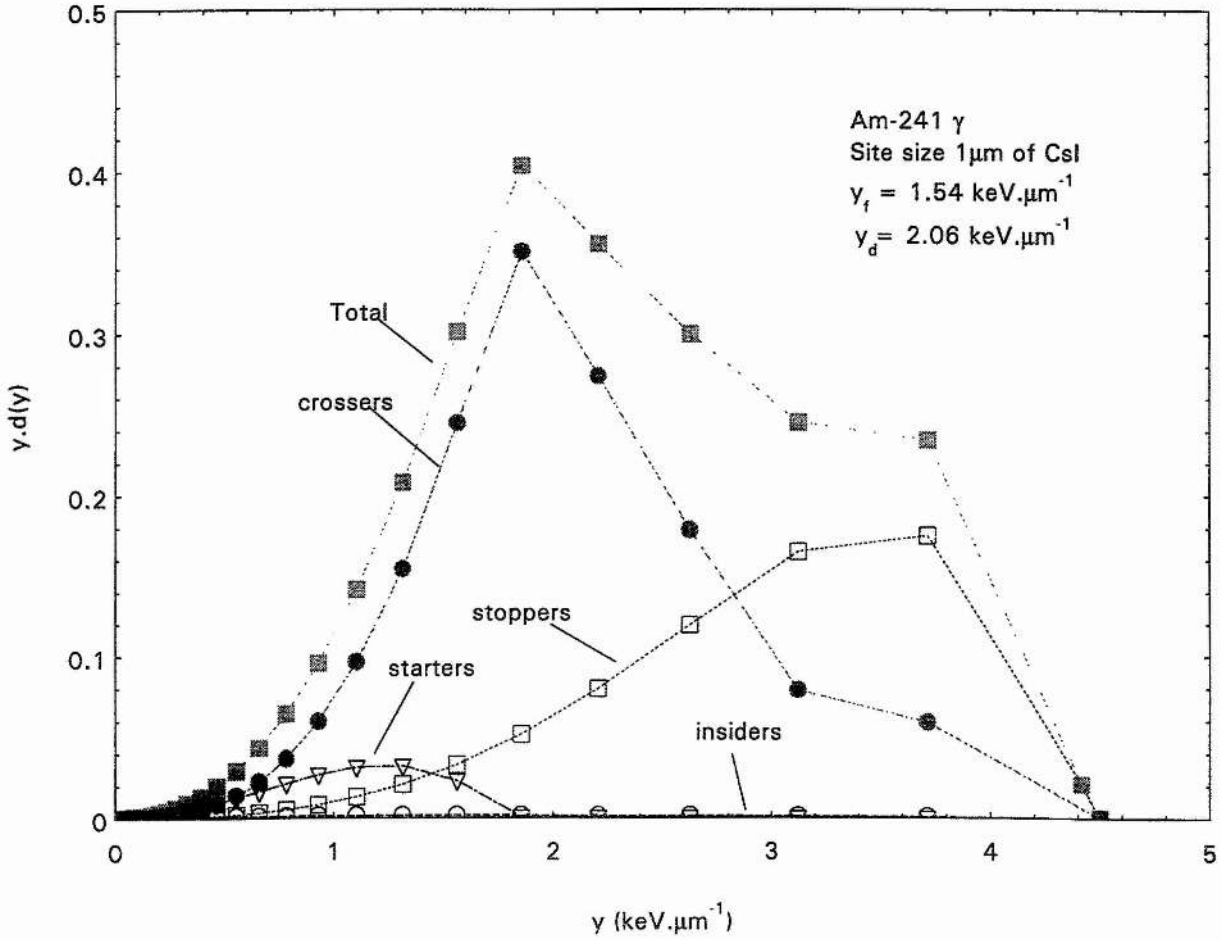

With a successfully completed instrument, designed to be physically similar to an endo-scope, the clinician will be able to pursue fundamental studies *in-vivo* to optimise the radiation effectiveness at the tumour. At present such techniques depend heavily on calculation with the inevitable uncertainties.

Appendix

Ranges of electrons

As a concept, range is less definite for electrons than for heavy charged particles, because the electron total path length is considerably greater than the distance of penetration along the initial velocity vector. It is useful to consider two different classes of range, as defined by Attix[140]:

(i) The range of a particle of a given type and initial energy in a given medium is the expectation value of the path length (p) that it follows until it comes to rest (excluding thermal motion).

(ii) The projected range of a charged particle of a given type and initial energy in a given medium is the expectation value of the furthest depth of penetration of the particle in its initial direction.

Usually, ranges are determined by measuring the transmission fraction, η, through a known thickness of absorber, t. Several definitions of the range have evolved due to the strong influence of scattering and straggling effects on the shape of the transmission curve. With reference to the schematic Figure A1, the most important ranges are [141]:

$\mathbf{R_m}$ is the maximum range. With this thickness of absorber, the recorded transmission reduces to an undetectable level i.e. below the detector's minimum threshold. Thus R_m is a subjective quantity. It is usually greater than the extrapolated range.

$\mathbf{R_{EX}}$ is the extrapolated range. It is determined by extrapolating the linear portion of the transmission curve to zero. For low electron energies this task becomes more subjective because the linear portion of the curve tends to be short. To a good approximation the extrapolated range is equivalent to the CSDA range for fast electrons in low-Z media.

$\mathbf{R_{50}}$ is the median range. This is the also the projected range, and it is given by the thickness of absorber for which the transmitted fraction is reduced to 50%.

$\mathbf{R_{CSDA}}$ is the continual slowing down approximation range.

$\mathbf{R_q}$ it the transmission range. Where q is an arbitrarily selected residual transmitted percentage, typically 1%.

Figure A1. Ranges of electrons

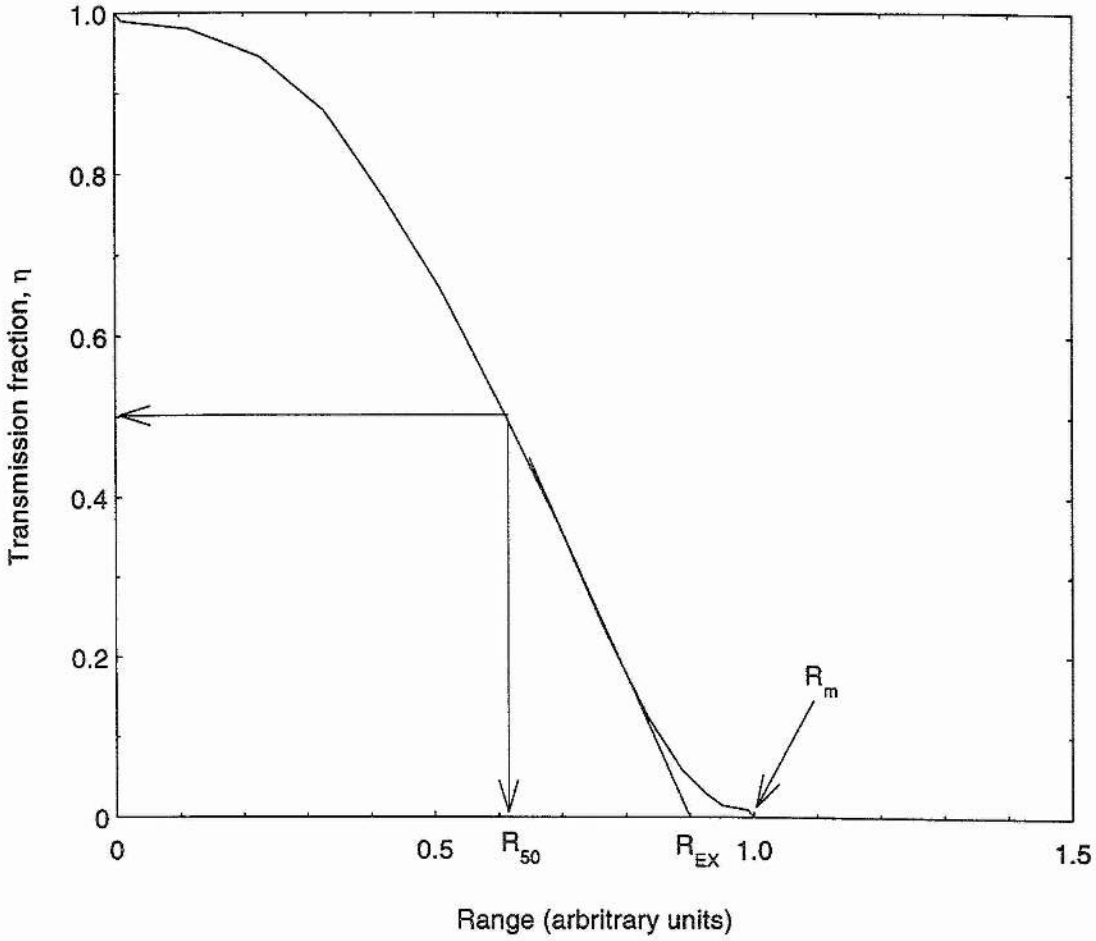

Figure A2. Activation data at various positions

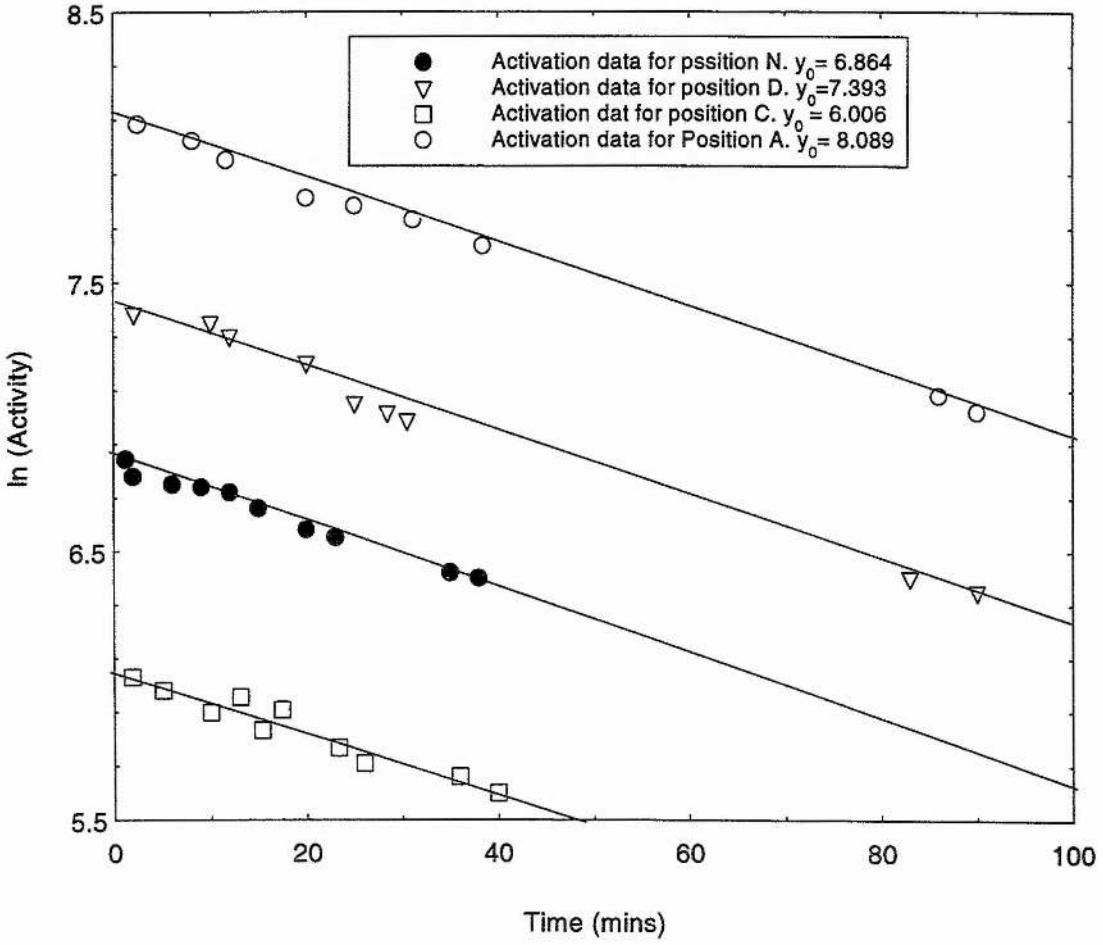

Figure A3. Activation data at various positions

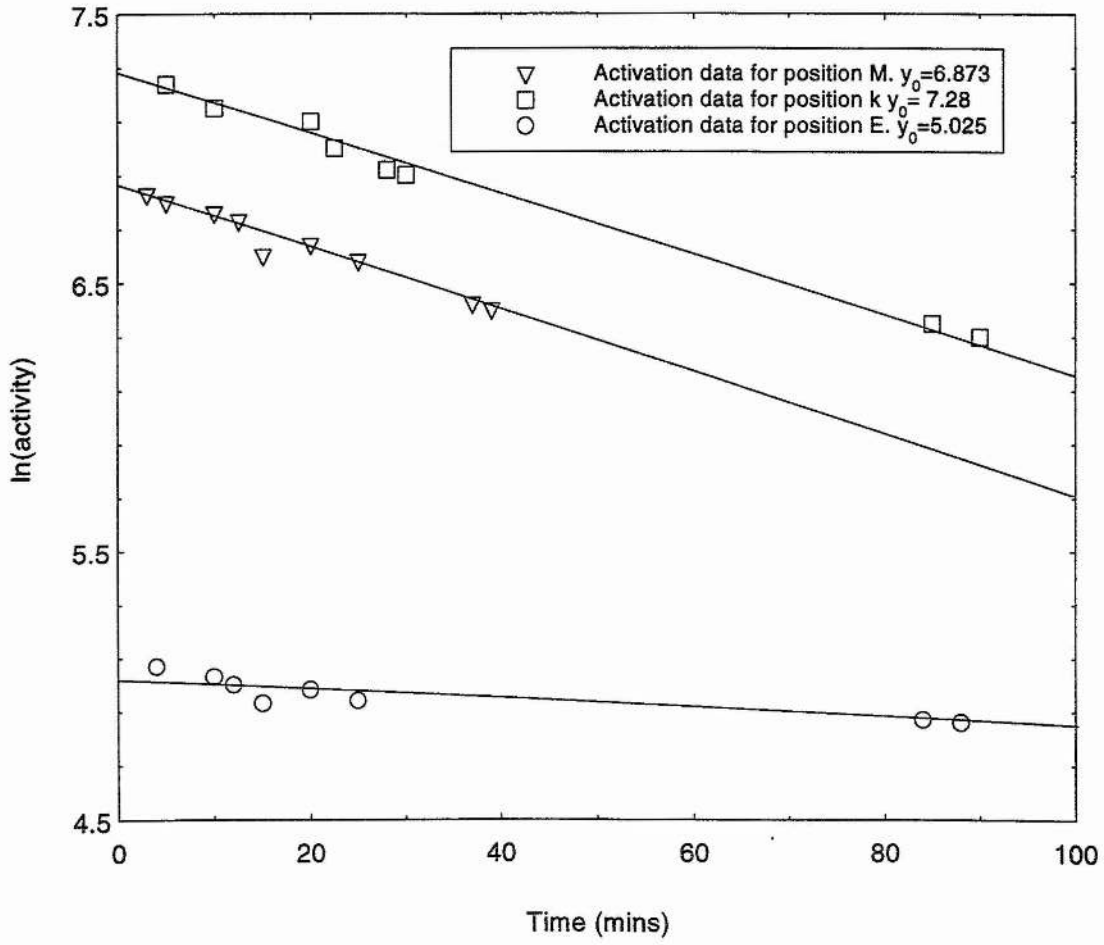

REFERENCES

1. Ionising Radiations Regulations for Medical Use. **1333** HMSO, London.(1985)
2. Nath, R., Epp, E.R.,Laughlin, J.S., Swanson, W.P. and Bond,V.P. *Neutrons from high energy X-ray medical accelerators: an estimate of risk to the therapy patient.* Medical Physics **11** 231-241 (1984).
3. ICRU Report **42** *Use of computers in external beam radiotherapy with high energy photons and electrons.* ICRU, 790 Woodmont Ave, Washington DC 20014, USA (1987).
4. ICRU Report **35** *Radiation dosimetry: electron beams with energy between 1 and 50 MeV.* Ibid.(1984).
5. Allen, P.D and Chaudhri, M.A. *Photoneutron production in tissue during high energy bremsstrahlung radiotherapy.* Phys. Med and Biol. **33** 1017-1036 (1988).
6. Kliauga, P. and Amols, H. *Photoneutrons from high energy medical linear accelerators: measurement of the spectrum and dose using a miniature proportional counter.* Int. J. Radiat. Biol. Phys. **31** 3 629-633 (1995).
7. NCRP Report **79** *Neutron contamination from medical electron accelerators.* National Council on Radiation Protection and Measurements, 7910 Woodmont Ave., Bethesda, MD20814 US (1984).
8. Bulow, B. and Forkman, B. *Photonuclear cross-sections.* In *Handbook on nuclear activation cross-sections.* Technical Report Series **156** 475-558. IAEA (1974).
9. Dietrich, S.S and Berman, B.L. *Atlas of photoneutron cross-sections with monoenergetic photons.* Atomic and Nuclear Data Tables. **38** 199-338 (1988).
10. Fueller, E.G. and Gerstenberg H.M. NBS Report NBSIR 83-2742 (1983-1986).
11. Kase, K.R., Mao, X. and Nelson, W.R. *Photoneutron yields in electron beams from 10 MeV to 10 GeV.* Portsmouth 94 Proceedings 113-116 (1994).
12. Swanson, W.P. *Improved calculation of photoneutron yield released by incident electrons.* Health Phys. **37** 347 (1979).
13. Nath, R., Price, K.W, and Holeman, G.R. *Mixed photon-neutron field measurements.* NBS SP 554 p87. (US Government Printing Office, Washington (1979).

14. McCall, R.C., Jenkins, T.M., and Shore, R.A. *Transport of accelerator produced photoneutrons in a concrete room.* IEEE Trans, Nucl. Sci. **NS-26** (1) 1593 (1979).
15. ICRU Report **33** *Radiation quantities and units.* ICRU, 790 Woodmont Ave, Washington DC 20014, USA (1980).
16. ICRP *Recommendations of the International Commission on Radiological Protection.* Publication **26**. (Oxford: Pergamon Press) (1977).
17. ICRP. *1990 Recommendations of the International Commission on Radiological Protection.* Publication **60** (Oxford: Pergamon Press) (1991).
18. ICRU Report **39** *Determination of dose equivalents resulting from external radiation sources.* Ibid.(1985).
19. ICRU Report **40** *The quality factor in radiation protection.* Ibid.(1986).
20. Rossi, H.H. and Zaider, M. *Microdosimetry and its applications.* Springer, New York (1996).
21. AAPM *Neutron measurements around high energy X-ray radiotherapy machines* AAPM **19** (American Association of Physicists in Medicine, New York) (1986).
22. Beckurts, K.H. and Wirtz, K. *Neutron physics.* (Springer Verlag, Berlin). (1964).
23. IAEA *Neutron fluence measurements* IAEA Technical Report Series **107** (International Atomic Energy Agency, Vienna) (1970).
24. ICRU **26** *Neutron dosimetry for biology and medicine.* Ibid (1984).
25. Tochlin, E. and La Rivere, P.D. *Neutron leakage characteristics related to room shielding.* p145 in **NBS-554** (US Government Printing Office, Washington) (1979).
26. Price, K.W., Nath, R., and Holeman, G.R. *Fast and thermal neutron profiles for a 25 MV x-ray radiotherapy machine.* Med. Phys. **5** 285 (1978).
27. JEFPC. OECD Nuclear Energy Agency (Le Seine St. Germain, 12 Boulevard des Iles, 9213u Issy - les- moulineurs, France) (1994).
28. Holeman, G.R., Price, K.W., Frieman, L.F, and Nath, R. *Neutron spectral measurements in an intense photon field associated with a high-energy x-ray machine.* Med. Phys. **4** 508 (1977).
29. Manfredotti, C., Nastasi, U., Ornato, E. and Zanini, A. *Evaluation of the undesired neutron dose equivalent to critical organs in patients treated*

by linear accelerator gamma ray therapy. Radiat. Prot. Dosim. **44** No.1/4 pp. 457-462 (1992).

30. Anderson, D.W. and Hwang, C.C. *Accelerator room photoneutron and photon background measurements using thermoluminescent dosimeters.* Health Phys. **44** 115 (1983).
31. Harvey, J.R. *The dependence of a personal neutron dosimeter which utilises a thermal neutron detector at the body surface.* Rep.RD/B/N827, Berkeley Nuclear Lab., Berkeley, U.K.
32 Fleischer R.L., Price, P.B. and Walker, R.M. *Nuclear tracks in solids.* (University of California Press, Berkeley) (1975).
33. Sherwin, A.G, Pearson, A.J, Richards, D.J and O'Hagan, J.B. *Measurement of neutrons from high energy electron linear accelerators.* Radiat. Prot. Dosim. **23** No.1/4 pp. 337-340 (1988).
34. Apfel, R.E *The superheated drop detector.* Nucl. Instrum.Methods **162** 603-608 (1979).
35. Ing, H. and Birnborn, H.C. *A bubble-damage polymer detector for neutrons.* Nucl. Tracks Radiat. Meas. **8** (1) 285-288 (1984).
36. Nath, R., Meigooni, A.S., King, C.R., Smolen, S., D'Errico, F. *Superheated drop detector for determination of neutron dose equivalent to patients undergoing high-energy x-ray and electron therapy.* Med. Phys. **20** (3) (1993).
37. Ipe, N.E., Busick, D.D. and Pollack, R.W. *Factors affecting the response of the bubble detector BD-100 and a comparison of its response to CR-39* Radiat. Prot. Dosim. **23** 1/4 135-138 (1988).
38. Gudowska. I. *Measurements of nuclear radiation around medical electron accelerators by means of ^{235}U fission chamber and indium foil activation.* Radiat. Prot. Dosim. **23** 1/4 345-348 (1988).
39. Wall, B.F *Fast neutron dosimetry using wide based n^+pp^+ silicon diodes.* Proc. First Symp. Neutron Dosim. in Biol. and Medicine. p.343 (CEC, Luxembourg)(1972).
40. Sanchez. F. Madgura, G. and Arrans. *Neutron measurements around an 18 MV linac.* Radiotherapy and Oncology **15** 259-265 (1989).
41. Ing, H., Nelson, W.R. and Shore, R.A. *Unwanted photon and neutron radiation resulting from collimated photon beams interacting with the body of radiotherapy patients.* Med. Phys. **9** (1) (1982).
42. Laughlin, J.S., Reid, A., Zeitz, L., and Ding, J. *Unwanted neutron contribution to megavoltage x-ray and electron therapy.* p.1 in **NBS-554** (US Government Printing Office, Washington) (1979).

43. Fox, J.G. and McAllister, J.D. *Fast neutrons from a 25 MeV betatron.* Med.Phys.**4** 387 (1977).

44. Horesly, R.J., Johns,H.E., Haslam, R.N.H. *Energy absorption in human tissue by nuclear processes with high energy x-rays.* Nucleonics. **11** (2) 28 (1953).

45. Allen, P.D. and Chaudhri, M.A. *The dose contribution due to photonuclear reactions during radiotherapy.* Med. Phys. **9** 904 (1982).

46. Nemec, H.W. and Roth, J. *Dosisverteilung der Photonen und Neutronen ausserhalb des Bremsstrahlungfeldes eines 8 MeV inearbeschleunigers. Strahlentherapie* **154** 380 (1976).

47. McGinley, P.H., Wood, M., Mills, M., and Rodriguez, R. *Dose levels due to neutrons in the vicinity of high-energy medical accelerators.* Med.Phys.**3** 397 (1976).

48. Deye, J.A. and Young, F.D. *Neutron production from a 10 MV LINAC.* Phys.Med.Biol.**22** 90 (1977).

49. McGinley, P.H. and Sohrabi, M. *Neutron contamination in the primary beam.* p.99 in **NBS-554** (US Government Printing Office, Washington) (1979).

50. Rodger, D.W.O. and Van Dyk, G. *Use of a neutron remmeter to measure leakage neutrons from medical accelerators.* Med. Phys. **8** 163 (1981).

51. Al-Janabi, M.A., Crossman, J.S.P., Foster,C.J, Robertson, M. and Watt,D.E.. *Yields and quality of photoneutron fields in the vicinity of high energy therapy machines.* Radiat. Prot. Dosim. **52** 1-4 p.119-122 (1994).

52. McCall, R.C. McCall Associate (report unpublished)(1982).

53. Tosi, G., Torresin, A., Agosto, S., Foglio Para, A., Sanguist, V., Zeni, L. and Silari, M. *Neutron measurements around medical electron accelerators by active and passive detection techniques.* Med. Phys.**18** (1) (1991).

54. Atherton, L. *Note on neutron measurements - 16 MeV linear accelerator.* International Electrochemical Internal Report. (1979).

55. Drouet, J., Moreau, J.C., Quechon, H., and Tabot,L. *Compte rendu des mesures effectues aupres d'un accelerateur Saturne de la CGR-MeV a Buc.* Saclay Report D. CEN-S/SPR/SRI/77507 GRA-092 JD/58 (1977).

56. Gur, D., Rosen, J.C. Burkowitz, and Gill,A. *Relative measures of fast neutron contamination in 18 MeV photon beam from a Philips Sl75-20 linear accelerator.* Med. Phys. 221 (1978).

57. Grant, W.H.III *Neutron leakage for Therac 20.* Unpublished report (1978).

58. Bading, J.R. and Zeittz, L. and Laughlin, J.S. *Phosphorus activation neutron dosimetry and its application to an 18 MV radiotherapy accelerator.* Med.Phys. **8** 5 (1982).

59. Marbach, J.R. *Neutron leakage from the Saggitaire linear accelerator at the University of Indiana at Indianapolis.* Unpublished report (1975).

60. LaRiviere, P.D. Varian internal Report Rad. Physics **11-81** (Varian associates, Palo Alto, California. (1982).

61. McCall, R.C. Unpublished data. (1977).

62. Leder, C.M. and Shirley, V.S. *Table of isotopes.* (John Wiley and Sons, USA) (1978).

63. Guinn, V.P. and Hoste, J. *Elemental analysis of biological material.* IAEA Technical Report Series **197** chpt.7 (IAEA, Vienna). (1980).

64 Rossi, H.H and Rosenzweig, W. *A device for the measurement of dose as a function of specific ionisation.* Radiology **64** 404 (1955).

65. Rossi, H.H. and Rosenzweig, W. *Measurements of neutron dose as a function of lineal energy transfer.* Radiat. Res. **2** 417 (1955b).

66. ICRU Report No.36. *Microdosimetry.* ICRU, 7910 Woodmont Ave. , Bethesda, Maryland, 20814. USA. (1983).

67. Blanc, D. and Terrisol, M. *Microdosimetry a tool for radiation research.* Radiat. Prot. Dosim. **13** 1-4 387-393 (1985).

68. Schmitz,T, Waker, A.J., Kliauga, P. and Zoetelif, H. (Eds.) *Design, construction and use of tissue equivalent proportional counters.* EURODOS Report 16178 **62** 4 (1995).

69. Campion, P.J. and Kingham, M.W. *The measurement of the gas multiplication in tissue equivalent gas.* Int. J. Appl. Rad. and Isotopes. **22** 703-706 (1971).

70. Watt, D.E. *Proportional counter design in radiocarbon dating.* Nucl. Inst. and Methods **50** 353-354 (1967).

71. Kellerer, A.M. *An assessment of wall effects in microdosimetric measurements.* Radiat.Res. **47** 377-386 (1971).

72. Kellerer, A.M. *Event simultaneity in cavities.* Radiat.Res. **48** 216-233 (1971).

73. Dietze, G., Menzel, H.G. and Buhler, G. *Calibration of tissue-equivalent proportional counters used in radiation protection dosimetry.* Radiat. Prot. Dosim. **9** (3) 245-249 (1984).

74. Pihet, P. and Menzel, H.G. *Atomic data required in accurate measurements of KERMA for neutrons with low pressure proportional counters.* Atomic and Molecular Data for Radiotherapy. IAEA, Vienna (1989).

75. Waker, A.J.. *Experimental uncertainties in microdosimetric measurements and an examination of the performance of three commercially produced proportional counters.* Nucl. Instr. and Methods in Phys.Res., A234 354-360 (1985).

76 Broerse, J.J., Minheer, B.J and Williams, J.R. *European Protocol for neutron Dosimetry for external beam therapy.* Br. J. Radiol. **54** 882-898 (1981).

77. Booz, J. *Microdosimetric spectra and parameters of low LET-radiations.* In proceedings of the Fifth Symposium on Microdosimetry, EUR 5452 (Luxembourg: CEC) 311-344 (1976).

78. Taylor, G.C., Fletcher, J.G. and Scott, M.C.. *Microdosimetric measurements of the Clatterbridge neutron therapy cancer therapy cyclotron.* Rad.Prot. Dosim. **31** (1/4) 443-447 (1990).

79. Schrewe, U.J., Brede, H.J., Pihet,P. and Menzel, H.G. *Calibration of tissue-equivalent proportional counters with built-in α-particle sources.* Radiat. Prot. Dosim. **23**(1/4) 249-252 (1988).

80. Crossman, J.S.P and Watt, D.E. *Inherent calibration of microdosemeters for dose distributions in lineal energy.* Radiat. Prot. Dosim. **55** 4 295-298 (1994).

81. Dahmen, P., Menzel, H.G. and Gillmaier, R. *Dosimetry of photons with low pressure proportional counters.* Radiat. Prot. Dosim. **29** No.1/2 81-85 (1984).

82. Iskef, J., Cunningham, J.W., and Watt, D.E. *Projected ranges and effective stopping powers of electrons with energy between 20 eV and 10 keV.* Phys.Med.Biol. **5** 535-545 (1983).

83. Vyatskin, A.Ya. and Trunev.V.V. Radiotekhnika i Elektronika. **12** 1636 (1967); **15** 565 (1970); **17** 1899 (1972).

84. Vyatskin, A.Ya., Trunev.V.V.and H.-J.Fitting. Radiotekhnika i Elektronika. **18** 432 (1973); **18** 1701 (1972).

85 Fitting, H.-J. *Transmission, energy distribution, and SE excitation of fast electrons in thin films.* Phys. stat. sol. (a) **26** 525 (1974).

86. Tung, C. J.; Ashley, J.C. and Ritchie, R.H. IEEE Trans. Nucl.Sci. **NS-26** 4814-8 (1979).

87. Watt, D.E. *Track structure for ionising radiation in liquid water.* Rep: Biophys /10/89. University of St.Andrews. UK(1989).

88. Kliauga, P.J and Rossi, H.H. *Studies with encapsulated sources of ^{128}I. Microdosimetry using a non-metallic wall-less proportional counter.* International J.Radiat.Oncology Biol.Phys. **8** 1963-1968 (1982)

89. Kliauga, P.J and Dvorak, R.. *Microdosimetric measurements of ionisation by monoenergetic photons.* Radiat. Protect.Dosimetry. **73** 1 (1978).

90. Varma, M.N. *Calibration of proportional counters in microdosimetry.* Proceedings of the 8th Symposium on Microdosimetry. EUR 8395 (London: Harwood Academic) 1051-1059 (1983).

91. ICRU 49 *Stopping powers and ranges for protons and alpha particles.* ICRU, 7910 Woodmont Ave., Bethesda, Maryland, 20814. USA. (1983).

92. Srdoc, D., Goodman, L.J., Marino, S.A., Mills, R.E., Zaider, M., and Rossi, H.H. *Microdosimetry of monoenergetic neutron radiation.* Proceedings of the 7th Symposium on Microdosimetry (London: Harwood Academic) 765-774 (1981).

93. Caswell, R.S. *Deposition of energy by neutrons in spherical cavities.* Radiat. Res. **27** 92-107 (1966).

94. Schummacher, H.and Menzel, H.G. *Comparison of microdosimetric characteristics of four fast neutron facilities.* In proceedings of the Seventh Symposium on Microdosimetry, EUR 7147 (Luxembourg: CEC) 1217-1232 (1981).

95. Fiddora, J. and Booz, J. *The local distribution of radiation quality of a collimated fast neutron beam from 15 MeV deuterons on beryllium.* In proceedings of the Sixth Symposium on Microdosimetry, EUR 6064 (Luxembourg: CEC) p.483 (1978).

96. Bonnett, D.E, Waker, A.J., Sherwin, A.G., and Souliman *Radiation metrology at a high-energy neutron therapy facility.* Radiat. Prot. Dosim. **2** 95-101 (1991).

97. Menzel, H.G., Buecher, G., and Schummacher,H. *Investigation of basic uncertainties in the experimental determination of microdosimetric data* Eighth Symposium on Microdosimetry (Luxembourg: CEC) 1061-1072 (1983).

98. Rodgers, R.C., and Gross, W. *Microdosimetry of monoenergetic neutrons.* Fourth Symposium on Microdosimetry, EUR 5122 (Luxembourg: CEC) p.1027.(1974).

99. Watt, D.E. Private communication (1992).

100. ICRP. *Protection against ionizing radiation from external sources used in medicine* Publication **33** *Annals of the ICRP vol. 39* (Oxford: Pergamon Press) (1983).

101 M^{c}.Ginley, P.H., and Butker, E.K *Evaluation of neutron dose equivalent levels at the maze entrance of medical accelerator treatment room.* Med. Phys. **18** (2) (1991).

102. Kersey, R.W., *Estimation of neutron and gamma radiation doses in the entrance mazes of SL75-20 linear accelerator treatment rooms.* Medicamundi **24** 151 (1979).

103. Oliver, G.D. Revised data from *fast neutron contamination in X ray beams of medical accelerators from 19 to 45 MV.* Presented at the annual meeting of the American Association of Physicists in Medicine (1974).

104. Lawson, R.C. and Watt, D.E. *Thermal neutron depth dose dependence on beam and phantom size for collimated beams of fast neutrons.* In: Watt.D.E DSc. Thesis **2** 4.6 (1975).

105. Bloch, S. and Shon, F.J. *Neutron dose measurements by an attenuation technique.* Health Physics **8** 533 (1962).

106. Watt DSc. *Studies with nuclear radiation.* **2** *Neutrons and heavy charged particles.* DSc. University of Dundee (1975).

107. Kellerer, A.M. and Rossi, H.H. *The theory of dual radiation action.* Curr. Top. Radiat. Res. Q **8** 85-158 (1972).

108. Amols, H.I., and Zellmer, D.L. *Microdosimetry of 10-15 MeV bremsstrahlung X rays.* Med.Phys. **11**, 227-253 (1984).

109 Tilikidis, A., Lind, B., Näfsstadius, P., and Brahme, A. *Microdosimetric investigation on the biological effectiveness of 50 MV scanned bremsstrahlung beams.* Doctoral Thesis. University of Stockholm. (1994).

110. Lindborg, L. *Microdosimetry measurements in the beam of high energy photons and electrons: techniques and results.* In Proc. Fifth Symposium on Microdosimetry, Verbiana, Italy. EUR-5452 (Luxembourg: CEC) 347- 375 (1976).

111. ICRU **37** *Stopping powers for electrons and positrons.* ICRU, 7910 Woodmont Ave., Bethesda, Maryland, 20814. USA. (1984).

112. Bengtsson, L.G. *Assessment of dose equivalent from fluctuations of energy deposition.* In Second Symposium on Microdosimetry.(Brussels: CEC) 375-400 (1969).

113. Kellerer, A.M., and Rossi, H.H. *On the determination of microdosimetric parameters in time-varying fields: the variance-covariance method.* Radiat. Prot. Dosim. **97** 237-245 (1984).

114. Kliauga, P., Amols,H., and Lidbourg, L. *Microdosimetry of pulsed radiation fields employing the variance method.* Radiat. Res. **105** 129-137 (1986).

115. Honré, H.B., Jensen, L.C., Jessen, K.A. and Nielsen, H.H *Variance-covariance measurements in therapeutic and diagnostic radiation beams* Radiat. Prot.Dosim. **52** (1-4) 387-390 (1994).

116. Greene, D. *Linear accelerators for radiation therapy.* Med. Phys. Handbooks **17** ((Adam and Hilger, Bristol).(1986).

117. Beddar, A.S., Mackie, T.R., and Attix, F.H. *Cerenkov light generated in optical fibre and other light pipes irradiated by electron beams.* Phys.Med.Biol. **37** 925-935 (1992).

118. Matsumoto,T. *Dose equivalent measurement for thermal neutrons and gamma rays with a small BGO scintillator connected to an optical fibre.* Radiat. Protect. Dosim. **35** (4) .241-245 (1992).

119. Languesse, M. and Bourdinaud.M *Radiation sensor based on inorganic scintillator with fibre readout for high energy radiography.* Sensors and Actuators A. **32**.464-469 (1992).

120. Hille, R., Bueker, H., and Haesing, F.W. *Glass fibres as radiation detectors.* Nucl. Instr.and Meth. A299 pp217-221 (1990) .

121. Braunlich, P., Jones, S.C, and Tetzlaff, W. *A remote fibre-optic microdosimetry reader.* Rad. Prot. Dosim.**6.** (1-4) 103-107 (1984).

122. Beddar, A.S., Mackie, T.R., and Attix, F.H. *Water-equivalent plastic scintillation detectors for high -energy dosimetry: I. Physical characteristics and theoretical considerations.* Phys.Med.Biol. **37** 1883-1900 (1992).

123. Birks, J.B., *The theory and practice of scintillation counting.* (Pergamon Press : New York) (1964).

124. Curran, S.C. and Baker, W.R., US Atomic Energy Commission Report. MMDC 1296 (1944).

125. Knoll, G.F. *Radiation detection and measurement.* Ed. 2 (John Wiley and Sons) (1989).

126. Younis, A-R. S.*Biophysical damage in Metallo-enzyme and mammalian cells by Cu - K X rays and radioisotopes.* Doctorate thesis, University of St.Andrews. (1989).

127. Crossman, J.S.P., Foster, C.J. and Watt, D.E. *Endo-microdosemeters for the control of radiation effectiveness in therapy applications.* Radiat. Prot. Dosim. **61** (1-3) 25-28 (1995).

128. De Boer, S.F., Beddar A.S., and Rawlinson, J.A. *Optical filtering and spectral measurements of radiation-induced light in plastic scintillation dosimetry.* Phys.Med.Biol.**38** 945-958 (1993).

129. Pruett, B.L., Peterson, R.T., and Smith, D.E. *Gamma-ray to Cerenkov light conversion efficiency for pure silica-core optical fibres.* SPIE **506** 10-16 (1984).

130. Sowerby, B.D. *Cerenkov detectors for low-energy gamma rays.* Nucl. Instr.and Meth. **97** 145-149 (1971).

131. Beddar, A.S., Mackie, T.R., and Attix, F.H. *Water-equivalent plastic scintillation detectors for high-energy dosimetry: II Properties and measurements.* Phys. Med. Biol. **37** 1901-1913 (1992).

132. Rossi, H.H. and Mays, C.W. Health Physics **34** No.353 (1978).

133. UNSCEAR *Sources and effects of ionising radiation.* Report to the General Assembly, with Annexes Publ. E771X1, (United Nations, New York).(1977).

134. Laughlin, J.S., Mohan, R., Kutcher, G.J. *Choice of optimum megavoltage for accelerators for photon beam therapy.* Int. J. Radiat. Onc. **12** 1551- 1557 (1986).

135. Parry J. Private communication. Dept. of Radiotherapy, Ninewells Hospital, Dundee.

136. Wambersie, A., Pihet, P., and Menzel, H.G. *The role of microdosimetry in radiotherapy.* Radiat. Prot. Dosim. **31** 421-429 (1990).

137. Yusuf, A.M. *Advances in semiconductor device design for radiation detection in medical and industrial application.* Doctoral thesis, University of St.Andrews (1992).

138. Dietze, G., Menzel, H.G. and Buhler, G. *Calibration of tissue-equivalent proportional counters used in radiation protection dosimetry.* Radiat. Prot. Dosim. **9**(3) 245-249 (1984).

139. ICRU **39** *Dose and volume specification for reportin intracavity therapy in gynecology.* ICRU, 790 Woodmont Ave, Washington DC 20014, USA(1985).

140. Attix, F.H. *Introduction to radiological physics and radiation dosimetry.* (John Wiley and Sons) (1986).

141. ICRU **16** *Linear energy transfer.* ICRU, 790 Woodmont Ave, Washington DC 20014, USA (1971).

142. ICRU **44** *Tissue Substitutes in radiation dosimetry and measurement.* ICRU, 790 Woodmont Ave, Washington DC 20014, USA (1989).

143. Wycoff, H.O. Med.Phys. **10** 715 (1983).